Superconducting qubit readout via low-backaction electro-optomechanical transduction

by

Robert Delaney

BSc, University of British Columbia, 2014

MSc., University of British Columbia, 2016

A thesis submitted to the

Faculty of the Graduate School of the

University of Colorado in partial fulfillment

of the requirements for the degree of

Doctor of Philosophy

Department of Physics

2022

Committee Members:

Konrad Lehnert, Chair

Cindy Regal

John Teufel

Graeme Smith

András Gyenis

Delaney, Robert (Ph.D., Physics)

Superconducting qubit readout via low-backaction electro-optomechanical transduction

Thesis directed by Prof. Konrad Lehnert

Entangling superconducting quantum processors via light would enable new means of secure communication and distributed quantum computing. However, transducing quantum signals between these disparate regimes of the electromagnetic spectrum remains an outstanding goal and interfacing superconducting qubits with electro-optic transducers presents significant challenges due to the deleterious effects of optical photons on superconductors. An ideal transducer should leave the state of the qubit unchanged: more precisely, the backaction from the transducer on the qubit should be minimal.

In this work, I demonstrate readout of a superconducting transmon qubit via a low-backaction electro-optomechanical transducer. Requirements for integrating technology from circuit quantum electrodynamics are discussed, and the results of superconducting qubit readout via an electro-optic transducer are presented. The modular nature of the transducer and circuit QED system used in this work enable complete isolation of the superconducting qubit from optical photons, and the backaction on the qubit from the transducer is less than that imparted by thermal radiation from the environment. I show that only moderate improvements in transducer bandwidth and added noise should enable the transduction of non-classical signals from a superconducting qubit to the optical domain.

Acknowledgements

There are many people I'd like to thank, who have helped significantly with the work that went into this thesis, and who helped me with the completion of my PhD. First off, my experience working at JILA over the past 5 plus years has been really incredible. There are too many people to include here, but really everyone that works at JILA contributes to the goal of completing amazing research, and it really has been a pleasure to work here with so many amazing people.

Before I even arrived at CU Boulder, I learned a huge amount about low temperature physics from my previous supervisors Douglas Bonn and Sarah Burke, as well as James Day and Pinder Dosanjh. Much of the work in this thesis would have been far more difficult to complete without the things I learned from them about the assembly of fragile low temperature physics experiments.

When I first started working in the lab Adam Reed was incredibly helpful, and taught me how to keep a rickety old dilution refrigerator going. He also taught me the inner workings of our electromechanical experiments. Lucas Sletten, Eric Rosenthal, Brad Moores, Dan Palken, Ben Chapman and Xizheng Ma worked alongside me in the lab through much of my PhD. I learned a huge amount from all of them, and really enjoyed my time working in the lab with them.

During the later part of my PhD I joined the microwave-to-optical transduction team, which has been an amazing experience, where I got to work with many great people. Jon Kindem, Max Urmey, Benjamin Brubaker, Peter Burns and Sarang Mittal have all been incredible teammates, and the work presented in this thesis would not have been in any way possible without each of their contributions. It has also been a pleasure to get to know and work with the newer members of the microwave-to-optical transduction team Luca Talamo, Kazemi Adachi and Sheng-Xiang Lin.

Joining the microwave-to-optical transduction team has also given me the privilege of getting to work with Cindy Regal. Her incredible insight into any and all aspects of experimental quantum optics has been extremely helpful, and she has really helped broaden my knowledge of the field.

I'd like to thank the other members of my thesis committee for taking the time out of their busy schedules to be on my committee: John Teufel, Graeme Smith and András Gyenis. In particular, we have often leaned on John Teufel for his expertise in electromechanics, and he has given incredibly useful feedback on both of the manuscripts that are described in this thesis.

Finally, I feel very lucky that I ended up in Konrad's group for my PhD, and working for him has really made my PhD an enjoyable experience. While he always guided me towards certain experimental goals, he has also provided the freedom to explore new ideas. Through our many meetings I've learned a huge amount from him about physics in general, and I'm continually impressed by his knowledge of experimental physics.

Contents

Chapter

Tables

Table

Figures

Figure

Chapter 1

Introduction

1.1 Communication with electromagnetic waves

Analog and digital communication through electro-magnetic waves has existed for centuries in various different forms. Optical telegraphs, or semaphores, used lights modulated by manual shutters to distribute digitally encoded information over long distances through a series of stations [1]. This basic demonstration of digital communication via light was followed by more advanced technologies such as the telegraph [2], where radio frequency information was digitally encoded via Morse code [3], and sent through radio frequency transmission lines. Today a huge portion of the electromagnetic spectrum is used for classical communication, with frequencies from a few hertz in under water or geological applications all the way up to terahertz scale optical frequencies used by the modern classical internet.

Although the bandwidth, speed and ubiquity make the modern day internet seem completely different from these early technologies, it is nonetheless all based upon encoding digital information in electromagnetic waves. Relatively recent technological advances over the past few decades have enabled the fast distribution of classical information through the internet, and much of this progress has largely been enabled by the use of fiber optic cable. Computers operate at radio frequencies, where the classical bits are operated at microwave clock frequencies, but this information then gets converted to infrared light for transmission through optical fibers near a wavelength of 1550 nm. The bandwidth over which signals can be encoded is much larger at optical frequencies than at microwave frequencies, meaning that a much larger number of bits can be sent in parallel. Furthermore, when

compared to coaxial transmission lines, optical fiber offers extremely low loss transmission, with state of the art fibers demonstrating only 0.14 dB/km of loss [4].

An equivalent dichotomy between microwave frequency computation and optical communication is arising in the field of quantum information, where it would be extremely useful if an analogous quantum internet [5, 6, 7, 8] could be developed. As in the classical case, it is best to encode quantum information in optical light for transmission, but due to additional and more stringent constraints on noise when transmitting quantum states, if quantum computations are performed at microwave frequencies, the quantum states *must* be transmitted optically in order to prevent the quantum state from being corrupted by thermal noise at ambient temperature.

1.1.1 Superconducting quantum computers

In classical computing, one of the first transistors [9] was held together by paper clips and gold foil, but transistors quickly progressed over more than 70 years to precisely fabricated, nanometer scale devices, with modern transistors spanning less than 14 nm, where now millions of transistors can be placed on a single chip. Today, quantum computing has progressed far past this stage of hastily prepared one-off devices [9], and we are now seeing the demonstration of modest quantum processors [10, 11, 12, 13] with capabilities that may soon be able to exceed those of classical computers [14] for certain computational tasks [15]. As a result, much research effort is being invested in rapidly scaling these capabilities.

Although there exist a wide range of platforms that are being investigated for scalable quantum computation, including trapped ions [16], neutral atoms [17] and optical qubits [18], one commonly pursued technique involves superconducting qubits [19, 20], in which the Josephson effect [21] can be used to create an artificial atom. The transition between the lowest two energy levels of these anharmonic inductor-capacitor (LC) circuits [22] is at microwave frequencies, typically in the range of $4-12$ GHz. Analogous to the modern transistor it is possible to fabricate these superconducting qubits using standard lithographic techniques [23, 24, 25], meaning that a large number of precisely engineered devices can be fabricated all on the same chip [12]. Furthermore,

the microwave transition frequencies enable the use of standard microwave technology similar to that used in cellphones for the control and readout of qubits. This contrasts systems involving atoms or trapped ions, which rely upon an atomic transition fixed by the laws of nature to form the physical qubit. Although this can have advantages in terms of the lifetime and reproducibility of the effective qubit, the ability to engineer the device that is needed, rather than trying to accommodate a physical system that already exists, is invaluable, and has spurred much research and investment in superconducting quantum computation.

However, the major drawback of superconducting quantum computers is their reliance upon low temperature for proper operation. There exists two main reasons for this constraint. First, a microwave resonator will not be in its quantum ground state (the thermal occupancy of the resonator is $n_{\mathrm{th}} \ll 1$) until its temperature is below 100 mK, meaning that some sort of cooling is required. Note that this can be true in atomic systems as well, where the motional state of the atom is typically far from the quantum ground state at ambient temperature, however this is typically addressed through techniques such as laser cooling [26, 27]. Second, the reliance these qubits have on superconductivity, means that the material used must be in the superconducting state, and in fact, must be deep in the superconducting state to avoid the deleterious effects of quasiparticles in the superconductor [28, 29, 30, 31]. Since aluminum is by far the best material for the fabrication of Josephson junctions, due to the clean aluminum oxide layers that can be easily formed through oxidizing the material, this necessitates operating superconducting qubits at a temperature far below that of the critical temperature of aluminum ($T_{\mathrm{c}} = 1.2$ K), or essentially again also at a temperature below 100 mK. Thus far, this has not impeded progress in developing superconducting quantum computers, as standard tools from low temperature physics such as dilution refrigerators exist, and can easily cool devices down below 50 mK. There do exist questions about just how far this technology can be scaled, as being able to address millions of qubits (in order to form far less logical qubits via error correction [32, 33, 34, 35]) presents difficulties for the thermalization of the control lines connected to the processor [36]. However, this is an active field of research [37, 38, 39], and has not yet proven to be a limiting factor.

1.1.2 The quantum internet

The speed of the classical internet is limited by the physical laws of nature, as a single bit of information cannot be sent faster than the speed of light. Furthermore, the total bandwidth of the transmission medium determines the number of bits that can be sent in parallel. The quantum internet is constrained as above, but also must meet a much more stringent set of requirements. For example classical bits can be made robust to errors and noise by simply making the pulse of light encoding the state 1 bright enough such that it is not possible to mistake it for the state 0. As long as there aren't constraints on the power of the classical signal being transmitted, errors can be made arbitrarily small during classical communication. Indeed, the invention of the transistor was motivated by the need to amplify analog classical information being transmitted through phone lines [9].

However, when transmitting quantum states, that are encoded in quantum excitations, or quanta, of the electromagnetic field, loss or added noise will irreversibly corrupt the quantum state of interest. Although loss can typically be detected and then subsequently compensated for through heralding techniques, where photon counting can be used to discard events in which no photon was detected [40, 41, 42, 43], even small amounts of noise (at even single photon levels) will quickly prevent the transmission of quantum information [44]. This is the why superconducting quantum computers must be operated at such low temperatures, as even if superconductivity was not a limiting factor (though it also is!), thermal noise would corrupt the states encoding the quantum information. A cryogenic link has recently been demonstrated between two separate dilution refrigerators [38] in the same room, and this will certainly be useful for expanding the local capabilities of superconducting quantum computers. However, this likely will not be scalable over long distances since cryogenic interconnects at millikelvin temperatures require extensive radiation shielding and vacuum systems that will be challenging to implement over kilometer scale distances.

In contrast to microwave frequency quantum devices, optical resonators are in their quantum ground state at ambient temperature, and optical quantum networks are an already proven tech-

nology [45, 46, 47], where qubits encoded in propagating optical photons can be sent through either optical fibers [48, 49, 50] or through free space [51]. Thus a natural way to network superconducting quantum computers would involve converting the quantum information encoded at microwave frequencies to optical frequencies for transmission through fiber optic cable, exactly in the same manner as in the classical internet. Thus, a necessary tool for the networking of superconducting quantum computers will be an electro-optic transducer that is capable of transducing quantum states between the microwave and optical domains.

Such a transducer must add close to zero noise, so as not to corrupt the fragile quantum states it is converting. Ideally, it should be efficient, such that it transduces nearly all of the incident signal and finally it should be compatible with superconducting qubits. More precisely, it should impart little to no backaction on the qubit, or more simply put, operating the transducer should have no effect upon the state of the superconducting qubit in any basis. In more direct analogy with the classical internet, ideally such a transducer should have a large enough bandwidth such that information can be encoded over a relatively large bandwidth.

It is interesting to note that one of the most promising candidates for building a successful quantum computer uses fabricated devices that operate at microwave frequencies, and the only reasonable technique for networking these quantum computers over any appreciable distance is through optical links—exactly what classical computing has converged upon. Thus for the quantum internet we desire all of the capabilities of today's classical internet such as large bandwidth, fast data transmission and reliability, but there also exist new requirements in order to preserve the quantum information being transmitted.

1.1.3 Electro-optic transducers for the quantum internet

Although much progress has been made in the realm of superconducting quantum computers, as of yet qubits and superconducting processors have only been connected in networks distributed within the same dilution refrigerator [52] or the same room [38]. The pursuit of a truly distributed (over kilometer distance scales) quantum network of superconducting qubits has thus given rise

to a rich research field [53] searching for efficient, low-noise electro-optic transduction techniques [54, 55, 56, 57, 58, 59, 60, 61, 62, 63, 64, 65]. Due to the orders of magnitude difference in energy scale between microwave and optical signals, these electro-optic transducers must use intermediary systems that simultaneously interact with both microwave and optical photons, where the interaction strength is enhanced parametrically by microwave and optical pumps. Examples of electro-optic transduction platforms include non-linear solid state materials [66, 65], Rydberg atom ensembles [55], magnonic systems [54], rare earth ions [64], or mechanical resonators [58, 67, 56, 61, 62]. When such quantum enabled transducers become available, the engineerability of microwave frequency superconducting qubits can then be combined with the advantages of certain optical elements such as state of the art photon counting and low loss optical transmission over optical fiber [68]. These different technologies can then be combined to perform new and exciting quantum optics experiments, and to create networks of superconducting quantum processors.

1.2 Thesis overview and contents

Networking superconducting quantum computers is very much in the early stages of development. This is mainly due to the fact that, although electro-optic transducers are now quantum enabled [65], or nearly quantum enabled [62, 69], they are not yet able to distribute quantum signals from superconducting qubits to optical communication channels.

This thesis work will describe experiments in which a superconducting qubit is integrated with an electro-optic transducer based upon an electro-optomechanical device. More broadly I use the framework of linear quantum optics [70] to describe the process of reading out a superconducting qubit, converting that propagating microwave signal encoding the state of the qubit to an optical pulse and then measuring the resulting optical output. Although the microwave-to-optical transducers being developed at JILA [67, 56, 69] are not yet quantum enabled, it is still possible to learn valuable information about the integration of superconducting qubits with electro-optic transducers through the process of reading out the qubit optically.

In Chapter 2 I outline the theoretical requirements for transducing signals from a circuit

QED system to the optical domain. In Chapter 3 I discuss experimental requirements and figures of merit for the transduction of signals from the circuit QED system. In Chapter 4 the results of optically mediated single-shot readout of a superconducting qubit are discussed and by using the superconducting qubit as a non-Gaussian resource, the quantum efficiency of the optical measurement apparatus is characterized. In Chapter 5 the backaction from the electro-optic transducer on the qubit is measured and discussed. Chapter 6 describes a purely electromechanical experiment from earlier in my PhD, where a new technique for pulsed measurement of the motion of a mechanical oscillator was developed. The thesis is concluded in Chapter 7, where the outlook for quantum enabled electro-optic transduction of photons from a circuit QED system is discussed.

Chapter 2

Electro-optic transduction theory

2.1 Overview

In this chapter I describe the necessary theoretical requirements to achieve transduction between the microwave and optical domain, as well as the additional constraints that apply when integrating superconducting qubits with electro-optic transducers. Ideally, an electro-optic transducer performs unitary operations on the microwave and optical signals, with no signal lost, or noise added by the transduction process, but of course in a real transducer this is not the case, and in this Chapter the non-idealities of the transduction process are discussed.

The needed interactions for electro-optic transduction can be achieved in several different ways. As is common in devices that use the direct electro-optic effect [65, 66, 71], a direct interaction between microwave and optical fields can be mediated, which enables swapping between microwave and optical photons. Such devices typically rely upon the Pockels effect, where an electric field can produce birefringence in an optical medium [72]. Alternatively, one can introduce an intermediate resonant mode, frequently a mechanical oscillator [69, 62, 60], which interacts simultaneously with microwave and optical fields to mediate the transduction process.

2.2 A simple beamsplitter interaction

To achieve ideal electro-optic transduction, a unitary transformation between an input field at microwave (optical) frequencies and an output field at optical (microwave) frequencies is required. The most basic version of this unitary operation is described by a beam-splitter interaction in terms

of bosonic operators $\hat{a}$ and $\hat{b}$:

$$H_{\mathrm{bs}}/\hbar = g_{\mathrm{bs}}\hat{a}\hat{b}^{\dagger} + g_{\mathrm{bs}}^{*}\hat{a}^{\dagger}\hat{b}, \tag{2.1}$$

where optical excitations ($\hat{a}$) are swapped with microwave excitations ($\hat{b}$) with coupling strength g_{bs}.

With the Hamiltonian describing the system, one can use the Heisenberg-Langevin equations [73] to describe the equations of motion of the system. Where for an arbitrary operator $\hat{O}$,

$$\dot{\hat{O}} = \frac{i}{\hbar}[\hat{H}, \hat{O}] - \frac{\kappa_{\mathrm{tot}}}{2}\hat{O} + \sum_{j}^{N}\sqrt{\kappa_j}\hat{O}_{\mathrm{in,j}}. \tag{2.2}$$

Here, there are N total ports coupled to the system with individual coupling rates κ_j, and the (bosonic) mode has a total linewidth of:

$$\kappa_{\mathrm{tot}} = \sum_{j}^{N}\kappa_j. \tag{2.3}$$

For ports that the experimentalist has physical access to, the input-output relations can also be usefully described by:

$$\hat{O}_{\mathrm{in,j}} + \hat{O}_{\mathrm{out,j}} = \sqrt{\kappa_{\mathrm{j}}}\hat{O}. \tag{2.4}$$

Thus, for the simple beamsplitter interaction described in Equation 2.1, the Heisenberg-Langevin equations yield:

$$\dot{\hat{a}} = -\frac{\kappa_{\mathrm{o}}}{2}\hat{a} + ig_{\mathrm{bs}}^{*}\hat{b} + \sqrt{\kappa_{\mathrm{o}}}\hat{a}_{\mathrm{in}} \tag{2.5}$$

$$\dot{\hat{b}} = -\frac{\kappa_{\mathrm{e}}}{2}\hat{b} + ig_{\mathrm{bs}}\hat{a} + \sqrt{\kappa_{\mathrm{e}}}\hat{b}_{\mathrm{in}}, \tag{2.6}$$

and

$$\hat{a}_{\mathrm{in}} + \hat{a}_{\mathrm{out}} = \sqrt{\kappa_{\mathrm{o}}}\hat{a}, \tag{2.7}$$

$$\hat{b}_{\mathrm{in}} + \hat{b}_{\mathrm{out}} = \sqrt{\kappa_{\mathrm{e}}}\hat{b}, \tag{2.8}$$

where κ_{o} (κ_{e}) is the coupling of the optical (microwave) resonator to its external port.

Assuming steady state input fields, one can look at the steady state response of the optical and microwave fields such that $\dot{\hat{a}} = \dot{\hat{b}} = 0$. This gives:

$$\hat{a} = \frac{2ig_{\mathrm{bs}}^{*}}{\kappa_{\mathrm{o}}}\hat{b} + \frac{2}{\sqrt{\kappa_{\mathrm{o}}}}\hat{a}_{\mathrm{in}} \tag{2.9}$$

$$\hat{b} = \frac{2ig_{\mathrm{bs}}}{\kappa_{\mathrm{e}}}\hat{a} + \frac{2}{\sqrt{\kappa_{\mathrm{e}}}}\hat{b}_{\mathrm{in}}. \tag{2.10}$$

Assuming that g_{bs} is real (which amounts to a choice of arbitrary phase), and I can also define the cooperativity as:

$$C = \frac{4g_{\mathrm{bs}}^2}{\kappa_{\mathrm{e}}\kappa_{\mathrm{o}}}. \tag{2.11}$$

Using Equations. 2.7, 2.8, 2.9 and 2.10, I can solve for the optical and microwave output fields $\hat{a}_{\mathrm{out}}$ and $\hat{b}_{\mathrm{out}}$ in terms of the optical input $\hat{a}_{\mathrm{in}}$ and the microwave input $\hat{b}_{\mathrm{in}}$, which gives:

$$\hat{a}_{\mathrm{out}} = \frac{1}{1+C}\left(2i\sqrt{C}\hat{b}_{\mathrm{in}} + (1-C)\,\hat{a}_{\mathrm{in}}\right), \tag{2.12}$$

$$\hat{b}_{\mathrm{out}} = \frac{1}{1+C}\left(2i\sqrt{C}\hat{a}_{\mathrm{in}} + (1-C)\,\hat{b}_{\mathrm{in}}\right), \tag{2.13}$$

and provides the desired linear relation between microwave input fields and the optical output field. It is clear that this can be written in terms of a unitary matrix such that:

$$\begin{pmatrix} \hat{a}_{\mathrm{out}} \\ \hat{b}_{\mathrm{out}} \end{pmatrix} = \hat{U} \begin{pmatrix} \hat{a}_{\mathrm{in}} \\ \hat{b}_{\mathrm{in}}, \end{pmatrix} \tag{2.14}$$

where the $\hat{U}$ is given by:

$$\hat{U} = \frac{1}{1+C}\begin{pmatrix} 1-C & 2i\sqrt{C} \\ 2i\sqrt{C} & 1-C \end{pmatrix}. \tag{2.15}$$

It is critical that the matrix $\hat{U}$ be unitary as it must preserve the bosonic commutation relations of the output fields [74].

Furthermore, it is clear that at unit cooperativity Equations 2.12 and 2.13 simplify drastically to:

$$\hat{a}_{\mathrm{out}} = i\hat{b}_{\mathrm{in}}, \tag{2.16}$$

$$\hat{b}_{\mathrm{out}} = i\hat{a}_{\mathrm{in}}, \tag{2.17}$$

which is of course an ideal bidirectional transduction operation.

Of equal importance is the noise properties of such a transducer, which can be found through the auto-correlation functions for the optical and microwave fields:

$$\langle \hat{a}_{\text{in}}(t)\hat{a}^{\dagger}_{\text{in}}(t')\rangle = \delta(t-t') \tag{2.18}$$

$$\langle \hat{a}^{\dagger}_{\text{in}}(t)\hat{a}_{\text{in}}(t')\rangle = 0 \tag{2.19}$$

$$\langle \hat{b}_{\text{in}}(t)\hat{b}^{\dagger}_{\text{in}}(t')\rangle = (1+n_{\text{mic}})\delta(t-t') \tag{2.20}$$

$$\langle \hat{b}^{\dagger}_{\text{in}}(t)\hat{b}_{\text{in}}(t')\rangle = n_{\text{mic}}\delta(t-t'), \tag{2.21}$$

where n_{mic} describes the thermal occupancy of the microwave field and I have assumed that the optical field is in its ground state. For microwave-to-optical transduction, the variance of the optical output field is:

$$\langle \hat{a}_{\text{out}}(t)\hat{a}^{\dagger}_{\text{out}}(t')\rangle = \frac{4C}{(1+C)^2}\langle \hat{b}_{\text{in}}(t)\hat{b}^{\dagger}_{\text{in}}(t')\rangle + \frac{(1-C)^2}{(1+C)^2}\langle \hat{a}_{\text{in}}(t)\hat{a}^{\dagger}_{\text{in}}(t')\rangle \tag{2.22}$$

$$\langle \hat{a}_{\text{out}}(t)\hat{a}^{\dagger}_{\text{out}}(t')\rangle = \left(\frac{4C}{(1+C)^2}(1+n_{\text{mic}}) + \frac{(1-C)^2}{(1+C)^2}\right)\delta(t-t'), \tag{2.23}$$

Note, that there is gain $G = \frac{4C}{(1+C)^2}$ (or if one prefers, attenuation, since $G \leq 1$), which is only unity for $C = 1$. Dividing by this gain gives noise referred to the input microwave port of:

$$\langle \hat{a}_{\text{out}}(t)\hat{a}^{\dagger}_{\text{out}}(t')\rangle/G = \left(1 + n_{\text{mic}} + \frac{(1-C)^2}{4C}\right)\delta(t-t'). \tag{2.24}$$

Note that the factor of unity is simply the contribution from microwave vacuum fluctuations, and is an inherent part of the signal, thus the *added* noise from transduction is:

$$n_{\text{add}} = n_{\text{mic}} + \frac{(1-C)^2}{4C}, \tag{2.25}$$

which can be made arbitrarily small by ensuring low microwave thermal occupancy and the $C \approx 1$ limit.

An example of this 'direct' beamsplitter between microwaves and optics involves the use of whispering gallery mode resonators, where the microwave field can directly modulate optical light via an inherent electro-optic non-linearity of the material such as lithium niobate [66]. The free spectral range of an optical whispering gallery mode resonator matches that of a microwave

resonator, allowing the electro-optic effect to be resonantly enhanced by pumping one of the modes, yielding the direct beamsplitter interaction between microwaves and optics described above. While this technology is promising, and recently demonstrated quantum enabled microwave to optical transduction for the first time [65], it has yet to be integrated with superconducting qubits, which, as will be shown in this work, provide significant additional constraints.

2.3 Transduction through an intermediary mode

An alternative technique for microwave-to-optical transduction, is to instead swap excitations to an intermediary system that interacts with both microwave and optical photons, achieving the same result as a direct beamsplitter. In the electro-optomechanical system used here, this intermediary coupling is mediated by a high quality factor mechanical mode, and gets described by the interaction Hamiltonian:

$$H_{\text{int}}/\hbar = G_{\text{o}}^{*}\hat{a}^{\dagger}\hat{c} + G_{\text{o}}\hat{a}\hat{c}^{\dagger} + G_{\text{e}}^{*}\hat{b}^{\dagger}\hat{c} + G_{\text{e}}\hat{b}\hat{c}^{\dagger}. \tag{2.26}$$

where G_{o} and G_{e} are now the strength of the optomechanical and electromechanical beamsplitter interactions respectively.

2.3.1 Electro-optomechanical transduction

Another avenue towards quantum enabled electro-optic transduction involves the use of mechanical elements simultaneously coupled to optical and microwave light [56, 69, 62]. At JILA, membrane in the middle style devices have been pursued [75, 67, 56, 69, 76], where the motion of a partially transparent silicon nitride membrane inside of a Fabry-Pérot cavity modulates its resonance frequency. To achieve electromechanical coupling, a part of the silicon nitride membrane is metalized to form the capacitor in a microwave frequency LC circuit. Motion of the silicon nitride membrane changes the parallel plate capacitance and hence the resonance frequency of the LC circuit. For a more detailed description of the electro-optomechanical transducer see [67, 56, 69].

2.3.2 Beamsplitter interaction from real electro-optomechanical coupling

The interaction described above is a pure beamsplitter interaction between a mechanical mode and optical/microwave electromagnetic modes. However, in practice electro-optomechanics achieves a Hamiltonian that instead approximates the beamsplitter interaction. The coupling between motion and light comes in the form of a position dependent frequency shift:

$$H_{\rm eo} = \hbar\omega_{\rm o}\hat{a}^\dagger\hat{a} + \hbar\omega_{\rm e}\hat{b}^\dagger b + \hbar\omega_{\rm m}\hat{b}^\dagger b + \hbar g_{\rm o}\hat{a}^\dagger\hat{a}(\hat{c}+\hat{c}^\dagger) + \hbar g_{\rm e}\hat{b}^\dagger\hat{b}(\hat{c}+\hat{c}^\dagger). \tag{2.27}$$

Where the Hamiltonian above of course does not provide the desired beamsplitter interaction. Furthermore, the electromechanical (optomechanical) coupling $g_{\rm e}$ ($g_{\rm o}$) is very small relative to $\kappa_{\rm o}$ and $\kappa_{\rm e}$. For example in [77, 69] the device had electromechanical and optomechanical coupling rates of $g_{\rm e} = 2\pi \times 1.6$ Hz and $g_{\rm o} = 2\pi \times 60$ Hz respectively. Thus, both to enhance this interaction strength and to yield the desired swapping interaction, strong microwave and optical pumps can be applied at frequencies $\omega_{\rm p,e}$ and $\omega_{\rm p,o}$ respectively, causing a displacement of the fields in the optical and microwave resonators such that $\hat{a} \to \bar{a} + \hat{a}$ and $\hat{b} \to \bar{b} + \hat{b}$. Linearizing the Hamiltonian around these strong pumps yields:

$$H_{\rm eo} = \hbar\Delta_{\rm o}\hat{a}^\dagger\hat{a} + \hbar\Delta_{\rm e}\hat{b}^\dagger b + \hbar g_{\rm o}\bar{a}(\hat{a}+\hat{a}^\dagger)(\hat{c}+\hat{c}^\dagger) + \hbar g_{\rm e}\bar{b}(\hat{b}+\hat{b}^\dagger)(\hat{c}+\hat{c}^\dagger) \tag{2.28}$$

where the detunings are given by $\Delta_{\rm o} = \omega_{\rm o} - \omega_{\rm p,o}$ and $\Delta_{\rm e} = \omega_{\rm e} - \omega_{\rm p,e}$. In this linearized Hamiltonian I now get the desired beamsplitter interaction, along with a two mode squeezing interaction where:

$$H_{\rm eo}^{int} = H_{\rm bs} + H_{\rm tms} \tag{2.29}$$

$$H_{\rm bs} = \hbar g_{\rm o}\bar{a}(\hat{a}^\dagger\hat{c} + \hat{a}\hat{c}^\dagger) + \hbar g_{\rm e}\bar{b}(\hat{b}^\dagger\hat{c} + \hat{b}\hat{c}^\dagger) \tag{2.30}$$

$$H_{\rm tms} = \hbar g_{\rm o}\bar{a}(\hat{a}^\dagger\hat{c}^\dagger + \hat{a}\hat{c}) + \hbar g_{\rm e}\bar{b}(\hat{b}^\dagger\hat{c}^\dagger + \hat{b}\hat{c}). \tag{2.31}$$

By choosing the detuning of the laser and microwave pumps, such that they are red-detuned with $\Delta_{\rm o} = \Delta_{\rm e} = -\omega_{\rm m}$, the beamsplitter interaction can be resonantly enhanced, while suppressing the two mode squeezing interaction.

2.4 State-space model for the electro-optomechanical transducer

To systematically solve the equations of motion describing the electro-optomechanical transducer and a coupled circuit QED system, techniques from linear control theory can be used [78]. From the Heisenberg-Langevin equations and the state-space model formalism the equations of motion can be written as:

$$\dot{\mathbf{x}}(t) = A\mathbf{x}(t) + B\mathbf{x}_{\text{in}}(t) \tag{2.32}$$

$$\mathbf{x}_{\text{out}}(t) = C\mathbf{x}(t) + D\mathbf{x}_{\text{in}}(t), \tag{2.33}$$

where $\mathbf{x} = (\hat{X}_1, \hat{Y}_1, \hat{Z}_1, \hat{X}_2, \hat{Y}_2, \hat{Z}_2)^T$ is a vector of quadrature amplitudes, with $\hat{X}_l$, $\hat{Y}_l$ and $\hat{Z}_l$ $(l = 1, 2)$ corresponding to the dimensionless optical, microwave and mechanical mode quadratures respectively. The optical quadratures can be defined in terms of creation/annihilation operators as $\hat{X}_1 = \frac{1}{2}(\hat{a}^\dagger + \hat{a})$ and $\hat{X}_2 = \frac{i}{2}(\hat{a}^\dagger - \hat{a})$, with the microwave and mechanical quadratures defined analogously. The input and output fields may also be written in vector form:

$$\mathbf{x}_{\text{in}} = (\hat{X}_{1,\text{in,ext}}, \hat{X}_{1,\text{in,int}}, \hat{Y}_{1,\text{in,ext}}, \hat{Y}_{1,\text{in,int}}, \hat{Z}_{1,\text{in,int}}, \hat{X}_{2,\text{in,ext}}, \hat{X}_{2,\text{in,int}}, \hat{Y}_{2,\text{in,ext}}, \hat{Y}_{2,\text{in,int}}, \hat{Z}_{2,\text{in,int}})^T \tag{2.34}$$

$$\mathbf{x}_{\text{out}} = (\hat{X}_{1,\text{out,ext}}, \hat{Y}_{1,\text{out,ext}}, \hat{X}_{2,\text{out,ext}}, \hat{Y}_{2,\text{out,ext}})^T, \tag{2.35}$$

The transducer can be viewed as a phase-preserving amplifier with near unity gain [74], so the equations of motion are independent of the phases of the optical and microwave pumps. Thus under an appropriate choice of these arbitrary phases, the elements of the matrices A, B, C, D in the state-space model can all be made real. Transforming to a rotating frame removes the free evolution of the quadratures, enabling the state-space model to be described with the following

matrices:

$$A_{\mathrm{RWA}} = \begin{pmatrix} -\frac{\kappa_{\mathrm{o}}}{2} & 0 & 0 & 0 & 0 & -g_{\mathrm{o}}\bar{a} \\ 0 & -\frac{\kappa_{\mathrm{e}}}{2} & 0 & 0 & 0 & -g_{\mathrm{e}}\bar{b} \\ 0 & 0 & -\frac{\gamma_{\mathrm{m}}}{2} & -g_{\mathrm{e}}\bar{b} & -g_{\mathrm{o}}\bar{a} & 0 \\ 0 & 0 & g_{\mathrm{o}}\bar{a} & -\frac{\kappa_{\mathrm{o}}}{2} & 0 & 0 \\ 0 & 0 & g_{\mathrm{e}}\bar{b} & 0 & -\frac{\kappa_{\mathrm{e}}}{2} & 0 \\ g_{\mathrm{o}}\bar{a} & g_{\mathrm{e}}\bar{b} & 0 & 0 & 0 & -\frac{\gamma_{\mathrm{m}}}{2} \end{pmatrix} \tag{2.36}$$

$$A = A_{\mathrm{RWA}} + \begin{pmatrix} Q & U \\ U & -Q \end{pmatrix} \tag{2.37}$$

$$Q = \begin{pmatrix} 0 & 0 & -g_{\mathrm{o}}\bar{a}\sin(2\omega_{\mathrm{m}}t) \\ 0 & 0 & -g_{\mathrm{e}}\bar{b}\sin(2\omega_{\mathrm{m}}t) \\ -g_{\mathrm{o}}\bar{a}\sin(2\omega_{\mathrm{m}}t) & -g_{\mathrm{e}}\bar{b}\sin(2\omega_{\mathrm{m}}t) & 0 \end{pmatrix} \tag{2.38}$$

$$U = \begin{pmatrix} 0 & 0 & g_{\mathrm{o}}\bar{a}\cos(2\omega_{\mathrm{m}}t) \\ 0 & 0 & g_{\mathrm{e}}\bar{b}\cos(2\omega_{\mathrm{m}}t) \\ g_{\mathrm{o}}\bar{a}\cos(2\omega_{\mathrm{m}}t) & g_{\mathrm{e}}\bar{b}\cos(2\omega_{\mathrm{m}}t) & 0 \end{pmatrix} \tag{2.39}$$

$$B = \begin{pmatrix} M & 0 \\ 0 & M \end{pmatrix} \tag{2.40}$$

$$M = \begin{pmatrix} \sqrt{\kappa_{\mathrm{o,ext}}} & \sqrt{\kappa_{\mathrm{o,int}}} & 0 & 0 & 0 \\ 0 & 0 & \sqrt{\kappa_{\mathrm{e,ext}}} & \sqrt{\kappa_{\mathrm{e,int}}} & 0 \\ 0 & 0 & 0 & 0 & \sqrt{\gamma_{\mathrm{m}}} \end{pmatrix} \tag{2.41}$$

$$C = \begin{pmatrix} \sqrt{\kappa_{\mathrm{o,ext}}} & 0 & 0 & 0 & 0 & 0 \\ 0 & \sqrt{\kappa_{\mathrm{e,ext}}} & 0 & 0 & 0 & 0 \\ 0 & 0 & 0 & \sqrt{\kappa_{\mathrm{o,ext}}} & 0 & 0 \\ 0 & 0 & 0 & 0 & \sqrt{\kappa_{\mathrm{e,ext}}} & 0 \end{pmatrix} \tag{2.42}$$

$$D = \begin{pmatrix} -1 & 0 & 0 & 0 & 0 & 0 & 0 & 0 & 0 & 0 \\ 0 & 0 & -1 & 0 & 0 & 0 & 0 & 0 & 0 & 0 \\ 0 & 0 & 0 & 0 & 0 & -1 & 0 & 0 & 0 & 0 \\ 0 & 0 & 0 & 0 & 0 & 0 & 0 & -1 & 0 & 0 \end{pmatrix}. \tag{2.43}$$

Where, κ_{o} (κ_{e}) is the total optical (microwave) cavity linewidth, the subscript 'ext' indicates coupling to an external port, the subscript 'int' indicates coupling to an internal loss port and the mechanical linewidth is given by γ_{m}.

2.4.1 Approximate frequency domain solution

As has been shown previously [67], the electro-optomechanical transducer has an approximately Lorentzian response in the frequency domain, where I can describe the transmission ($|S_{\mathrm{oe}}(\omega)|^2$) between the microwave and optical domain as a function of frequency as

$$|S_{\mathrm{oe}}(\omega)|^2 = \epsilon \frac{\kappa_{\mathrm{e,ext}}}{\kappa_{\mathrm{e}}} \frac{\kappa_{\mathrm{o,ext}}}{\kappa_{\mathrm{o}}} \frac{\Gamma_{\mathrm{e}}\Gamma_{\mathrm{o}}}{\omega^2 + \Gamma_{\mathrm{T}}^2/4} \eta_{\mathrm{g}}, \tag{2.44}$$

where $\omega = 0$ corresponds to a signal on resonance with the microwave LC circuit, and the Lorentzian has a characteristic linewidth of $\Gamma_{\mathrm{T}} = \Gamma_{\mathrm{e}} + \Gamma_{\mathrm{o}} + \gamma_{\mathrm{m}}$. η_{G} is a small transduction gain factor due to finite sideband resolution [79, 67]:

$$\eta_{\mathrm{G}} = \left(1 + \left(\frac{\kappa_{\mathrm{e}}}{4\omega_{\mathrm{m}}}\right)^2\right)\left(1 + \left(\frac{\kappa_{\mathrm{o}}}{4\omega_{\mathrm{m}}}\right)^2\right). \tag{2.45}$$

The strength of the optical (microwave) beamsplitter interaction $g_{\mathrm{o}}\bar{a}$ ($g_{\mathrm{e}}\bar{b}$) sets the total bandwidth of the transduction process, and determines the optomechanical and electromechanical damping rates respectively [67]:

$$\Gamma_{\mathrm{o}} \approx \frac{4g_{\mathrm{o}}^2\bar{a}^2}{\kappa_{\mathrm{o}}} \tag{2.46}$$

$$\Gamma_{\mathrm{e}} \approx \frac{4g_{\mathrm{e}}^2\bar{b}^2}{\kappa_{\mathrm{e}}}. \tag{2.47}$$

2.4.2 Time domain calculations

While solving the state-space model in the frequency domain provides insight into the bandwidth of the electro-optomechanical transducer, and can be done so exactly [67], for pulsed qubit readout experiments the signals are more easily represented in the time domain. Thus I elect to solve the state-space model in the time domain. To do so, I must also find the equations of motion for the circuit QED system's microwave cavity described by:

$$\dot{\hat{d}} = -\left(\frac{\kappa_{\mathrm{c}}}{2} + i\chi\right)\hat{d} + \sqrt{\kappa_{\mathrm{c,ext}}}\hat{d}_{\mathrm{in}} + \sqrt{\kappa_{\mathrm{c,w}}}\hat{d}_{\mathrm{in,w}} \tag{2.48}$$

$$\hat{d}_{\mathrm{out,w}} + \hat{d}_{\mathrm{in,w}} = \sqrt{\kappa_{\mathrm{c,w}}}\hat{d} \tag{2.49}$$

$$\hat{d}_{\mathrm{out}} + \hat{d}_{\mathrm{in}} = \sqrt{\kappa_{\mathrm{c,ext}}}\hat{d}, \tag{2.50}$$

where the subscript 'w' indicates the weakly coupled port to which the readout pulse is applied. The cavity is strongly overcoupled to its external coupling port (labeled 'ext'), which is routed towards the electro-optomechanical transducer. Note, that the sign in front of χ will depend upon whether the qubit is in the ground or the excited state, but because I am only interested in the energy transmitted, the phase of the readout pulse is irrelevant to the total amount of transmitted energy. The output field of the circuit QED system can then be split into quadratures such that:

$$\hat{W}_{1,\mathrm{out}} = \frac{1}{2}(\hat{d}_{\mathrm{out}} + \hat{d}^{\dagger}_{\mathrm{out}}) \tag{2.51}$$

$$\hat{W}_{2,\mathrm{out}} = \frac{i}{2}(\hat{d}^{\dagger}_{\mathrm{out}} - \hat{d}_{\mathrm{out}}) \tag{2.52}$$

The output quadrature fields of the qubit cavity can then be routed as inputs to the state-space model describing the electro-optomechanical transducer. I can then define the pulse transduction efficiency as:

$$\eta_{\mathrm{p}} = \epsilon\frac{\int \hat{X}_{1,\mathrm{out,ext}}(t)^2dt + \int \hat{X}_{2,\mathrm{out,ext}}(t)^2dt}{\int \hat{W}_{1,\mathrm{out,ext}}(t)^2dt + \int \hat{W}_{2,\mathrm{out,ext}}(t)^2dt}, \tag{2.53}$$

where I have included the optical cavity mode matching factor ϵ in η_{p}.

The pulse transduction efficiency depends strongly upon the temporal envelope of the signal emitted by the circuit QED system, and the properties of the qubit dictate the maximum length

of a useful qubit readout pulse T_p, and hence its minimum bandwidth $\Delta\omega_\mathrm{p}$. There exist two main factors limiting the length of T_p. First, in order to efficiently read out the state of the qubit, the signal-to-noise ratio (SNR) of the measurement does not increase significantly for $T_\mathrm{p} > T_1$, where T_1 is the lifetime of the qubit [80]. Second, I wish to characterize the quantum efficiency of the optically mediated qubit readout scheme (detailed in Chapter 4), which requires injecting a weak readout pulse of length T_p into a Ramsey sequence, and measuring the resulting amplitude of Ramsey oscillations. Thus the SNR of this measurement decreases exponentially as a function of the T_2 time of the qubit, and for $T_\mathrm{p} \sim T_2$, the integration times become prohibitively long. It is the combination of these two factors that sets a minimum bandwidth of the qubit readout pulse $\Delta\omega_\mathrm{p} \sim \frac{1}{T_2}$.

Both the circuit QED system and electro-optomechanical transducer's state-space models can be solved numerically to then calculate η_p. Where I have included the optical cavity mode matching ϵ as an additional factor included in the pulse efficiency. It can also be useful to express η_p in terms of approximate expressions from the various different efficiency contributions:

$$\eta_\mathrm{p} \approx \eta_\mathrm{t}\eta_\mathrm{bw}\eta_\mathrm{G} \tag{2.54}$$

$$\eta_\mathrm{p} \approx \underbrace{\left(\epsilon\frac{\kappa_\mathrm{o,ext}}{\kappa_\mathrm{o}}\frac{\kappa_\mathrm{e,ext}}{\kappa_\mathrm{e}}\frac{4\Gamma_\mathrm{e}\Gamma_\mathrm{o}}{\Gamma_\mathrm{T}^2}\right)}_{\eta_\mathrm{t}}\underbrace{\left(1-2\frac{\left(1-e^{-\Gamma_\mathrm{T}T_\mathrm{p}/2}\right)}{\Gamma_\mathrm{T}T_\mathrm{p}}\right)}_{\eta_\mathrm{bw}}\underbrace{\left(1+\left(\frac{\kappa_\mathrm{e}}{4\omega_\mathrm{m}}\right)^2\right)\left(1+\left(\frac{\kappa_\mathrm{o}}{4\omega_\mathrm{m}}\right)^2\right)}_{\eta_\mathrm{G}} \tag{2.55}$$

The first term is the transduction efficiency η_t, which characterizes the efficiency when transducing narrowband signals [67, 56, 69]. The second term η_bw, is the efficiency due to bandwidth limitations. To retrieve a tractable expression for this I approximate the output of the circuit QED system as a square pulse, and assume that the transducer has an entirely Lorentzian response with linewidth Γ_T (see Equation 2.44). The final term constitutes the gain of the transducer η_G due to finite sideband resolution [79]. These theoretical contributions to the quantum efficiency of the optically mediated readout, along with additional experimental contributions, will be described further in Chapter 4.

Figure 2.1 shows a theoretical calculation of $\eta_\mathrm{p} = \eta_\mathrm{t}\eta_\mathrm{bw}\eta_\mathrm{G}$ (see Equation 2.55) as Γ_e is

varied. The curves are calculated through the state-space model described in Section 2.4 using experimentally measured parameters as inputs. $\Gamma_o > \Gamma_e$ for all data points except the two rightmost points of the $\Gamma_o = 640$ Hz curve, which limits η_t. Additionally, there is insufficient total bandwidth Γ_T since the bandwidth of the qubit readout pulse (the readout pulse has length $T_p = 15$ µs) greatly exceeds the total bandwidth of the transducer. The combination of these effects causes η_p to peak at approximately 0.04.

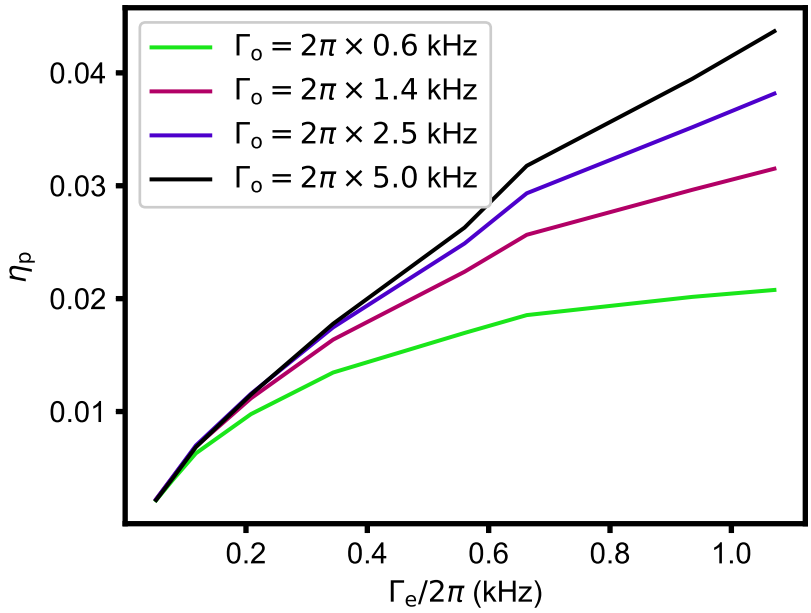

Figure 2.1: **Pulse transduction efficiency.** Numerically calculated pulse efficiency including contributions from bandwidth limitations, mismatch between Γ_e and Γ_o, optical mode matching, Γ_e-dependent LC circuit loss and transducer gain. Since the pulse used to readout the state of the qubit can have a maximum (useful) length of approximately the $T_1 \sim T_2$ time of the qubit, the bandwidth of the qubit pulse significantly exceeds that of the electro-optomechanical transducer, the primary limit to the η_p.

Chapter 3

Integrating Circuit QED technology with electro-optomechanical transducers: experimental requirements

3.1 Overview

Having demonstrated that electro-optomechanical transduction is theoretically feasible with classical Gaussian fields I now move onto the experimental requirements for coupling circuit QED technology to the microwave-to-optical transducer. The end goal is to efficiently transduce quantum states from a microwave frequency superconducting qubit through the electro-optomechanical transducer to the optical domain. Once upconverted to an optical signal these states can be detected with a linear optical detector, or alternatively via photon counting [62, 81].

Since quantum enabled electro-optic transduction is still in the early stages of development [82], and has yet to be achieved outside of the context of Gaussian fields [65], it is not yet possible to demonstrate non-classical optical photon statistics that are correlated with the state of a superconducting qubit. Nonetheless, by sending classical states from a circuit QED system through the electro-optomechanical transducer, one can still learn both about the properties of the transducer itself, and the effect of the transducer on the qubit. It is in this framework of classical qubit readout that I operate in order to learn about the integration of superconducting qubits with the electro-optomechanical transducer.

In this section I outline the necessary properties of a circuit QED system for coupling to the electro-optomechanical transducer, as well as the relevant performance metrics for the electro-optomechanical transducer itself. Figure 3.1 provides an experimental schematic demonstrating

the important elements of the optically mediated superconducting qubit readout experiment. The experiment can be broken into four main components, with the first being the circuit QED system (see Figure 3.1(a)), containing a transmon qubit dispersively coupled (see Section 4.2 for an exact definition of dispersive coupling) to a resonant microwave cavity. The isolation and coupling elements (see Figure 3.1(b)) enable proper routing of signals between the circuit QED system and the electro-optomechanical transducer, and isolate the circuit QED system from the strong microwave pumps required for transduction. The electro-optomechanical transducer itself is formed by a mechanically compliant silicon nitride membrane, which simultaneously modulates the resonance frequency of the optical Fabry-Perot cavity and a microwave frequency inductor-capacitor (LC) circuit (see Figure 3.1(c) and Section A.2). Finally, signals emitted by the electro-optomechanical transducer are detected via optical heterodyne detection (see Figure 3.1(d)).

3.2 Efficiently transducing signals from a circuit QED system

3.2.1 Bandwidth

The transducer has finite bandwidth, which limits the frequency span, and hence the minimum time duration of signals that it can efficiently transduce. The bandwidth of the transducer is given by $\Gamma_\mathrm{T} = \Gamma_\mathrm{e} + \Gamma_\mathrm{o} + \gamma_\mathrm{m}$, and ideally signals to be transduced through the converter will have bandwidth $\Gamma_\mathrm{sig} \ll \Gamma_\mathrm{T}$. Additionally, the transducer's efficiency depends strongly on what amounts to an impedance matching condition:

$$\eta_\mathrm{t} = \epsilon \frac{\kappa_\mathrm{o,ext}}{\kappa_\mathrm{o}} \frac{\kappa_\mathrm{e,ext}}{\kappa_\mathrm{e}} \frac{4\Gamma_\mathrm{e}\Gamma_\mathrm{o}}{\Gamma_\mathrm{T}^2}, \tag{3.1}$$

where maximal transduction efficiency η_t occurs for $\Gamma_\mathrm{o} = \Gamma_\mathrm{e}$. This requirement of $\Gamma_\mathrm{e} = \Gamma_\mathrm{o}$ for maximal η_t results from the simultaneous beamsplitter interactions, where for efficient transduction, optical and microwave photons must be swapped into the mechanical resonator at equal rates. Thus, if only one of Γ_e or Γ_o is limited for various technical reasons, the total bandwidth of the transducer will be limited when trying to maximize η_t. This was exactly the case in [77, 69], where $g_\mathrm{e} = 1.6$ Hz was significantly smaller than in previous devices, where for example in [56] $g_\mathrm{e} = 3.8$ Hz. Since

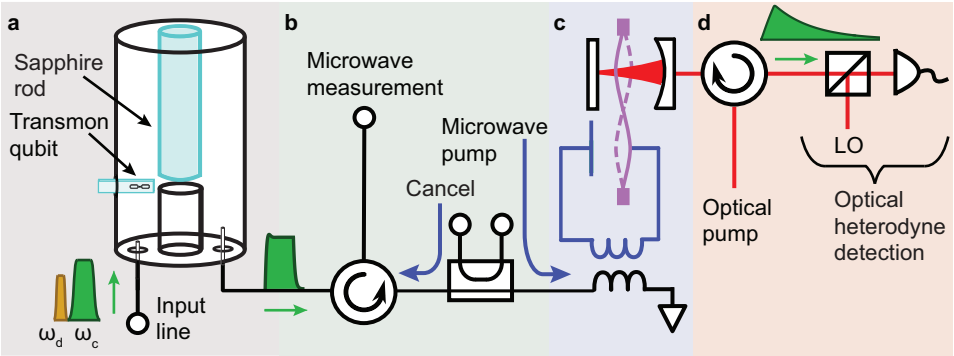

Figure 3.1: **Apparatus for readout of a superconducting qubit via the electro-optomechanical transducer.** (a) Circuit QED system consisting of a transmon qubit dispersively coupled to a 3D coaxial quarter-wave cavity resonator. A translatable sapphire rod tunes the frequency of the cavity *in situ*. Qubit preparation pulses with frequency ω_d (gold), followed by readout pulses with frequency ω_c (green), are injected through the circuit QED system's input line. (b) Isolation between the circuit QED system and the transducer is achieved using circulators, along with a directional coupler for interferometric cancellation. The directional coupler is also used to apply the microwave pump to the transducer, while the circulator enables microwave heterodyne measurement of reflected signals. (c) The electro-optomechanical transducer consists of an optical cavity and a flip-chip microwave LC circuit resonator simultaneously coupled to a single mode of a high-quality factor silicon nitride membrane with frequency $\omega_\mathrm{m}/2\pi = 1.45$ MHz. (d) Optical pump and heterodyne detection scheme.

$\Gamma_\mathrm{e} \approx 4g_\mathrm{e}^2|\bar{b}|^2/\kappa_\mathrm{e}$, this reduced the achievable damping rate by a factor of 5.6 for a given pump power $|\bar{b}|^2$, reducing the maximum achievable bandwidth of the transducer.

3.2.2 Tunable frequency

Due to the narrow bandwidth of the electro-optomechanical transducer detailed above it is critical that signals sent from a circuit QED system be on resonance with the microwave resonance of the transducer. Currently the electro-optomechanical transducers made in JILA are rather bespoke devices, as the fabrication process involves many steps and separate components, followed by extensive screening of devices to find a device with ideal parameters. Furthermore, the microwave resonant frequency of the transducer is formed by an LC circuit where $\omega_\mathrm{e} = 1/\sqrt{LC(x)}$ and

$$C(x) = \frac{\epsilon_\mathrm{o} A}{d - x} = \frac{C(0)}{1 - \frac{x}{d}}, \tag{3.2}$$

where the resonance frequency shifts significantly with the parallel plate capacitor separation d. In fact, it is desirable for the resonance frequency to vary significantly as a function of d, so as to maximize electromechanical coupling which scales as [83]:

$$g_{\mathrm{e}} = x_{\mathrm{zp}} \frac{d\omega_{\mathrm{e}}}{dx}\bigg|_{x=0} = x_{\mathrm{zp}} \frac{\omega_{\mathrm{e}}}{2d}, \tag{3.3}$$

where $x_{\mathrm{zp}} = \sqrt{\hbar/2\omega_{\mathrm{m}} m}$ is the zero-point motion of the mechanical oscillator, determined by the exact geometry, mass and tension of the silicon nitride membrane [83]. Thus it is ideal for d to be as small as possible to maximize this coupling. However, as the parallel plate capacitor geometry is formed by two separate chips that are epoxied together, it has been found that when cooling these devices to temperatures below 100 mK, the resonant frequency is subject to at a minimum 100 MHz variation between thermal cycles of the same device. Furthermore, when screening devices it is possible for the resonance frequency of the device to end up anywhere in the $4-8$ GHz microwave measurement band of the optical access dilution refrigerator. Thus a circuit QED system with a tunable resonance frequency is extremely important for efficiently coupling between the qubit and the transducer. Ideally, multiple circuit QED systems are prepared that can cover the whole microwave measurement band, and can be extensively tuned at the base temperature of the dilution refrigerator to bring the circuit QED system into resonance with the transducer.

The necessary tunability is achieved by attaching a sapphire rod to a piezoelectric stepping module with a maximum travel of approximately 5 mm at the base temperature of the dilution refrigerator. By advancing this sapphire rod so that it participates more in the circuit QED cavity's microwave resonance, it lowers the resonant frequency of the cavity. Using this technique I was able to fabricate two cavities: cavity A, which is tunable between $5.7-7.2$ GHz and cavity B, tunable between $6.8-8.5$ GHz, covering a large fraction of the microwave measurement band. Figure 3.2 demonstrates the internal loss rate $\kappa_{\mathrm{c,int}}$ and total linewidth κ_{c} of cavity A as a function of its resonant frequency ω_{c}. It is clear that the internal loss remains low and roughly constant over the entire tuning range of the cavity, with $\kappa_{\mathrm{c.int}}/2\pi \approx 4-10$ kHz, corresponding to internal quality factors of $Q_{\mathrm{int}} \sim 10^6$. Typically devices are pre-screened, and then one of these cavities can be

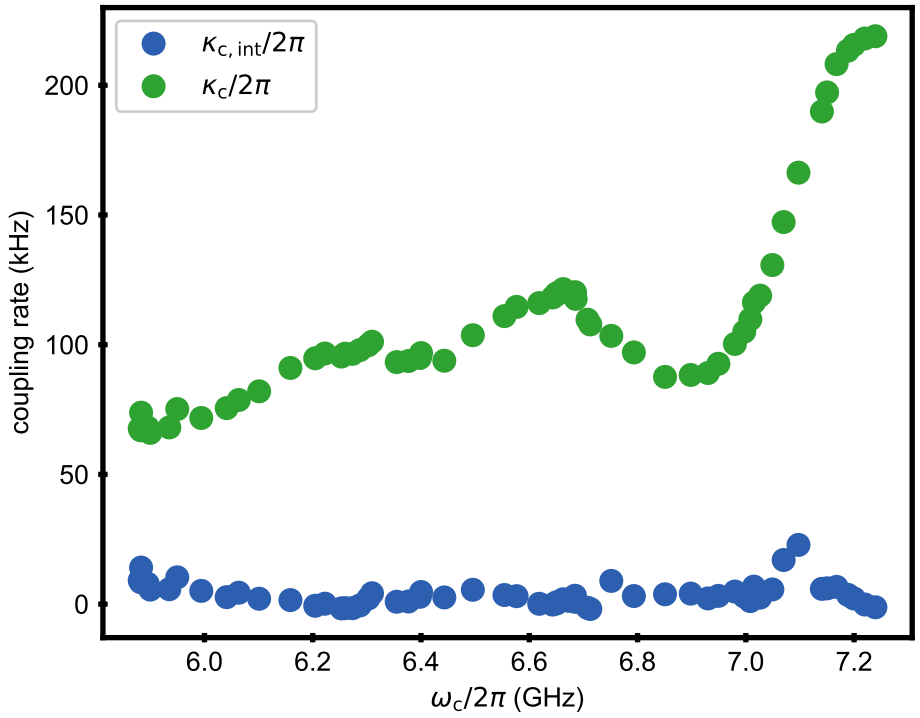

Figure 3.2: **Tunable microwave cavity coupling rates.** Internal loss rate $\kappa_{c,int}$ and total linewidth κ_c of cavity A. The external coupling rate changes significantly as a function of the sapphire rod position as it changes the distribution of the fields relative to the coupling pin—the non-monotonic dependence on frequency is expected from finite element analysis simulations. The blue points represent the internal loss (including the weakly coupled port, which may constitute a large fraction of this loss) of the resonator, which remains nearly constant over the entire tuning range of the cavity.

chosen and cooled down alongside the selected device. The non-monotonic behavior of κ_c as a function of ω_c (see Figure 3.2), which is dominated by changes in $\kappa_{c,ext}$, is due to the changing field distribution in the microwave cavity as the sapphire rod is translated, and is expected from finite element analysis simulations. Once the frequency of the electro-optomechanical transducer is known at low temperature, the sapphire rod can be tuned with the piezoelectric stepping module (attocube ANPz101 linear z-nanopositioner) such that $\omega_c = \omega_e$. See Section A.1 for technical details of the circuit QED system and Figure A.2 for a cross sectional view of a CAD model of the device.

While the cavity frequency is being tuned, it is also important that the properties of the

superconducting qubit remain relatively unchanged over the set of possible cavity frequencies. By changing the resonance frequency of the cavity, the detuning between the cavity and the qubit ($\Delta = \omega_c - \omega_q$) changes, which alters both the dispersive shift χ, and affects the Purcell limit for the qubit [84]:

$$\frac{1}{T_1} = \left(\frac{g}{\Delta}\right)^2 \kappa_c. \tag{3.4}$$

Thus it is important to check that both the lifetime and the coherence time of the qubit are not significantly affected by tuning the cavity. Such a measurement is shown in Figure 3.3 for cavity A, where he T_1 time of the qubit is largely unchanged over nearly the entire tuning range of the cavity.

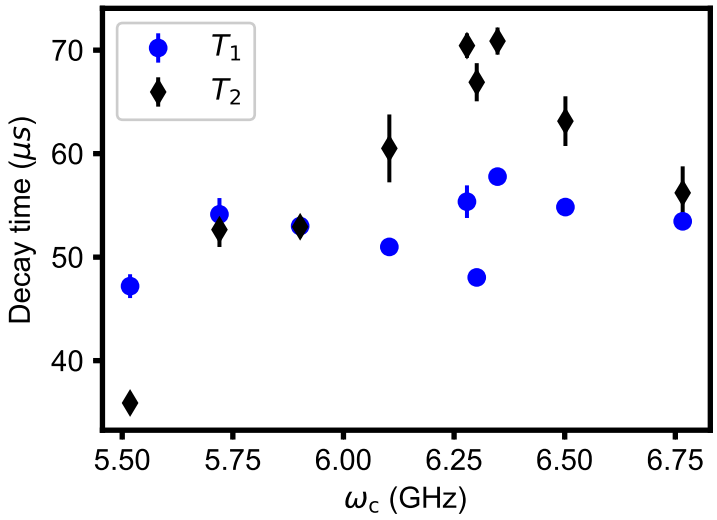

Figure 3.3: **Lifetime and coherence time of the qubit contained within Cavity A.** The T_1 and T_2 times are shown as a function of the cavity's resonant frequency.

Interestingly, while the coherence time remains relatively high for all frequencies of the cavity, there is a non-monotonic dependence of the T_2 time of the qubit on cavity frequency ω_c. While the dispersive shift between the fundamental mode of the cavity (see Figure 3.4) does have the expected monotonic dependence, the linewidth of the cavity κ_c (as seen in Figure 3.2) is not monotonic, and may explain the behavior of the T_2 time of the qubit. Additionally, there could be significant contributions to the dephasing of the qubit from higher modes of the cavity as the sapphire rod is

moved. Unfortunately, because these modes are outside of the $4-8$ GHz microwave measurement band it is not possible to characterize the effects of these modes quantitatively.

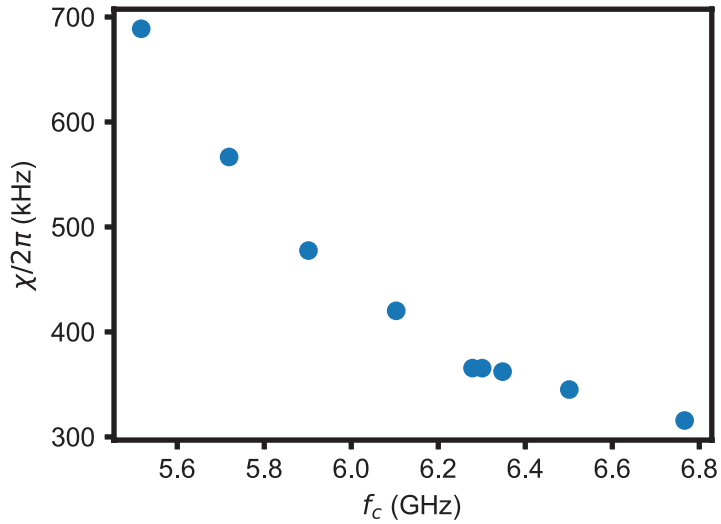

Figure 3.4: **Cavity A dispersive shift.** Dispersive shift χ of cavity A as a function of its frequency.

3.3 Input referred added noise

Ideally the transduction process should be entirely noiseless so that only signal photons are present at the output of the electro-optomechanical transducer. In practice, noise needs to be mitigated to a level where it does not significantly harm the fidelity of the state transfer, with the exact amount of added noise that can be tolerated depending upon the exact protocol being used [82]. In the case of linear detection, if more than 50% of the signal is noise such that the added noise in two quadratures $n_{\mathrm{add}} > 1/2$ is larger than that of vacuum fluctuations, then the non-classical properties of a quantum state will be lost. For example, there will no longer be any negativity in the Wigner function [85, 86], a frequently used measure of non-classicality.

In current devices [87, 69] the primary factor limiting quantum enabled transduction is noise generated in the LC circuit from the microwave pumps required for transduction. In Figure 3.5 the noise emitted by the microwave LC circuit N_{p} is shown both as a function of the number of pump photons circulating in the LC circuit n_{int} (top axis) and as a function of Γ_{e} (bottom axis). Note,

at $\Gamma_e = 50$ Hz, $N_p \approx 1$ photons/s/Hz, which precludes quantum transduction [82] even over a very narrow bandwidth.

Figure 3.5 also demonstrates how increases in g_e lead to direct reductions in N_p. Since $\Gamma_e \propto g_e^2 n_{int}$, for the same level of added noise N_p, a higher Γ_e can be achieved when g_e is increased. In the device described in [77] $g_e = 2\pi \times 1.6$ Hz was significantly suppressed relative to even previously fabricated devices, where $g_e = 2\pi \times 3.8$ Hz [56]. Ideally g_e can be made large enough such that it is possible to operate with $\Gamma_e \geq 1$ kHz, but with the noise significantly below $N_p < 1$. This would require an increase of g_e by approximately a factor of 10, assuming that all else remains constant. The anomalously low $g_e = x_{zp}\omega_e/2d = 2\pi \times 1.6$ Hz in this work is likely due to an anomalously large capacitor plate separation, equating to $d \approx 1$ µm, meaning that ideally one would like $d \approx 100$ nm to reduce the effects of this noise emitted by the microwave circuit. Wafer

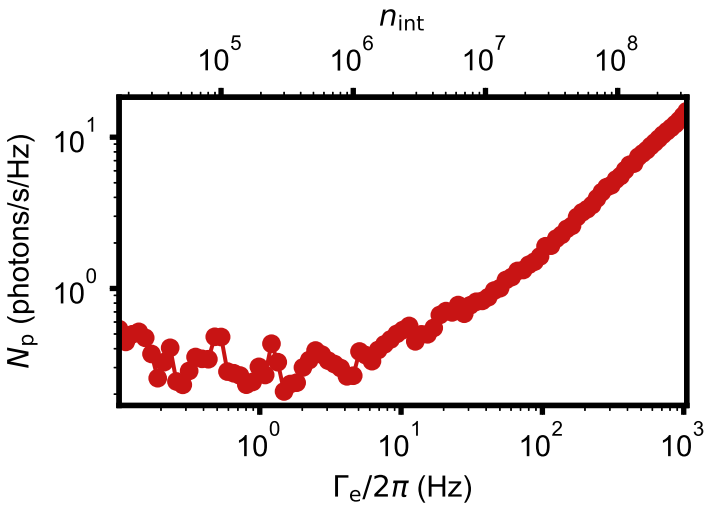

Figure 3.5: **Microwave LC circuit noise.** Parameter noise emitted by the microwave circuit N_p as a function of the number of photons circulating in the LC circuit n_{int} (top axis) and Γ_e (bottom axis).

bonding techniques are currently being explored to decrease the separation of the plates of the capacitor, but thermal contraction of the many different layers used in the flip chip geometry makes achieving this a challenge [69]. Another avenue for reducing N_p is to reduce the noise emitted by

the microwave circuit for a given value of n_{int}, in what amounts to essentially improving the power handling of the LC circuit. Because the source of N_{p} is currently not well understood this remains an outstanding challenge.

3.4 Interaction between the added noise and the efficiency

Loss is going to be a nearly fundamental component of any physically realizable quantum network since fiber optic cables suffer photon loss of at least 0.2 dB/km. However, in principle, heralding protocols [40, 41, 42, 88] can tolerate arbitrarily high levels of signal loss, so long as dark counts on the photon counter heralding the entanglement are far more infrequent than the arrival of real signal photons. However, in practice, these dark counts impose significant constraints on the amount of loss that can be tolerated in a remote entanglement experiment [89, 90, 91, 92]. This is because the noise at the output of the circuit QED system is the relevant metric for quantum transduction [82], but depends explicitly upon the transmission efficiency η_{loss} such that $N_{\mathrm{cQED}} = N_{\mathrm{det}}/\eta_{\mathrm{loss}}$, where here N_{det} is the noise at the input of the optical detector.

Dark counts at the detector can be generated intrinsically by the photon counting module, and in state of the art devices occur at mHz to Hz rates [93, 94, 95]. Alternatively, the electro-optomechanical transducer can itself generate noise photons, which behave equivalently to dark counts on the photon counting module. In the JILA transducers [67, 56, 69], the source of this noise is primarily due to the strong microwave pump generating noise in the microwave LC circuit (see Section 3.3), which is then transduced over to the optical domain. However, there are additional contributions from a small amount of laser induced noise [69] and finite sideband resolution causing the transducer to act as an amplifier, which means noise must be added during transduction [74].

To illustrate how noise and loss enters the system and influences the noise at the output of the circuit QED system N_{cQED}, a distributed beamsplitter model can be used. As an example, suppose there are two dominant sources of loss η_1 and η_2, which can be modelled as a beamsplitters with transmissivity η_{k} respectively. This model is illustrated in Figure 3.6, and at each beamsplitter, noise N_{i} can also enter through the dark port of the beamsplitter. I can then write the noise referred

to the output of the circuit QED system as:

$$N_{\mathrm{cQED}} = N_1 + \frac{N_2}{\eta_1}. \tag{3.5}$$

Hence the noise added later on in the transmission chain has a larger effect on the input referred added noise than the noise added at the signal input. This occurs because the noise N_1 gets attenuated the same amount as the signal before reaching the detector. This is a rather trivial result and is just the inverse effect of cascaded amplifiers, where due to the gain of the amplifier, input referred noise added after the initial amplifier is suppressed by the gain of earlier stages of the measurement chain [96].

This makes dark counts inherent to photon counters particularly damaging to the input referred added noise when transducing states from a circuit QED system to the optical domain. If the total transmission process has efficiency η_{loss}, then any dark noise at the input of the photodetector N_{d} will be enhanced such that $N_{\mathrm{cQED}} = N_{\mathrm{d}}/\eta_{\mathrm{loss}}$. This also makes it highly important to reduce the loss between the circuit QED system and the transducer, as any loss between these two devices will also increase N_{cQED}. This is one advantage of systems in which the superconducting qubit is integrated onto the same chip as the electro-optic transducer [62], as it can be engineered so that the majority of the signal makes it to the electro-optic transducer for frequency conversion.

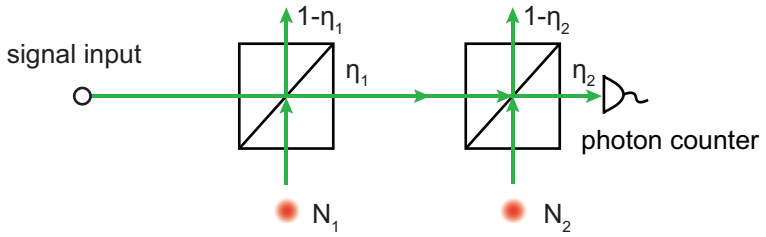

Figure 3.6: **Distributed beamsplitter model** demonstrating how multiple sources of loss/added noise contribute to the noise seen at the photon counting module/optical detector and at the signal input.

3.5 Repetition rate

The repetition rate of the experiment is a critical performance metric when coupling circuit QED systems to the electro-optomechanical transducer, as Γ_{rep} determines integration times for any experiment that requires averaging of many trials of the signal. Furthermore, in photon counting protocols, it also imposes a strict upper bound on the possible entanglement rates between remote qubits. In a real heralding experiment, any achieved entanglement rates will likely be several orders of magnitude lower than Γ_{rep} due to various sources of inefficiency reducing the probability of success.

Small repetition rates are actually a major limiting factor in several electro-optic transduction experiments. For example, in impressive recent results [62, 65] pulsed protocols were required to mitigate optical heating, since optical photons can easily generate quasiparticles in superconductors, which act as a source of noise in the microwave circuit. Additionally, optical dissipation in the dielectrics of the mechanical oscillator cause heating and can elevate the mechanical mode temperature [97]. To mitigate this, the laser field can be pulsed on for only a short period of time to avoid heating the sample. Assuming sufficiently large bandwidth, the short transduction pulse may be quite efficient, but the effects of quasiparticle generation take up to several milliseconds to dissipate, so Γ_{rep} is significantly reduced. Techniques to increase Γ_{rep} by switching to materials in which the superconductor has a much shorter quasiparticle lifetime are a current topic of research in the field.

The experiments in this work are also limited to a fixed experimental repetition rate, but instead this is due to the finite bandwidth of the electro-optomechanical transducer. The rather unique etalon design for the Fabry–Pérot cavity prevents light from the optical cavity from scattering onto the superconductor, and combined with the use of NbTiN as the superconductor in the microwave circuit, the transducer can be run continuously with little effect from the laser [69]. The energy decay rate of the silicon nitride membrane is determined by the total damping rate Γ_{T}, which means that one must wait for a time of at least $T_{\mathrm{wait}} > 5/\Gamma_{\mathrm{T}}$ so that the energy from

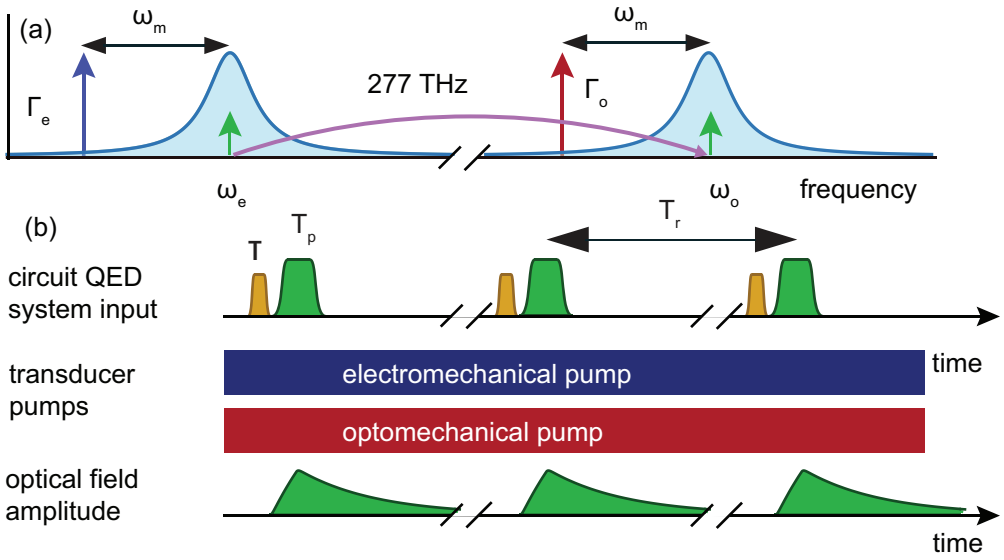

Figure 3.7: **Frequency and time domain operation of the transducer.** (a) Transducer pumps and experimental readout signals represented in the frequency domain. The electro(opto)-mechanical damping rates Γ_e (Γ_o) are controlled by the strength of the respective pumps, both red-detuned by ω_m to transduce microwave signals to the optical domain. (b) A pulse timing diagram illustrates the qubit (gold) and readout (green) pulses, with the experiment conducted with a repetition time of $T_r = 0.4 - 2$ ms and steady-state pumps. The upconverted readout pulse is filtered by the transducer's frequency response (bottom row), setting the minimum repetition time of the experiment T_r.

the pulse has decayed to less than 1% of its initial value. This is demonstrated schematically in Figure 3.7, which shows that one must wait for the amplitude of the filtered readout pulse to decay to a sufficiently low level before the protocol can be repeated. In the current device, since $\Gamma_T \leq 2\pi \times 6.1$ kHz for all measurements, this meant that the electro-optic transducer was indeed the limiting factor in the duty cycle as the decay rate of the qubit ($\Gamma_1 = \frac{1}{T_1} = 2\pi \times 9.3$ kHz) was larger. However in future devices, where we desire a qubit with $T_1 > 100$ µs [98, 99, 100], the qubit will actually be the limiting factor when it comes to duty cycle. However this can be easily addressed through active qubit reset protocols [101, 102, 103, 104, 88].

Chapter 4

Optically mediated superconducting qubit readout

4.1 Introduction

In this chapter I demonstrate optically mediated readout of a superconducting qubit, and then use the qubit as a non-Gaussian resource [77] to characterize the quantum efficiency of the electro-optomechanical transducer and optical measurement apparatus. This technique was originally developed to characterize the efficiency of parametric amplifiers used in superconducting qubit experiments [105, 106, 107, 108, 109], where it exploits the direct relationship between the dephasing induced by a weak measurement of the qubit and the signal-to-noise ratio of dispersive readout.

4.2 Dispersive readout of a superconducting qubit

4.2.1 Dispersive Hamiltonian

The Jaynes-Cummings model describes the interaction of a two level system with a resonant cavity [110]. In circuit QED, the two level system is the formed by the lowest two energy levels of an anharmonic LC circuit [111, 112, 113, 22], where the inductor consists of a single Josephson junction and the capacitor is a standard linear capacitor. In the rotating wave approximation the Jaynes-Cummings Hamiltonian is given by:

$$H_{\mathrm{JC}} = \hbar\omega_{\mathrm{c}}\hat{a}^{\dagger}\hat{a} + \hbar\omega_{\mathrm{q}}\frac{\hat{\sigma}_{\mathrm{z}}}{2} + \hbar g(\hat{a}\hat{\sigma}_{+} + \hat{a}^{\dagger}\hat{\sigma}_{-}). \tag{4.1}$$

It is frequently beneficial to operate with the atom and the resonator relatively far detuned from each other (ie. $|\Delta| = |\omega_{\mathrm{c}} - \omega_{\mathrm{q}}| \gg g, \kappa_{\mathrm{c}}, \kappa_{\mathrm{q}}$) such that instead of resonantly swapping atomic states

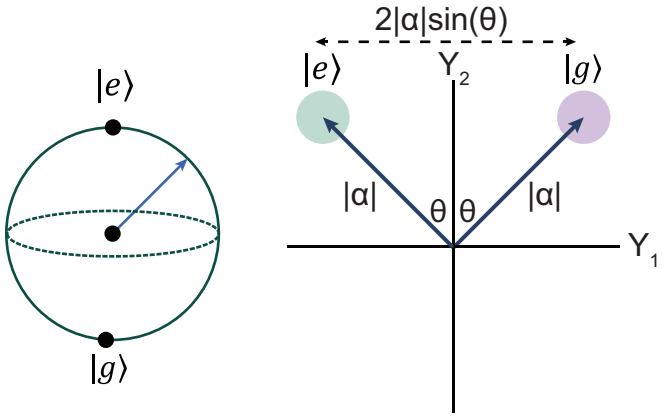

Figure 4.1: **Dispersive readout of a superconducting qubit.** The states |e⟩ and |g⟩ get mapped onto two phase shifted coherent states in the microwave cavity.

for excitations in the cavity, the Jaynes-Cummings interaction simply dresses the states of the cavity and the atom. To see this, the dispersive transformation can be performed such that $H \rightarrow U^{\dagger}HU$. The transformation is chosen to 'complete the square', and diagonalize the Hamiltonian to first order in $\frac{g}{\Delta}$ [114]:

$$U = \exp\left(\frac{g}{\Delta}(\hat{\sigma}_{-}\hat{a}^{\dagger} - \hat{a}\hat{\sigma}^{+})\right), \tag{4.2}$$

which gives the dispersive Hamiltonian:

$$H_{\mathrm{d}} = \hbar\left(\omega_{\mathrm{c}} + \frac{g^2}{\Delta}\hat{\sigma}_{\mathrm{z}}\right)\hat{a}^{\dagger}\hat{a} + \hbar\omega_{\mathrm{q}}\frac{\hat{\sigma}_{\mathrm{z}}}{2} + O\left(\frac{g^2}{\Delta^2}\right). \tag{4.3}$$

Where now the frequency of the resonator depends upon the state of the qubit, or equivalently, the average frequency of the qubit is dependent upon the average number of photons in the cavity $\langle\hat{a}^{\dagger}\hat{a}\rangle$. Thus, as is shown in Figure 4.1, if a coherent state α is injected into the microwave resonator with frequency near ω_{c}, the phase of the resulting output field will vary based upon the state of the qubit.

4.2.2 Optically mediated dispersive readout

This dispersive Hamiltonian forms the basis for much of modern circuit QED [20, 115], and enables readout of the superconducting qubit through a coupled microwave resonator. Inside of the microwave cavity, this readout process can be described by two coherent states $\alpha_{|\mathrm{g}\rangle}$ and $\alpha_{|\mathrm{e}\rangle}$ of

equal amplitude but differing phase (see Figure 4.1) corresponding to the qubit being in either the ground or the excited state. The angle θ shown in Figure 4.1 is determined by the dispersive shift χ and the linewidth of the circuit QED system's cavity κ_c:

$$\theta = \arctan\left(\frac{2\chi}{\kappa_c}\right) \tag{4.4}$$

However, by the time the coherent state propagates through the electro-optomechanical transducer and makes it to the optical detector (See Figure 3.1 for a schematic of the experimental apparatus), the optical heterodyne voltages are significantly modified by the act of transduction. First, the amplitude of the coherent state is reduced by loss through the measurement apparatus η_{loss}. Second, added noise converts the coherent states into mixed thermal states with variance larger than vacuum (see Figure 4.2). This noise can result from the optical detector itself, where for example heterodyne detection requires that noise equivalent to the variance of vacuum fluctuations be added [74], or result from the electro-optomechanical transducer imprinting noise onto the transduced readout signal—see Section 3.3.

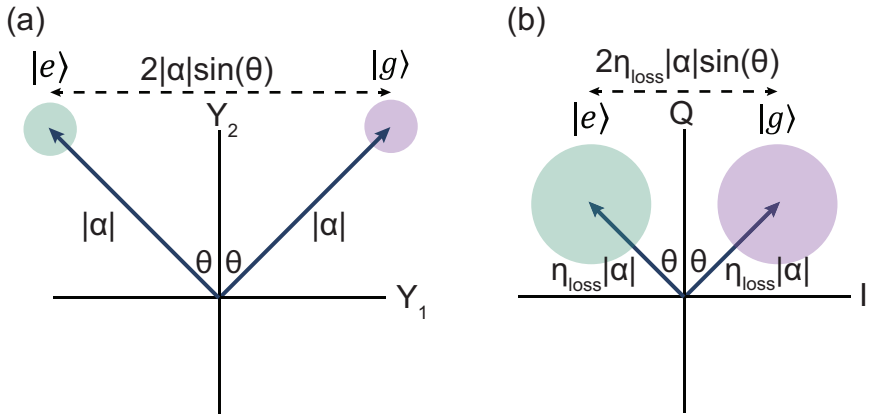

Figure 4.2: **Dispersive readout of a superconducting qubit with loss and noise.** (a) The states |e⟩ and |g⟩ get mapped onto two coherent states of opposite phase in the microwave domain with quadratures Y_2 and Y_1. (b) The microwave state is converted to the optical domain and detected on an optical heterodyne detector with voltage quadratures I and Q. Signal loss η_{loss} reduces the amplitude of the coherent state, while added noise increases the variance of the detected state. Both effects serve to reduce the SNR of the measurement.

4.3 Demonstrating readout of a superconducting qubit via the electro-optomechanical transducer

I demonstrate readout of the superconducting qubit by using the electro-optomechanical transducer to perform optically measured superconducting qubit experiments. To initialize the qubit state, a short qubit drive pulse with frequency ω_{d} and duration τ (gold pulse in Figure 4.3(a)) can be applied to the input line of the circuit QED system to induce Rabi oscillations in the qubit at a rate Ω_{r}. For $\tau = \pi/\Omega_{\mathrm{r}}$, the qubit population is inverted, and prepared mainly in the excited state $|e\rangle$. When no pulse is applied ($\tau = 0$), the qubit is prepared mainly in the ground state $|g\rangle$. State preparation is followed by a square readout pulse of length $T_{\mathrm{p}} = 15$ µs (green pulse in Figure 4.3(a)). The maximum useful length of the readout pulse, and hence the minimum pulse bandwidth, is determined by the lifetime of the qubit ($T_1 = 17$ µs) [80]. The pulse then travels through the cavity and is upconverted as described above, and the demodulated optical signal is digitized and integrated to extract a single voltage encoding the state of the qubit.

I first use this protocol to demonstrate single-shot optical readout of the superconducting qubit. By recording multiple voltage traces to form histograms of the qubit state-dependent optical heterodyne voltage, I can estimate the single-shot probability $P(e)$, and choose a voltage threshold V_{thresh} (see dashed line in Figure 4.3(b)) to maximize the fidelity $F_{\mathrm{opt}} = 1 - P(e|g) - P(g|e)$, where $P(e|g)$ ($P(g|e)$) is the probability of measuring $|e\rangle$ ($|g\rangle$) given that $|g\rangle$ ($|e\rangle$) was prepared. In Figure 4.3(b) I show histograms of the optical heterodyne voltage when preparing the qubit in either $|e\rangle$ or $|g\rangle$. The amplitude of the microwave readout pulse incident on the circuit QED system's microwave cavity is $\sqrt{\bar{n}_{\mathrm{r}}} = 19$ photons$^{1/2}$, and the electro-optomechanical transducer is operated continuously with $(\Gamma_{\mathrm{e}}, \Gamma_{\mathrm{o}})/2\pi = (0.5, 2.4)$ kHz to transduce the emitted microwave field to the optical domain for detection. A bimodal distribution is clearly visible in each histogram, with the two modes corresponding to the ground and excited states of the qubit.

The maximum optical readout fidelity of $F = F_{\mathrm{o}} \operatorname{erf}(\sqrt{2\eta_{\mathrm{q}} n_{\mathrm{r}}}) \approx 0.4$ is consistent with the measured quantum efficiency and a residual excited state population of $10 - 15\%$ in the qubit.

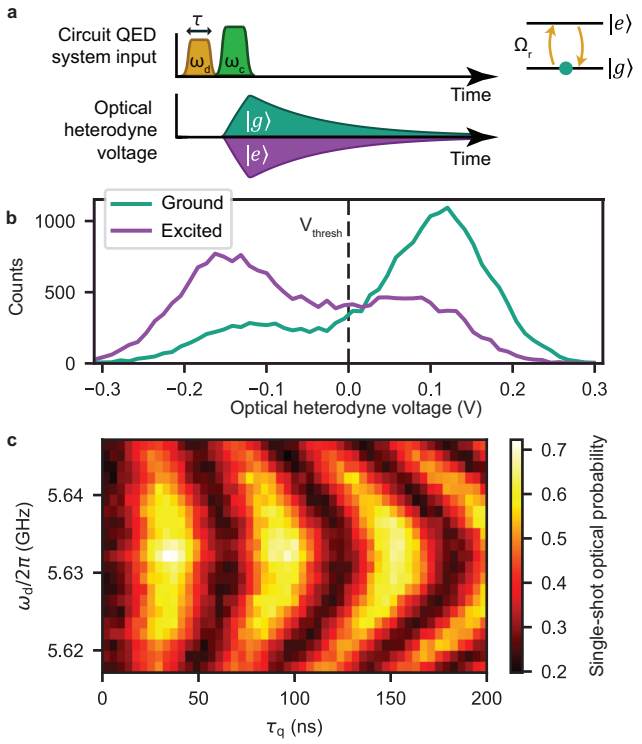

Figure 4.3: **Single-shot optical readout of a transmon qubit.** (a) A microwave drive pulse with frequency ω_d near the qubit frequency and length τ is applied to drive Rabi oscillations in the qubit at rate Ω_r. A microwave readout pulse centered around ω_c is sent through the cavity and subsequently transduced to the optical domain for optical heterodyne detection. The phase of the optical pulse depends on the state of the qubit. Pulse widths are not to scale for clarity. (b) Histogram of optical heterodyne voltage when reading out the superconducting qubit through the electro-optomechanical transducer. A 15 μs microwave pulse ($\sqrt{\bar{n}_\mathrm{r}} = 19$ photons$^{1/2}$) is applied to the microwave cavity to optically read out the state of the superconducting qubit when preparing it in the ground state (teal curve) or excited state (purple curve), with $(\Gamma_\mathrm{e}, \Gamma_\mathrm{o})/2\pi = (0.5, 2.4)$ kHz. The dashed line represents the voltage threshold V_thresh for single-shot readout. (c) Optically measured Rabi oscillations with the same readout pulse and transducer parameters above.

This residual occupancy is likely due to the relatively low attenuation (51 dB) between ambient temperature and the dilution refrigerator base plate on the microwave pump and cancellation lines [116], which is required to deliver the high-power microwave pump to the electro-optomechanical transducer. However, further work is needed to determine whether other aspects of the optical-access cryostat contribute to this thermal population in the qubit.

I can then use single-shot readout to measure Rabi oscillations of the superconducting qubit and demonstrate the stability of the optical measurement apparatus. To measure Rabi oscillations

I vary the qubit drive pulse length τ and the pulse frequency ω_{d} (Figure 4.3(c), with the same pulse amplitude and transducer damping rates as in Figure 4.3(b)). This measurement was taken over approximately 1.5 hours using a single threshold value chosen at the beginning of the experiment, indicating stability of the optical cavity lock and electro-optomechanical transducer over this period of time.

4.4 Two equivalent descriptions of linear measurement

When performing a linear measurement, the relevant figure of merit is typically the signal-to-noise ratio. Instead of characterizing both the noise and loss of the measurement apparatus separately, it can be useful to describe the measurement apparatus in terms of a single quantity known as the the quantum efficiency η_{q}, which contains two separate factors: the transmission loss η_{loss} and the contribution from the noise η_{noise}. Here I show how the noise measured at the input of the optical heterodyne detector, or equivalently at the output of an effective amplifier with gain η_{loss} (see Figure 4.4), can be expressed as a contribution to the quantum efficiency $\eta_{\mathrm{q}} = \eta_{\mathrm{loss}}\eta_{\mathrm{noise}}$, in which the optical readout apparatus can be modeled as an effective beamsplitter (see Figure 4.4).

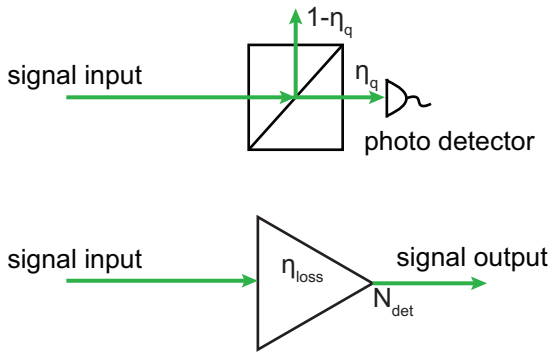

Figure 4.4: **Effective beamsplitter model.** A linear measurement can be characterized as an effective beamsplitter with efficiency η_{q} (top), or can equivalently be mapped onto to an effective amplifier model characterized by transmission efficiency due to loss η_{loss} and noise added at the output of the effective amplifier N_{det} (bottom). Both models are equivalent descriptions of linear measurement and transduction.

The voltage records obtained from the optical heterodyne detection of the upconverted qubit

readout pulse can be written in the form:

$$I_{|k\rangle}(t) = \sqrt{G_{\rm o}}\left(\sqrt{\kappa_{\rm c}\eta_{\rm loss}}{\rm Re}(\alpha_{|k\rangle}(t)) + \hat{\zeta}_{\rm I}(t)\right) \tag{4.5}$$

$$Q_{|k\rangle}(t) = \sqrt{G_{\rm o}}\left(\sqrt{\kappa_{\rm c}\eta_{\rm loss}}{\rm Im}(\alpha_{|k\rangle}(t)) + \hat{\zeta}_{\rm Q}(t)\right), \tag{4.6}$$

where $\sqrt{G_{\rm o}}$ is an overall gain factor and the index $k = \{g, e\}$ labels whether the qubit was prepared in the ground state or the excited state. $\eta_{\rm loss}$ includes *all* sources of loss between the circuit QED system and the ideal optical detector, while $\hat{\zeta}_{\rm I}$ and $\hat{\zeta}_{\rm Q}$ are noise operators whose autocorrelation functions include contributions from vacuum fluctuations, the added noise of an ideal heterodyne detector, and transducer added noise $N_{\rm t}$:

$$\langle\hat{\zeta}_{\rm I}(t)\hat{\zeta}_{\rm I}(t')\rangle = \langle\hat{\zeta}_{\rm Q}(t)\hat{\zeta}_{\rm Q}(t')\rangle = \frac{1}{2}(1 + N_{\rm t})\delta(t - t'). \tag{4.7}$$

Eqs. (4.5), (4.6), and (4.7) define the amplifier model described in Figure 4.4 in which the transduction process is characterized by an efficiency $\eta_{\rm loss}$ and total two-quadrature noise $N_{\rm det} = 1 + N_{\rm t}$ at the output of the ideal amplifier. However, as described above, for qubit readout it is often more convenient to combine these metrics into a single figure of merit. To this end, I can rescale Eqs. (4.5), (4.6) to obtain

$$I(t) = \sqrt{G'_{\rm o}}\left(\sqrt{\frac{\kappa_{\rm c}\eta_{\rm loss}}{1 + N_{\rm t}}}{\rm Re}(\alpha_{|k\rangle}(t)) + \tilde{\zeta}_{\rm I}(t)\right) \tag{4.8}$$

$$Q(t) = \sqrt{G'_{\rm o}}\left(\sqrt{\frac{\kappa_{\rm c}\eta_{\rm loss}}{1 + N_{\rm t}}}{\rm Im}(\alpha_{|k\rangle}(t)) + \tilde{\zeta}_{\rm Q}(t)\right), \tag{4.9}$$

where $\sqrt{G'_{\rm o}} = \sqrt{G_{\rm o}(1 + N_{\rm t})}$ is a modified overall gain factor, and $\tilde{\zeta}_{\rm I}$ and $\tilde{\zeta_{\rm Q}}$ are noise operators containing only contributions from vacuum fluctuations and ideal heterodyne detection: $\langle\tilde{\zeta}_{\rm I}(t)\tilde{\zeta}_{\rm I}(t')\rangle = \langle\tilde{\zeta}_{\rm Q}(t)\tilde{\zeta}_{\rm Q}(t')\rangle = \frac{1}{2}\delta(t - t')$. From Eqs. (4.8) and (4.9) it is clear that $\eta_{\rm q}$ can be defined as

$$\eta_{\rm q} = \eta_{\rm loss}\eta_{\rm noise} = \eta_{\rm loss} \times \frac{1}{1 + N_{\rm t}}. \tag{4.10}$$

Thus through a simple rescaling, the amplifier model can be directly mapped onto an effective beamsplitter describing the measurement apparatus.

4.4.1 Modeling the transducer's added noise

To obtain an expression for N_{t}, one can begin with the spectral density of the noise at the input of the optical heterodyne detector, which is measured directly at each pair of Γ_{e}, Γ_{o} values, corresponding to a total electro-optomechanical linewidth of $\Gamma_{\mathrm{T}} = \Gamma_{\mathrm{o}} + \Gamma_{\mathrm{e}} + \gamma_{\mathrm{m}}$. When normalized to the measured shot noise of the LO beam, the single-quadrature power spectral density in units of photons/s/Hz is given by

$$S_{\mathrm{out}}(\omega) = \frac{1}{2}(1 + S_{\mathrm{b}}) + \frac{\Gamma_{\mathrm{T}}^2}{4}\frac{S_{\mathrm{t}}(0)}{\frac{\Gamma_{\mathrm{T}}^2}{4} + \omega^2}, \tag{4.11}$$

where $S_{\mathrm{t}}(0)$ is the amplitude of the Lorentzian frequency response on resonance. The first term is the sum of equal contributions from vacuum fluctuations and the added noise of an ideal heterodyne detector, S_{b} encodes a small contribution from phase noise on the optical pump, and the Lorentzian term is due to fluctuations in the motion of the membrane imprinted on the reflected optical pump [69, 117]. The noise operator autocorrelation functions are obtained from the inverse Fourier transform of this spectrum:

$$\langle \hat{\zeta}_{\mathrm{I}}(t)\hat{\zeta}_{\mathrm{I}}(t')\rangle = \frac{1}{2}\left(1 + S_{\mathrm{b}}\right)\delta(t - t') + \frac{\Gamma_{\mathrm{T}}}{4}S_{\mathrm{t}}(0)e^{-\Gamma_{\mathrm{T}}|t-t'|/2}, \tag{4.12}$$

and $\langle \hat{\zeta}_{\mathrm{Q}}(t)\hat{\zeta}_{\mathrm{Q}}(t')\rangle = \langle \hat{\zeta}_{\mathrm{I}}(t)\hat{\zeta}_{\mathrm{I}}(t')\rangle$.

To obtain a single value encoding the state of the qubit, I perform a weighted integral of the two quadrature voltage records of the form [106]

$$V_{|k\rangle}(T_{\mathrm{int}}) = \int_0^{T_{\mathrm{int}}} \left[W_{\mathrm{I}}(t)I_{|k\rangle}(t) + W_{\mathrm{Q}}(t)Q_{|k\rangle}(t)\right]dt, \tag{4.13}$$

where I integrate the signal for a time T_{int} long enough such that all of the energy in the qubit readout pulse has decayed. The weights $W_{\mathrm{I}}(t)$ and $W_{\mathrm{Q}}(t)$ are chosen to optimize the SNR of the qubit readout [80] and to simplify the calculation of the quantum efficiency [106]:

$$W_{\mathrm{I}}(t) = \langle I_{|e\rangle}(t)\rangle - \langle I_{|g\rangle}(t)\rangle \tag{4.14}$$

$$W_{\mathrm{Q}}(t) = \langle Q_{|e\rangle}(t)\rangle - \langle Q_{|g\rangle}(t)\rangle. \tag{4.15}$$

The variance of this integrated voltage is then given by

$$\langle \Delta V^2_{|k\rangle}(T_{\rm int})\rangle = \int_0^{T_{\rm int}} \int_0^{T_{\rm int}} \left[W_{\rm I}(t) W_{\rm I}(t') \langle \hat{\zeta}_{\rm I}(t) \hat{\zeta}_{\rm I}(t') \rangle + \; W_{\rm Q}(t) W_{\rm Q}(t') \langle \hat{\zeta}_{\rm Q}(t) \hat{\zeta}_{\rm Q}(t') \rangle \right] dt \, dt' \tag{4.16}$$

Thus, I can define the total noise (in two quadratures) $N_{\rm det}$ at the input of the ideal optical heterodyne detector (where any inefficiency in the real optical detector has been included in $\eta_{\rm opt}$) in units of photons/s/Hz as

$$N_{\rm det} = 1 + N_{\rm t}, \tag{4.17}$$

where $N_{\rm t}$ is the noise added by the transducer,

$$N_{\rm t} = \frac{\Gamma_{\rm T} S_{\rm t}(0)}{4G(T_{\rm int})} \int_0^{T_{\rm int}} \int_0^{T_{\rm int}} \left[W_{\rm I}(t) W_{\rm I}(t') + \; W_{\rm Q}(t) W_{\rm Q}(t') \right] e^{-\Gamma_{\rm T}|t-t'|/2} \, dt \, dt' + S_{\rm b}, \tag{4.18}$$

and

$$G(T_{\rm int}) = \frac{1}{2} \int_0^{T_{\rm int}} \left[W_{\rm I}(t)^2 + W_{\rm Q}(t)^2 \right] \, dt. \tag{4.19}$$

4.5 Characterizing the quantum efficiency: theory

4.5.1 Superconducting qubit readout signal-to-noise ratio

In a dispersive measurement, a coherent state $|\alpha\rangle$ is entangled with the state of the qubit. If initially the qubit is prepared in a superposition state $|\psi_{\rm q}\rangle = \frac{1}{\sqrt{2}}(|e\rangle + |g\rangle)$, its interaction with the driven cavity mode causes it to evolve into the state

$$|\psi_{\rm m}\rangle = \frac{1}{\sqrt{2}} \left(|e\rangle |\alpha_{\rm e}\rangle + |g\rangle |\alpha_{\rm g}\rangle \right), \tag{4.20}$$

where $|\alpha_{\rm e}\rangle$ and $|\alpha_{\rm g}\rangle$ are coherent states with equal magnitude but phases shifted by $\theta_\pm = \pm \arctan 2\chi/\kappa_{\rm c}$, with the + (−) sign corresponding to the qubit in $|g\rangle$ ($|e\rangle$). The readout amplitude $\sqrt{\bar{n}_{\rm r}} = |\alpha| \sin\theta$ determines the separation in phase space between these two coherent states. The degree to which the two Gaussian distributions can be resolved in phase space is quantified by the signal-to-noise ratio (SNR): loss reduces the SNR by narrowing the phase space separation, while noise reduces the SNR by increasing the variance of each distribution. The SNR is defined as

$$\mathrm{SNR} = \frac{|\mu_{\rm e} - \mu_{\rm g}|}{\sigma_{\rm ge}}, \tag{4.21}$$

where $\sigma_{\mathrm{ge}} = \sigma_e = \sigma_g$ is the standard deviation of the Gaussian-distributed optical heterodyne voltage corresponding to the qubit in either the ground or the excited state, and μ_{g} and μ_{e} are the mean values of the two distributions. Noise N_{t} gets added by the transducer, and some of the signal is lost such that $|\alpha| \to \eta_{\mathrm{loss}}|\alpha|$; thus the SNR for a steady state readout tone can be written as

$$\mathrm{SNR} = \frac{2\sqrt{2}\eta_{\mathrm{loss}}|\alpha|\sin\theta}{\sqrt{1+N_{\mathrm{t}}}}. \tag{4.22}$$

4.5.2 Signal-to-noise ratio for a general pulsed measurement

For pulsed measurements the signal-to-noise ratio of qubit readout becomes slightly more complicated, where now using Equations 4.13, 4.14 and 4.15 and one can find that the readout contrast is given by:

$$S = |\langle V_{|e\rangle}(T_{\mathrm{int}})\rangle - \langle V_{|g\rangle}(T_{\mathrm{int}})\rangle|. \tag{4.23}$$

$$S = \kappa_{\mathrm{c}}\eta_{\mathrm{q}}G_0\int_0^{T_{\mathrm{int}}} |\alpha_{\mathrm{e}}(t') - \alpha_{\mathrm{g}}(t')|^2 dt'. \tag{4.24}$$

The noise was calculated in Equation 4.16, but can be simplified by using the vacuum noise autocorrelation functions $\langle\tilde{\zeta}_{\mathrm{I}}(t)\tilde{\zeta}_{\mathrm{I}}(t')\rangle = \langle\tilde{\zeta}_{\mathrm{Q}}(t)\tilde{\zeta}_{\mathrm{Q}}(t')\rangle = \frac{1}{2}\delta(t-t')$ along with the weights in Equations 4.14 and 4.15, giving the noise:

$$N = G_0\sqrt{\frac{1}{2}\kappa_{\mathrm{c}}\eta_{\mathrm{q}}\int_0^{T_{\mathrm{int}}} |\alpha_{\mathrm{e}}(t') - \alpha_{\mathrm{g}}(t')|^2 dt'}. \tag{4.25}$$

Thus the signal-to-noise ratio for any arbitrary pulsed measurement is given by:

$$\mathrm{SNR} = \sqrt{2\kappa_{\mathrm{c}}\eta_{\mathrm{q}}\int_0^{T_{\mathrm{int}}} |\alpha_{\mathrm{e}}(t') - \alpha_{\mathrm{g}}(t')|^2 dt'}. \tag{4.26}$$

4.5.3 Measurement induced dephasing

Reading out the state of the qubit through the cavity necessarily causes fluctuations in the frequency of the qubit due to the dispersive interaction between the qubit and the cavity—see

Equation 4.1. This leads to measurement-induced dephasing [118], where a projective (strong) measurement completely destroys the coherence of any initial superposition of the qubit. Using a master equation approach [118, 119] it can be shown that the effect of the measurement pulse dephases the qubit such that:

$$\Gamma_\phi = 2\chi \int_0^{T_{\rm int}} \mathrm{Im}(\alpha_{\rm e}^*(t')\alpha_{\rm g}(t'))dt'. \tag{4.27}$$

As was shown in [106], one can use the equations of motion for the qubit cavity:

$$\dot{\alpha}_{\rm e}(t) = -i(\Delta - \chi)\alpha_{\rm e}(t) - \frac{\kappa_{\rm c}}{2}\alpha_{\rm e}(t) + \sqrt{\kappa_{\rm c}}\alpha_{\rm in} \tag{4.28}$$

$$\dot{\alpha}_{\rm g}(t) = -i(\Delta + \chi)\alpha_{\rm g}(t) - \frac{\kappa_{\rm c}}{2}\alpha_{\rm g}(t) + \sqrt{\kappa_{\rm c}}\alpha_{\rm in}, \tag{4.29}$$

where Δ is the detuning from the microwave resonator's center frequency. Along with the additional requirement that all energy from the readout pulse decays on a timescale shorter than $T_{\rm int}$, one can then directly relate Γ_ϕ to the signal-to-noise ratio of the qubit measurement such that:

$$\Gamma_\phi = 2\chi \int_0^{T_{\rm int}} \mathrm{Im}(\alpha_{\rm e}^*(t')\alpha_{\rm g}(t'))dt' = \frac{\kappa_{\rm c}}{2}\int_0^{T_{\rm int}} |\alpha_{\rm e}(t') - \alpha_{\rm g}(t')|^2 dt'. \tag{4.30}$$

Using the above equation to eliminate the integral term in Equation 4.26 gives a very simple expression for the quantum efficiency [106]:

$$\eta_{\rm q} = \frac{4\mathrm{SNR}^2}{\Gamma_\phi} \tag{4.31}$$

4.6 Measurement-induced dephasing: experimental results

The off diagonal elements of a density matrix are the so-called coherence elements, which describe the (basis dependent) level of superposition between different quantum states. A measurement of length $T_{\rm p}$ has the effect of reducing the amplitude of these coherence elements [106, 109] by an amount:

$$\hat{\rho}_{\rm ge}(T_p) = \rho_{\rm ge}(0)e^{-\Gamma_\phi(T_p)}. \tag{4.32}$$

To estimate $|\rho_{\rm ge}/\rho_{\rm ge}(0)|$ one can perform a Ramsey sequence, where the coherence elements are given by $|\rho_{\rm ge}| = \langle|\sigma_{\rm z}|\rangle/4$. If one then injects a weak measurement pulse of length $T_{\rm p}$ into the Ramsey

sequence (see Figure 4.5(a)), and then measures the resulting amplitude of the Ramsey oscillations (see Figure 4.5(b) and Figure 4.6), this will give an estimate of the decay of ρ_{ge}. Figure 4.5(b) shows the results of these measurements, using the microwave readout apparatus and varying the strength of the weak 15 µs readout pulse. I observe a clear Gaussian decay of ρ_{ge} as a function of readout amplitude $\sqrt{n_{\mathrm{r}}}$. This measurement-induced dephasing quantifies the amplitude of the readout pulse inside of the circuit QED system's microwave cavity, while the SNR of the qubit readout quantifies the distinguishability of the two (thermal) coherent states at the optical detector.

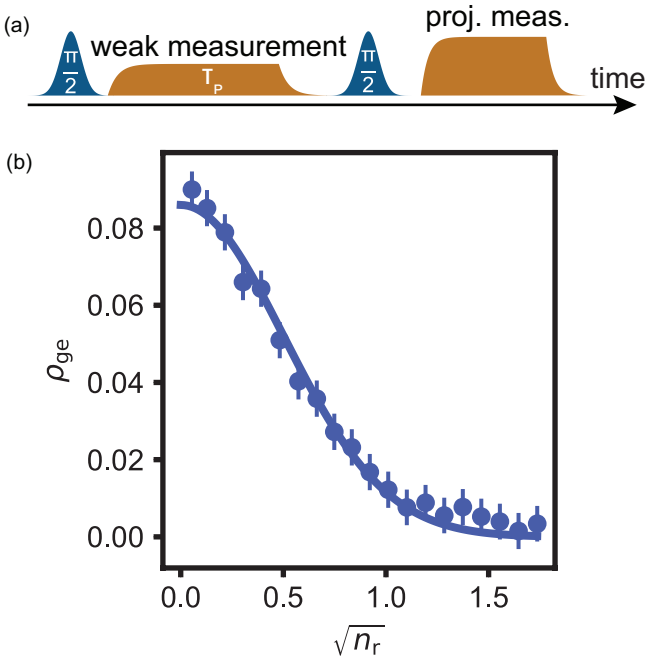

Figure 4.5: **Measurement induced dephasing.** (a) Protocol for measurement-induced dephasing calibration. A weak measurement pulse is injected into a Ramsey sequence. The Ramsey sequence is then followed by a strong projective measurement of the qubit. (b) The coherence of the qubit ρ_{ge} decays as a Gaussian function of the weak measurement amplitude $\sqrt{n_{\mathrm{r}}}$. The points are data, while the line is a Gaussian fit.

4.7 Characterizing the quantum efficiency of the optical readout apparatus

Having established the quantum efficiency as an unforgiving performance metric describing the optical measurement apparatus I plot η_{q} as a function of the total electro-optomechanical damping $\Gamma_{\mathrm{e}} + \Gamma_{\mathrm{o}}$ in Figure 4.7, where Γ_{e} is varied at several different fixed values of Γ_{o}. Using the

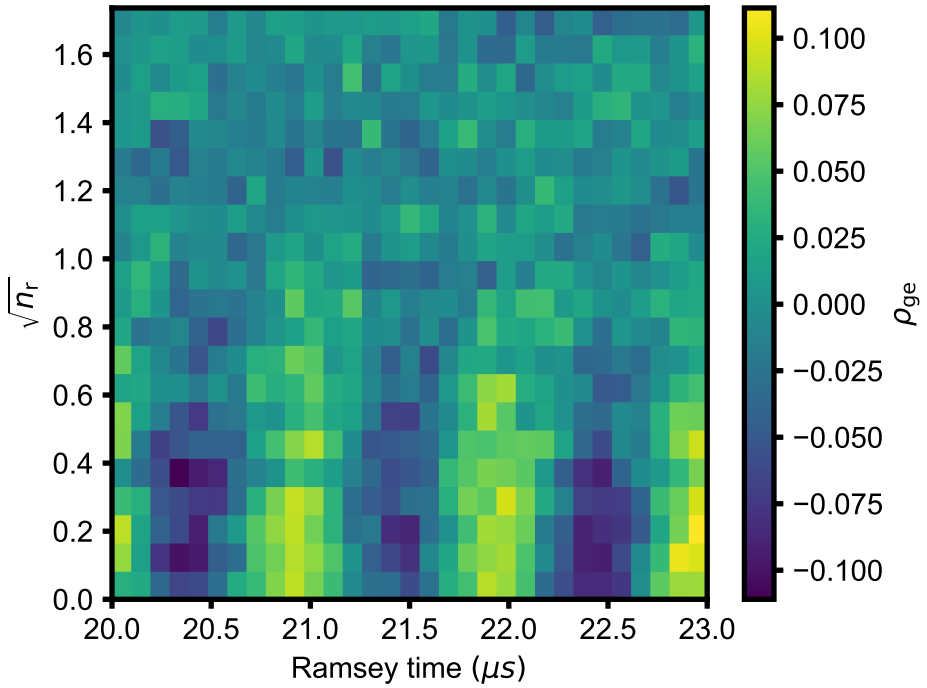

Figure 4.6: **Measurement induced dephasing Ramsey fringe data.** As the measurement strength is increased the amplitude of the Ramsey oscillations decreases as a Gaussian function of measurement amplitude $\sqrt{n_r}$. The Ramsey time (the separation between $\pi/2$ pulses) starts at 20 µs since the measurement pulse must fit within the Ramsey sequence.

.

state-space model (see Section 2.4) I perform a fit to η_q as $\Gamma_e + \Gamma_o$ is varied, with η_{mic} as the only free parameter. The fit results are plotted as dashed lines in Figure 4.7(c). This yields an *apparent* microwave loss of $\eta_{mic}^{app} = 0.17$, in slight tension with $\eta_{mic} = 0.34$ inferred from the microwave measurement described in Section 4.8.4. This discrepancy may be due to slight drifts in the optical cavity mode matching or microwave apparatus gain over time since the experiment was performed over the course of approximately 3 months. Two notable features are present in the quantum efficiency of the optically mediated superconducting qubit readout. First, the efficiency drops off significantly for $\Gamma_e \ll \Gamma_o$, which is due to both mismatched transduction (see Equation 4.37), as well as small transduction bandwidth $\Gamma_T = \Gamma_e + \Gamma_o + \gamma_m$. The efficiency also plateaus for large Γ_e due to Γ_e-dependent LC circuit loss and noise in the LC circuit that increases with Γ_e (see

Figure 3.5).

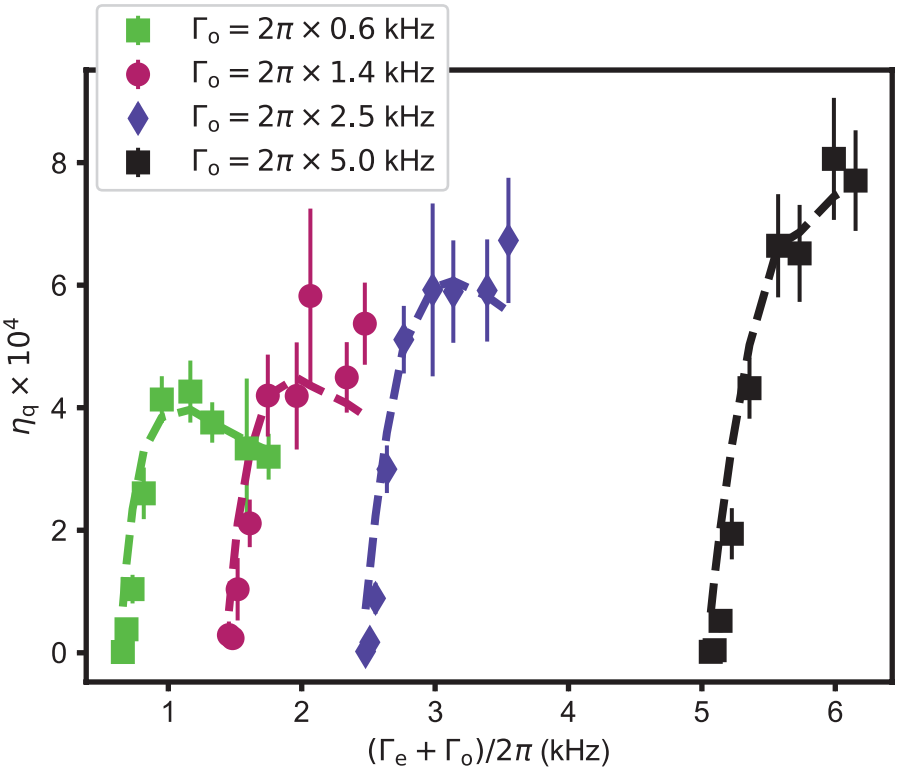

Figure 4.7: **Quantum efficiency of the optically mediated qubit readout.** The quantum efficiency is calibrated by comparing the signal-to-noise ratio of an optical qubit measurement to the total measurement-induced dephasing. For 20 Hz $\leq \Gamma_e/2\pi \leq$ 1100 Hz, Γ_e is varied for several fixed values of Γ_o and perform qubit readout measurements. The points are data from these measurements, while the dashed lines are a model using independently measured parameters of the electro-optomechanical transducer. The model includes all sources of inefficiency such as loss, added noise, and finite transduction bandwidth. All error bars represent one standard deviation.

4.7.1 Technical details of the quantum efficiency calibration

To control the readout amplitude $\sqrt{n_r}$ a drive voltage V is varied via an IQ mixer. The SNR and Gaussian decay of ρ_{ge} can be recast in terms of this drive voltage as:

$$\text{SNR} = aV \tag{4.33}$$

$$\rho_{ge} = \rho_{ge}(0)e^{-\frac{V^2}{2\sigma^2}} \tag{4.34}$$

which implies that $\Gamma_\phi = \frac{V^2}{2\sigma^2}$. Using Equations 4.33 and 4.34 in Equation 4.31 then gives a simple expression for the quantum efficiency:

$$\eta_{\mathrm{q}} = \frac{\sigma^2 a^2}{2}, \tag{4.35}$$

where in this convention an ideal heterodyne detector would have $\eta_{\mathrm{q}} = 1$. Thus to measure the data in Figure 4.7, I first measure the effects of a measurement pulse on the coherence of the qubit as in Figure 4.5. This can be completed using the microwave measurement apparatus, which is significantly more efficient than the optical measurement apparatus, as this measurement is only concerned with the effects of the pulse on the qubit. Second, for each Γ_{e} and Γ_{o} point, I sweep the measurement voltage V, and record histograms when preparing the qubit in both the ground and then the excited state (see Figure 4.3(b)). Finding the SNR as a function of V then enables the extraction of a, and subsequently η_{q}.

4.8 Contributions to the quantum efficiency

Since the quantum efficiency describes *all* sources of loss and added noise resulting from the optically mediated readout, there exist many different contributions to the final value, all of which are described in this Section. The quantum efficiency of the optically mediated qubit readout apparatus can be split into seven main components, $\eta_{\mathrm{q}} = \eta_{\mathrm{bw}}\eta_{\mathrm{t}}\eta_{\mathrm{G}}\eta_{\mathrm{mic}}\eta_{\mathrm{opt}}\eta_{\mathrm{cav}}\eta_{\mathrm{noise}}$. I describe each contribution below, and the contributions are also summarized in Table 4.1. Note the first three contributions to the quantum efficiency η_{bw}, η_{t} and η_{G} are theoretically calculated from the known transducer operating parameters and are discussed in Section 2.4. The rest of the contributions are technical sources of loss and added noise.

4.8.1 Bandwidth limitations: η_{bw}

A significant contribution to η_{q} is due to the mismatch in bandwidth between the transducer and the readout pulse emitted by the qubit cavity. In the rotating wave approximation,

Table 4.1: Contributions to the quantum efficiency $\eta_q = \eta_{bw}\eta_t\eta_G\eta_{mic}\eta_{opt}\eta_{cav}\eta_{noise}$. Numerical values are not reported for contributions that depend on Γ_e and Γ_o.

Parameter	**Symbol**	**Value**
Finite bandwidth	η_{bw}	see Equation (4.36)
Transducer efficiency	η_t	See Equation (4.37)
Transducer gain	η_G	See Equation (4.38)
Microwave transmission loss	η_{mic}	$\eta_{mic} = 0.34$
Optical detection efficiency	η_{opt}	$\eta_{opt} = 0.28$
Circuit QED system cavity loss	η_{cav}	$\eta_{cav} > 0.96$
Added noise	η_{noise}	$\eta_{noise} = (1 + N_t)^{-1} = N_{det}^{-1}$

approximating the circuit QED system's output as a square pulse with width T_p, obtaining

$$\eta_{bw} \approx 1 - 2\frac{\left(1 - e^{-\Gamma_T T_p/2}\right)}{\Gamma_T T_p}. \tag{4.36}$$

Using the state space model outlined in Section 2.4, I solve for the full dynamics without the above approximations to give a contribution to the efficiency in the range $0.02 < \eta_{bw} < 0.19$ over the range of Γ_T values plotted in Figure 4.7. It is possible to increase η_{bw} significantly by either increasing the length of the signal emitted by the circuit QED system T_p, or by increasing the total bandwidth of the electro-optomechanical transducer Γ_T.

4.8.2 Transducer efficiency: η_t

The relatively low electromechanical coupling in this device ($g_e = 2\pi \times 1.6$ Hz) limits the maximum achievable electromechanical damping rate to $\Gamma_e = 2\pi \times 1.1$ kHz. To maximize bandwidth the transducer is often operated in a mismatched mode with $\Gamma_o \gg \Gamma_e$, but this comes at a cost to the narrowband signal efficiency of the transducer [69]:

$$\eta_t = \epsilon\frac{\kappa_{o,ext}}{\kappa_o}\frac{\kappa_{e,ext}}{\kappa_e}\frac{4\Gamma_e\Gamma_o}{\Gamma_T^2}, \tag{4.37}$$

which sets an upper bound on the efficiency with which broadband signals can be transduced. Equation (4.37) also depends on Γ_e implicitly due to the pump power-dependent LC circuit loss. This contribution is responsible for the sharp drop in efficiency for $\Gamma_e \ll \Gamma_o$ on each curve in Figure 4.7, and is largely responsible for the plateau at high Γ_e for each fixed value of Γ_o.

4.8.3 Transducer gain: η_{G}

Due to the finite sideband resolution of the electro-optomechanical system [79], the transducer has gain [67]

$$\eta_{\mathrm{G}} = \left(1 + \left(\frac{\kappa_{\mathrm{e}}}{4\omega_{\mathrm{m}}}\right)^2\right)\left(1 + \left(\frac{\kappa_{\mathrm{o}}}{4\omega_{\mathrm{m}}}\right)^2\right). \tag{4.38}$$

This two-quadrature gain is undesirable for transduction, as it is necessarily accompanied by unwanted added noise [74], but it is a small effect, varying in the range $1.3 < \eta_{\mathrm{G}} < 1.5$ with microwave pump power. This gain is intrinsically linked to the added noise, as the transducer can be be described as a phase preserving amplifier with gain η_{G} [74].

4.8.4 Microwave transmission loss: η_{mic}

The experimental system also permits qubit readout through a microwave readout apparatus by reflecting the readout signal off of the electro-optomechanical transducer (shown in Figure 3.1). Its quantum efficiency $\eta_{\mathrm{q}}^{\mathrm{mic}}$ is defined to include all sources of loss and noise that affect the readout pulse as it emerges from the circuit QED system's cavity, reflects off the transducer's LC circuit, and is detected using the microwave heterodyne measurement apparatus. The quantum efficiency of the microwave apparatus can be split into four separate components such that:

$$\eta_{\mathrm{q}}^{\mathrm{mic}} = \eta_{\mathrm{mic}}\eta_{\mathrm{HEMT}}\eta_{\mathrm{noise}}\eta_{\mathrm{ref}}. \tag{4.39}$$

The first two parameters characterize transmission losses, where η_{mic} represents the loss between the circuit QED system and the electro-optomechanical transducer, and is the parameter I wish to extract from these quantum efficiency measurements. η_{HEMT} accounts for the loss between the electro-optomechanical transducer and the high-electron-mobility transistor (HEMT) amplifier, and is characterized by an independent electro-mechanical temperature sweep to be $\eta_{\mathrm{HEMT}} = 0.26$ [69]. The contribution from added noise η_{noise} takes into account the added noise of the HEMT and noise emitted by the LC circuit. The circuit reflection loss η_{ref} is a function of the power dependent

linewidth of the LC circuit since in the steady state:

$$\eta_{\mathrm{ref}} = |S_{11}|^2 = \frac{\Delta^2 + (\kappa_{\mathrm{e}} - 2\kappa_{\mathrm{e,ext}})^2/4}{\Delta^2 + \kappa_{\mathrm{e}}^2/4}, \tag{4.40}$$

where $\Delta = \omega - \omega_{\mathrm{e}}$ is the detuning of the probe field. Since the circuit is close to critically coupled at the maximum incident pump power of -45 dBm ($\Gamma_{\mathrm{e}} = 2\pi \times 1.1$ kHz), with $\kappa_{\mathrm{e}}/2\kappa_{\mathrm{e,ext}} = 0.97$, this LC circuit reflection loss is a large contribution to $\eta_{\mathrm{q}}^{\mathrm{mic}}$ at high pump powers and is responsible for the shape of the curve in Figure 4.8.

The signal emitted by the qubit cavity has finite bandwidth, and as a result a significant fraction of the energy of the qubit readout pulse will be detuned from the resonator. To account for this I estimate the energy of the circuit QED system's output field by solving the set of equations for the output of the qubit cavity:

$$\dot{\hat{\alpha}} = \left(-i(\Delta \pm \chi) - \frac{\kappa_{\mathrm{c}}}{2}\right)\hat{\alpha} + \sqrt{\kappa_{\mathrm{c,w}}}\hat{\alpha}_{\mathrm{in,w}}(t) + \sqrt{\kappa_{\mathrm{c,ext}}}\hat{\alpha}_{\mathrm{in}}(t) \tag{4.41}$$

$$\hat{\alpha}_{\mathrm{out,w}} + \hat{\alpha}_{\mathrm{in,w}} = \sqrt{\kappa_{\mathrm{c,w}}}\hat{\alpha} \tag{4.42}$$

$$\hat{\alpha}_{\mathrm{out}} + \hat{\alpha}_{\mathrm{in}} = \sqrt{\kappa_{\mathrm{c,ext}}}\hat{\alpha}, \tag{4.43}$$

where the qubit readout pulse is applied to the weak port with coupling rate $\kappa_{\mathrm{c,w}}$ and the other port of the qubit cavity directs energy towards the electro-optomechanical transducer with coupling rate $\kappa_{\mathrm{c,ext}}$. The parameter Δ is the detuning of the pulse from cavity resonance, while the $+$ $(-)$ sign corresponds to the case where the qubit is prepared in the ground (excited) state.

$$\hat{\alpha}_{\mathrm{in,w}}(t) = \hat{\alpha}_{\mathrm{in,o}}(\Theta(t) - \Theta(t - T_{\mathrm{p}})) \tag{4.44}$$

is described by a square pulse of length T_{p}, where $\Theta(t)$ is the Heaviside step function. Equivalently the equations of motion can be solved in reflection off the electro-optomechanical transducer where the fields are described by:

$$\dot{\hat{b}} = -\left(i\Delta + \frac{\kappa_{\mathrm{e}}}{2}\right)\hat{b} + \sqrt{\kappa_{\mathrm{e,ext}}}\hat{b}_{\mathrm{in}} \tag{4.45}$$

$$\hat{b}_{\mathrm{out}} + \hat{b}_{\mathrm{in}} = \sqrt{\kappa_{\mathrm{e,ext}}}\hat{b}, \tag{4.46}$$

and the efficiency η_{ref} for a broadband pulse can be calculated as:

$$\eta_{\mathrm{ref}} = \frac{\int |\hat{b}_{\mathrm{out}}(t)|^2 dt}{\int |\hat{\alpha}_{\mathrm{out}}(t)|^2 dt}. \tag{4.47}$$

Measuring $\eta_{\mathrm{q}}^{\mathrm{mic}}$ allows for the retrieval of the microwave transmission loss η_{mic} between the circuit QED system and the transducer. As shown in Figure 4.8, $\eta_{\mathrm{q}}^{\mathrm{mic}}$ decreases significantly with increasing Γ_{e}. This data is fit to a model (purple curve in Figure 4.8) that includes the effects of Γ_{e}-dependent LC circuit reflection loss, noise emitted from the microwave port of the transducer, and independently calibrated microwave measurement apparatus added noise referred to the transducer output [69], with η_{mic} as the only free parameter, yielding $\eta_{\mathrm{mic}} = 0.34$ (4.7 dB). This relatively high level of loss can be mitigated by reducing the total number of microwave connectors in the signal path, switching to superconducting cables, and removing filters from the signal path and placing them instead on the pump and cancel lines.

4.8.5 Optical detection efficiency: η_{opt}

The optical detection efficiency is given by the product of factors encoding optical transmission losses between the transducer and the balanced heterodyne detector, the inefficiency of the heterodyne detector itself, and the detector's dark noise: together these three factors yield $\eta_{\mathrm{opt}} = 0.28$. This figure excludes optical cavity losses and imperfect mode matching, which are included in Equation (4.37) as they are an inherent part of the electro-optomechanical transducer.

4.8.6 Circuit QED system cavity loss: η_{cav}

Through the measured attenuation on the lines, the sum of the of the weak port coupling and the internal loss to $\kappa_{\mathrm{c,int}} + \kappa_{\mathrm{c,w}} < 2\pi \times 15$ kHz can be bounded. Thus $\eta_{\mathrm{cav}} = 1 - \frac{\kappa_{\mathrm{c,int}} + \kappa_{\mathrm{c,w}}}{\kappa_{\mathrm{c}}} > 0.96$ does not significantly affect η_{q}. Although there are no detailed measurements as a function of the resonant frequency of cavity B, from measurements on cavity A, the loss is well below 15 kHz over the entire tuning range of the cavity—see Figure 3.2.

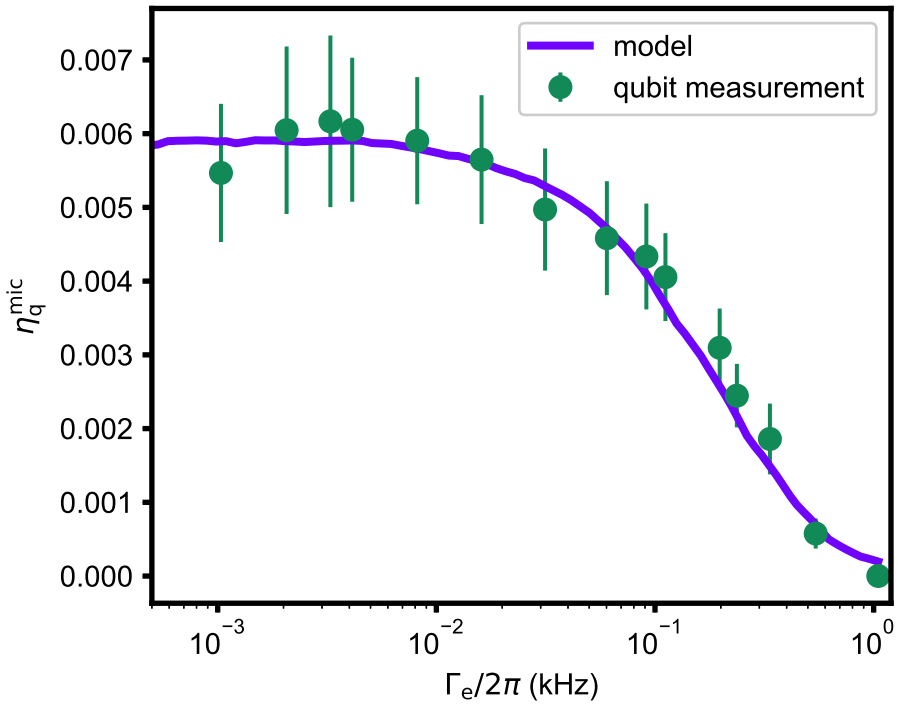

Figure 4.8: **Characterization of the quantum efficiency of the microwave readout apparatus.** The microwave readout efficiency η_q^{mic} is measured as a function of the electromechanical damping rate Γ_e. The points are data, while the line is a model including partial absorption of the readout pulse by the pump power-dependent reflection loss of the LC circuit, power-dependent added noise, fixed transmission losses and the independently measured added noise of the microwave heterodyne measurement apparatus. The shape of the curve is dominated by power-dependent LC circuit reflection loss, with the quantum efficiency of the microwave readout apparatus approaching zero at high power because the LC circuit is nearly critically coupled. From this, I estimate 4.7 dB of loss ($\eta_{mic} = 0.34$) between transducer and the circuit QED system.

4.9 The transmission loss and comparison to other results

For comparison to other results, I can independently measure the output noise of the transducer N_t, and divide out its contribution to the quantum efficiency (see Section 4.4) to retrieve the transmission loss:

$$\eta_{loss} = \eta_q/\eta_{noise} = \eta_q(1 + N_t) \tag{4.48}$$

This transmission loss is an important figure of merit as it ultimately will contribute to an upper bound on possible entanglement rates between remote qubits (see Section 3.5), and it represents the

practical amount of signal that one has transduced all the way to the end of the optical measurement apparatus. I plot the transmission efficiency as a function of $\Gamma_e + \Gamma_o$, where a maximum value of approximately 2×10^{-3} is achieved.

While the above result for η_{loss} may seem low, especially when compared to previous results from JILA where the *transducer* efficiency was $\eta_t = 47$ % [56], η_{loss} takes into account *all* sources of inefficiency from the transduction process. Thus η_t is only a small contribution to $\eta_{loss} = \eta_{bw}\eta_t\eta_G\eta_{mic}\eta_{opt}\eta_{cav}$, since it contains many different contributions, nearly all of which are far from unity. This technique of characterizing the total transmission loss contrasts previous results from JILA [67, 56, 69], as well as other groups [65] where the performance of only the electro-optic transducer itself was characterized. It is perfectly valid to characterize just the performance of the transducer itself (characterized by η_t), but it does not capture all of the sources of loss that will be relevant for networking remote superconducting qubits.

In Table 4.2 I compare the results shown in this work with other recent results in the field. The important figures of merit are the transmission efficiency η_{loss}, the input referred added noise of the transducer, the repetition rate of the experiment, and whether qubits were integrated. Note that the integration of qubits entails extra experimental constraints, and can significantly reduce the efficiency and increase the added noise. For example [69] had qubits integrated with the transducer, but the qubit was unused during the characterization of the transducer, which moves the reference plane for the efficiency and added noise up to the input of the converter—see Figure 4.9. That fact, combined with the use of narrowband signals, lead to orders of magnitude higher efficiency and orders of magnitude lower added noise than in [77], which used the same experimental apparatus. This is why the results that do no integrate qubits [69, 65] may seemingly have significantly better performance than the two lone results that have integrated qubits into the experiment [77, 62].

Table 4.2: Recent electro-optic transduction results

Reference	η_{loss}	**Added noise at input (photons/s/Hz)**	**Repetition rate (kHz)**	**Integrates qubits**
Delaney *et al.* (2021), [77]	2×10^{-3}	740	2.5	yes
Mirhosseini *et al.* (2021), [62]	9×10^{-5}	0.6	0.1	yes
Sahu *et al.* (2021), [65]	0.09-0.15	0.16	0.01-0.5	no
Brubaker *et al.* (2021), [69]	0.47	3.2	continuous	no
Forsch *et al.* (2020), [60]	1.6×10^{-5}	> 100000	continuous	no

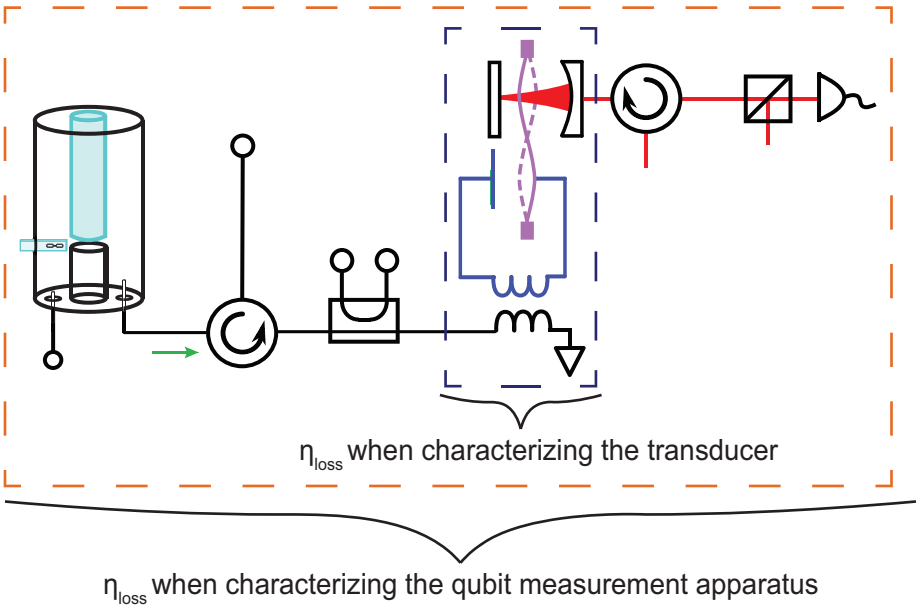

Figure 4.9: **Differences in efficiency characterization.** The large orange box highlights all of the components that are included when calibrating η_{loss} of the qubit measurement apparatus [77]. While the small purple box highlights the efficiency number that is calibrated when simply characterizing the electro-optic transducer [69, 56, 67]. The different reference planes are used because *all* sources of loss are important when sending signals from a superconducting qubit to an optical detector, but when characterizing the performance of *only* an electro-optic transducer it is important to characterize the performance of the device itself.

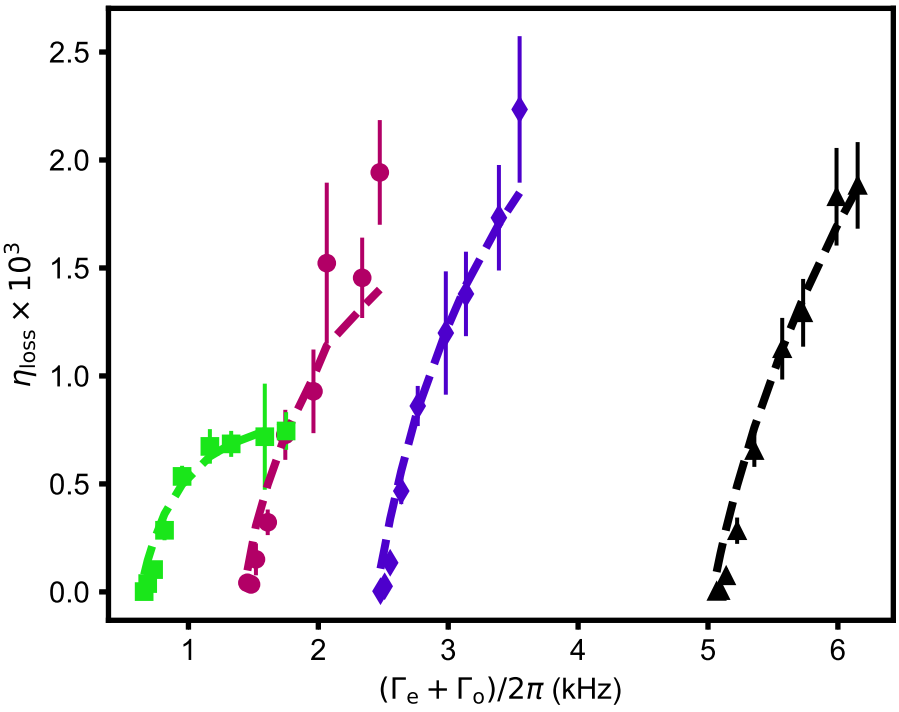

Figure 4.10: **Transmission loss.** Transmission loss η_{loss} (scaled by a factor of 10^3) as a function of the total electro-optomechanical damping rate $\Gamma_{\mathrm{T}} = (\Gamma_{\mathrm{e}} + \Gamma_{\mathrm{o}})/2\pi$. η_{loss} includes *all* sources of loss between the circuit QED system and the optical heterodyne detector at the end of the optical measurement apparatus. The points are data from qubit and optical noise measurements. The lines are the independently measured and calculated efficiency using only linear measurements.

Chapter 5

Characterization of backaction from the electro-optic transducer

5.1 Motivation

Backaction is fundamental to quantum mechanics, as the act of measurement necessarily involves interaction between the system of interest and the detector, and according to the Heisenberg uncertainty principle, as you learn more about an observable (for example the position of a particle $\hat{x}$) there becomes more uncertainty about the value of the conjugate observable (in this case, the momentum $\hat{p}$). No matter the system, the backaction depends fundamentally upon the strength of the measurement, and the system upon which the backaction is imparted is agnostic as to whether the measurement is being performed by an experimentalist carefully monitoring the signal, or by the environment, through degrees of freedom that the experimentalist has no access to. It is this later form of 'measurement' backaction by the environment that is most problematic in circuit QED, as thermally generated photons from noise propagating down signal and control lines [120, 121] can make it into the circuit QED system, and 'measure' the state of the qubit. It is also this unintentional injection of photons into the circuit QED system by the electro-optic transducer, either coherently from the microwave pumps, or through heating, that this chapter is concerned with.

In the context of electro-optic transduction, backaction is an extremely important figure of merit. An electro-optic transducer in principle can impart no backaction, as transduction is a purely unitary operation (see Section 2.2 and [122]). However, due to experimental non-idealities, including accidental measurement, or heating by laser and/or microwave pumps, backaction can be

rather significant and is an important performance metric for a real electro-optic transducer.

As an example, the microwave pump used to mediate the transduction process in the experiments shown in this thesis has a maximum incident power of $P_{\text{inc}} = -45$ dBm, which if it were incident on the circuit QED system would result in $\sim 2{\times}10^8$ photons in the circuit QED system's microwave cavity. This level of power in the circuit QED system vastly exceeds $n_{\text{crit}} = \Delta^2/4g^2 = 302$, the photon number at which the dispersive approximation breaks down [123, 22]. Thus, not only is there significant potential for backaction on the qubit from the pumps, it is possible to drive the the qubit out of the dispersive regime, driving the qubit out of its computational basis and effectively rendering it useless. Additionally, if optical photons are incident on the superconducting qubit,or significantly heat the substrate, as was the case in [62], then quasiparticles will be generated, also effectively rendering the qubit unusable for a several millisecond time scale until the quasiparticles have decayed—preventing continuous operation of the transducer. In both of these cases this is much worse than backaction—which simply erases phase information—and instead is destructive to the state (and even the existence) of the qubit during operation of the electro-optic transducer.

5.2 Backaction in circuit QED

The coherence time (T_2 time) of a qubit describes the characteristic time that phase information can be stored in a qubit, and is determined both by its lifetime and any additional sources of dephasing T_ϕ, such that:

$$\frac{1}{T_2} = \frac{1}{2T_1} + \frac{1}{T_\phi}. \tag{5.1}$$

In circuit QED, shot noise, which arises from the discrete nature of photons, randomly shifts the resonance frequency of the qubit coupled to the microwave cavity through the dispersive interaction. This shot noise can result from measurement induced dephasing, where a coherent state dephases the qubit, and will be discussed in Section 5.4.1, and has been studied in both circuit QED [118] and cavity QED [124, 125, 126]. Additionally, as will be discussed in Section 5.4.2, dephasing can occur due to thermal photons incident on the circuit QED system [127], with this thermal dephasing

being one of the primary factors limiting coherence times in circuit QED systems today [120, 121].

5.2.1 Implications for the remote entanglement of qubits

Preserving the qubit in its prepared state is particularly important for the implementation of heralding protocols when encoding qubits in bosonic fields [128, 88, 129], or for heralding remote entanglement between two spatially separated qubits [43]. For example, using diamond NV centers [130, 131], a memory qubit is required to store the quantum state for entanglement distillation between remote qubits. However, if the operation of the transducer disrupts the state of the memory qubit, then this will also certainly disrupt the entanglement between the remote qubits.

A simple example of this, more centered around transmon qubits, involves driving the blue sideband transition between the microwave cavity at frequency ω_c and qubit at ω_q to generate single photons [132, 133, 134, 88, 135]. This driving field induces joint Rabi oscillations between the states $|e,1\rangle$ and $|g,0\rangle$. Thus the joint system can be prepared in

$$|\psi\rangle = \sin\theta|e,1\rangle + \cos\theta|g,0\rangle. \tag{5.2}$$

Operating in the regime where θ is small [43], and assuming the standard single cavity circuit QED regime, where the qubit has a much longer lifetime than the cavity such that $\kappa_c \gg 1/T_1$, $|e,1\rangle$ will decay to the state $|e,0\rangle$ at a rate $\kappa_c \gg 1/T_1$. Thus, if a photon counter detects the emitted photon—after having traveled through the electro-optic transducer—this heralds the state $|e\rangle$ in the qubit. If this is completed simultaneously with two identical remotely located systems, and the photons are injected into a 50-50 beamsplitter before detection, then this is a basic protocol [43] for generating heralded Bell states

$$|\psi_{\text{Bell}}\rangle = \frac{1}{2}(|\mathrm{e,g}\rangle + |\mathrm{g,e}\rangle), \tag{5.3}$$

where the fidelity of the bell state can be exchanged for the success rate, and the protocol is insensitive (in terms of fidelity) to photon loss. However, if the act of transducing the photons destroys the state of the qubit, then entanglement cannot be heralded between the two remote qubits.

5.3 Isolation and filtering to reduce backaction

The cryogenic portion of the experiment consists of two interconnected modular systems, the first being the electro-optic transducer, in which microwave light can be coupled through an SMA port, and optical light can be coupled in through free space. The other device is a circuit QED system, where the microwave cavity is dispersively coupled to the qubit, and energy from the microwave cavity leaks out a port strongly coupled to a transmission line directed towards the electro-optic transducer. These two modular systems are connected via a superconducting coaxial transmission line through a single-junction circulator connected in series with a triple-junction circulator (see Figure 5.1). This provides a total of 63 dB of isolation to shield the circuit QED system from the strong microwave pump (up to $P_{\text{inc}} = -45$ dBm incident on the LC circuit), which is routed to the transducer through a directional coupler. The 63 dB of isolation is significantly less than the nominally specified value of 77 dB, and is likely due to unintended standing wave resonances between the circulators that reduce total amount of nonreciprocity.

The circulators are quite important for proper operation of the experiment. First, the isolation of the strong microwave pumps is critical to prevent dephasing of the qubit by the electro-optic transducer. Secondly, the circulators are needed for signal routing, so that signals reflected off of the electro-optic transducer can be routed towards a microwave amplifier for detection.

However, the circulators alone do not provide sufficient isolation between the circuit QED system and the transducer, and thus interferometric techniques must be used to reduce the amplitude of the microwave pump before it reaches the circulators. To achieve this additional isolation I send a cancellation tone through the second port of the directional coupler (labeled "cancel" in Figure 5.1(a)) to interferometrically cancel [136] the reflected microwave pump. By sending a signal of equal amplitude, but opposite phase to that of the reflected microwave pump, the signals will coherently cancel each other to null the field propagating towards the circuit QED system. The total amount of cancellation is determined by the degree to which the arms of the interferometer can be balanced.

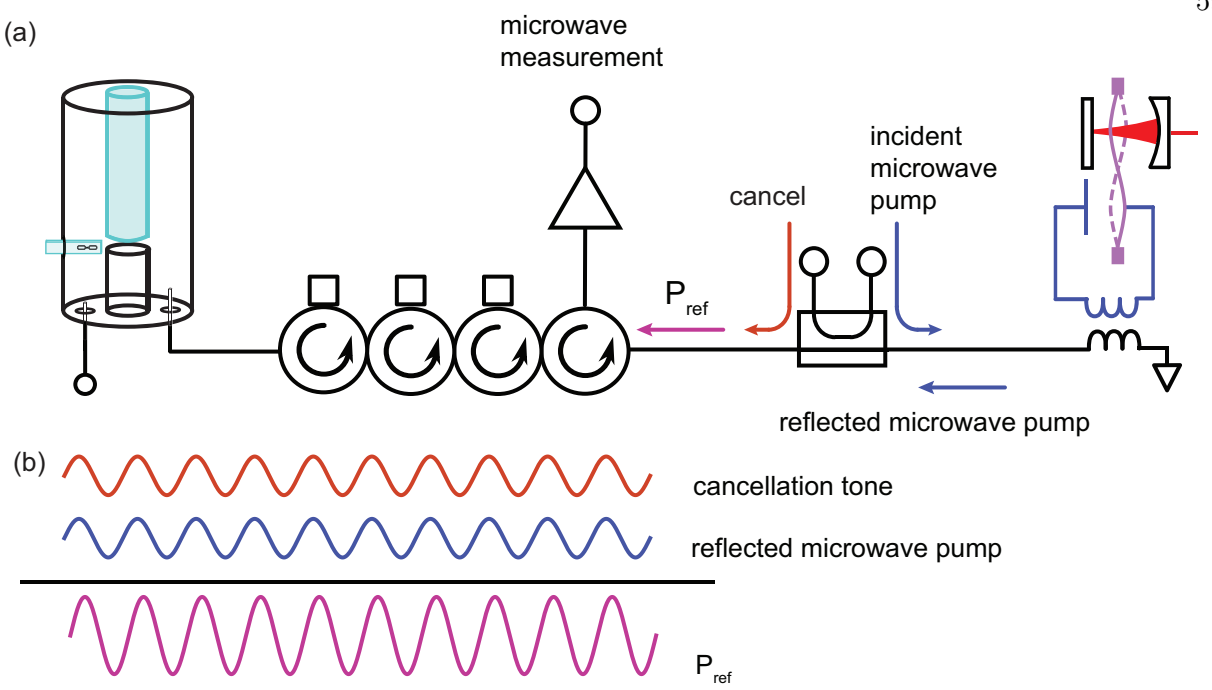

Figure 5.1: **Isolation and pump cancellation scheme.** (a) Circulators (total isolation of 63 dB) and interferometric cancellation are used to prevent the strong microwave pump from reaching the circuit QED system and dephasing the qubit. Cancellation is achieved by sending a microwave cancellation tone with amplitude equal to that of the reflected microwave pump but opposite phase into the second arm of the directional coupler. The phasor sum of this cancellation tone and the reflected microwave pump determines the pump power P_{ref} propagating towards the circuit QED system. (b) The directional coupler acts as an interferometer, enabling interference between the reflected microwave pump and the cancellation tone. During normal operation of the transducer the cancellation tone is tuned to minimize P_{ref}, but to estimate the effect of pump photons on the qubit the cancellation tone can be tuned to only partially interfere and tune P_{ref} over several decades. The phasor sum shown here is for the case of constructive interference.

5.3.1 Reducing backaction through modularity

A major advantage of the modular design used in this work is the ability to nearly completely isolate the qubit from the electro-optic transducer, while still being able to send signals from the circuit QED system through the electro-optic transducer with relatively high efficiency. Though

the modularity and isolation comes at a small cost to signal transfer efficiency between the circuit QED system and the electro-optic transducer, where $\eta_{\mathrm{mic}} = 0.34$ (see Section 4.8.4) is a significant source of loss, this still compares relatively favorably to [62]—the only other example where signals from a circuit QED system have been detected optically—where the equivalent efficiency for sending signals from a qubit to the transducer was 0.75. However, a major difference, is that in our modular system the qubit is nearly unaffected (the degree to which there is backaction will be discussed in Sections 5.4.1 and 5.4.2) by the operation of the transducer. In contrast, in [62], the act of turning on the transducer heats the qubit and completely destroys any stored information, making further error correction and heralding operations challenging.

5.4 Sources of excess backaction

I now discuss the possibility for different sources of backaction from the electro-optic transducer to influence the circuit QED system. This can come from three separate sources: the optical pumps heating the circuit QED system, coherent backaction from the microwave pump or heating induced by the microwave pump.

5.4.1 Coherent backaction from the electro-optic transducer

Due to the power of the microwave pumps used to drive the electro-optic transducer ($P_{\mathrm{inc}} = -45$ dBm), there is a distinct possibility of coherent pump photons traveling through the isolation (described in Section 5.3), entering the circuit QED system's microwave cavity, and dephashing the qubit. In this case coherent photons will dephase the qubit via the coherent AC stark effect, and induce a frequency shift of the form [118]:

$$\Delta\omega = 2\chi\bar{n}_{\mathrm{p}}\left(1 - \frac{\chi}{\kappa_{\mathrm{c}}^2/4 + \chi^2 + \Delta^2}\right) \approx 2\chi\bar{n}_{\mathrm{p}}, \tag{5.4}$$

where the fractional term can be neglected as the pump is detuned by $|\Delta| = \omega_{\mathrm{m}} = 2\pi \times 1.45$ MHz, such that $|\Delta| \gg \kappa_{\mathrm{c}}, \chi$. The pump photons in the circuit QED cavity are given by $\bar{n}_{\mathrm{p}} = (\bar{n}_+ + \bar{n}_-)/2$,

where

$$n_{\pm} = \frac{\kappa_{\mathrm{c,ext}}|\alpha_{\mathrm{in}}|^2}{\kappa_c^2/4 + (\Delta \pm \chi)^2}. \tag{5.5}$$

Note that $\bar{n}_+ \approx \bar{n}_-$ insofar as $\chi/|\Delta| \ll 1$. See Table 5.1 for the relevant circuit QED system parameters. In order to separate out thermal backaction (which will also shift the qubit's frequency) from coherent backaction, I tune the electromechanical pump to a power such that $P_{\mathrm{inc}} = -77.5$ dBm and heating of the dilution refrigerator's base plate by the pump is negligible. Then, without changing the incident power (which could possibly change the thermal backaction) I tune the interferometric cancellation to tune the reflected microwave pump power P_{ref} over several decades (see Figure 5.1(a),(b)). Thus, under these operating conditions, any frequency shift of the qubit is entirely due to coherent backaction from the microwave pump.

Figure 5.2 shows the expected linear dependence of coherent photon number $\bar{n}_{\mathrm{p}}$ (as measured via a Ramsey experiment) on P_{ref}. Note that during normal operation of the transducer I tune the cancellation so that $P_{\mathrm{ref}} < -95$ dBm. There is no data at these low values of P_{ref}, since resolving such small frequency shifts is not easily achieved, but I can extrapolate the linear fit to -105 dBm $\leq P_{\mathrm{ref}} \leq -95$ dBm to infer $\bar{n}_{\mathrm{p}}$ at the typical operating point of the interferometer. From this data, it is clear that $n_{\mathrm{p}} < 1 \times 10^{-3}$, indicating minimal coherent backaction from the microwave pump during normal operation of the electro-optic transducer.

5.4.2 Thermal backaction

The main source of backaction present in more standard circuit QED experiments is backaction from thermally generated photons [120]. In the experiments shown here, since the base temperature of the dilution refrigerator is raised by both the microwave and optical pumps used to mediate transduction, it is certainly possible that the operation of the electro-optic transducer imparts thermal backaction on the qubit. These thermal photons cause dephasing of the qubit of the form [137, 138]

$$\Gamma_\phi = \frac{\kappa_{\mathrm{c}}}{2}\mathrm{Re}\left[\sqrt{\left(1 + \frac{2i\chi}{\kappa_{\mathrm{c}}}\right)^2 + \frac{8i\chi n_{\mathrm{eff}}}{\kappa_{\mathrm{c}}}} - 1\right]. \tag{5.6}$$

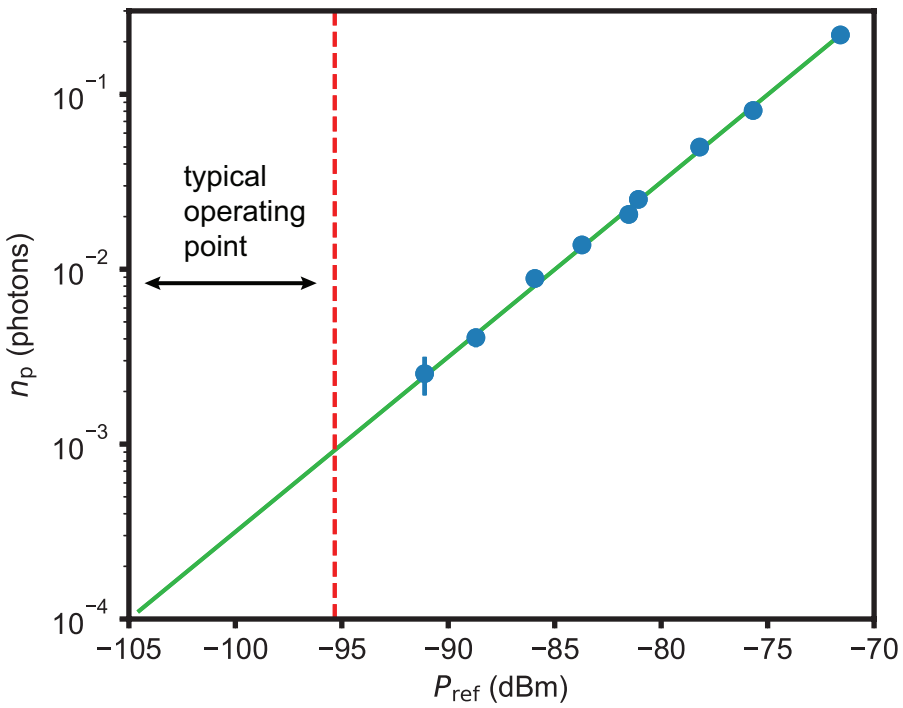

Figure 5.2: **Excess backaction from pump photon leakage.** The number of pump photons in the circuit QED system $\bar{n}_p$ is measured as P_{ref} is varied. During transducer operation the cancellation is typically tuned to achieve -105 dBm $< P_{ref} < -95$ dBm or equivalently $\bar{n}_p < 1 \times 10^{-3}$. The cancellation does not stay completely fixed over the course of the experiment due to small thermal drifts slightly changing the amplitude of P_{ref}.

Where $n_{eff} = \bar{n}_{th} + \Delta n$ is the effective occupancy of the circuit QED system's microwave cavity mode. This effective occupancy is the sum of two different contributions: the thermal occupancy of the resonator due to its environment n_{th}, and excess backaction from the converter Δn. In the limit where $n_{eff} \ll 1$ Equation 5.6 can be Taylor expanded such that:

$$\frac{1}{T_\phi} = \Gamma_\phi = \frac{\kappa_c \chi^2}{\frac{\kappa_c^2}{4} + \chi^2} n_{eff}. \tag{5.7}$$

To measure the effects of thermal dephasing, I first measure the effect of the optical pump on the circuit QED system, with the microwave pump off. In Figure 5.3 a microwave-domain Ramsey experiment is performed to measure the coherence time of the qubit when the laser is off (red circles) and when it is on with $\Gamma_o/2\pi = 5.0$ kHz (cyan diamonds), achieved with 11 mW of circulating power in the optical cavity. I find $T_{2,on} = 20.7 \pm 0.2$ µs and $T_{2,off} = 20.4 \pm 0.2$ µs, showing no measurable change in the qubit coherence time due to laser illumination. This is the hoped for

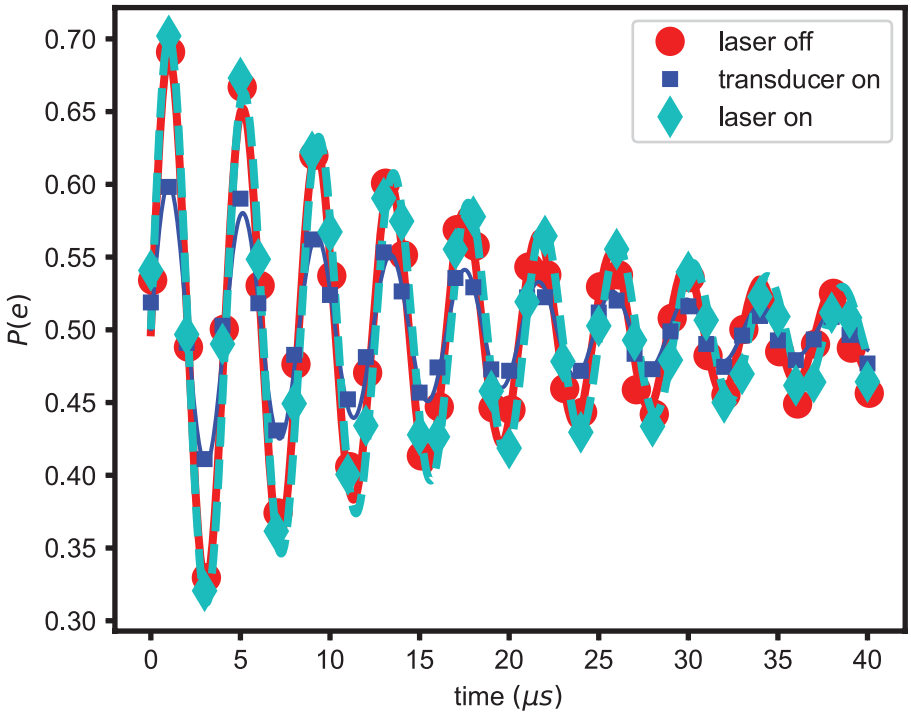

Figure 5.3: **Qubit coherence when operating the electro-optic transducer.** Ramsey fringes under different operating conditions of the electro-optic transducer. Red circles are with the transducer completely off. Cyan diamonds are with the laser on ($\Gamma_o = 2\pi \times 5.0$ kHz). The blue squares are with the transducer on with $(\Gamma_e, \Gamma_o)/2\pi = (1.1, 5.0)$ kHz

result as the circuit QED system is sealed in a light tight box and spatially separated from the optical port. The blue points are taken with the transducer on, such that $\Gamma_o/2\pi = 5.0$ kHz and $\Gamma_e/2\pi = 1.1$ kHz. In this case, the coherence time is slightly reduced to $T_{2,\mathrm{tr}} = 19 \pm 1$ µs. The single-shot readout contrast is reduced significantly due to *microwave* pump power-dependent loss and noise in the LC circuit (see Section 4.8.4), but this is not an effect of the pump on the qubit.

The scope of this measurement can be expanded by additionally measuring the lifetime of the qubit to determine its dephasing rate $\Gamma_\phi = T_\phi^{-1} = T_2^{-1} - \frac{1}{2}T_1^{-1}$, and infer the effective occupancy n_{eff} of the circuit QED system's microwave cavity using Equation (5.7). In Figure 5.4 I show the results of sweeping the dilution refrigerator's base temperature, where the T_1, T_2 and T_ϕ time of the qubit are shown under various different operating conditions of the transducer. There is a strong dependence of the T_2 time and T_ϕ time on the base temperature of the dilution

refrigerator as expected. I can then convert the decay time measurements to effective occupancy

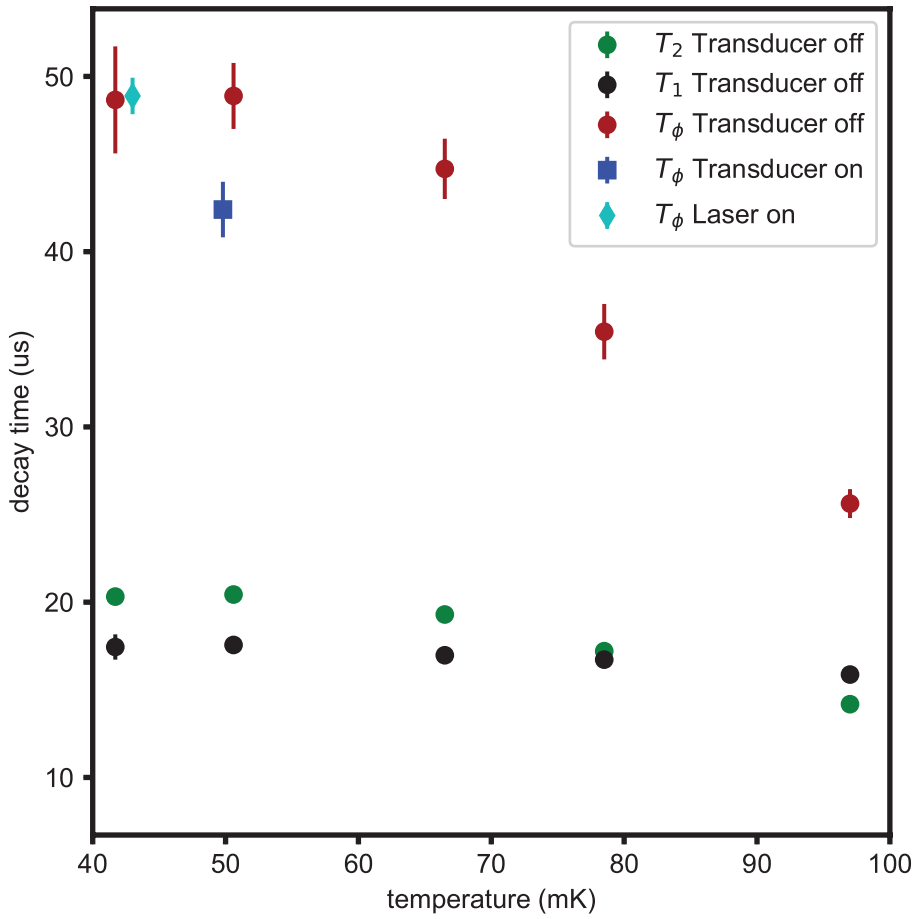

Figure 5.4: **Qubit decay times versus temperature.** Qubit Lifetime (T_1, black circles), qubit Ramsey time (T_2, green circles), dephasing time with the laser and microwave pumps off (T_ϕ, red circles), dephasing time with the laser on ($\Gamma_o = 2\pi \times 5.0$ kHz, cyan diamond) and dephasing time with the Transducer on ($\Gamma_e = 2\pi \times 1.1$ kHz, $\Gamma_e = 2\pi \times 5.0$ kHz).

of the circuit QED system's microwave resonator through Equations 5.1 and 5.7. In Figure 5.5 I plot the effective occupancy n_{eff} as the temperature of the dilution refrigerator's base plate T_{bp} is varied. At low temperature, the inferred thermal occupancy plateaus at $n_{\text{th}} \approx 0.019$ photons ($T_{\text{eff}} = 95$ mK), though this plateau may be caused by intrinsic sources of qubit dephasing other than an elevated temperature [20]. The cyan diamond in Figure 5.5 demonstrates that there is no measurable excess backaction from the laser ($\Gamma_o/2\pi = 5.0$ kHz) on the qubit. I then turn on the microwave pump ($\Gamma_e/2\pi = 1.1$ kHz, leaving Γ_o unchanged) and the blue square in Figure 5.5

indicates excess backaction of $\Delta n = (3 \pm 1) \times 10^{-3}$ photons. This excess backaction must come largely from local heating of microwave components by the strong microwave pump with incident power $P_{\mathrm{inc}} = -45$ dBm, since in Section 5.4.1 it was established that backaction from coherent pump photons is negligible. It is worth emphasizing that these backaction measurements are taken at the largest possible values of Γ_{o} and Γ_{e} used in this work, and backaction will likely be even lower when operating at smaller Γ_{e}.

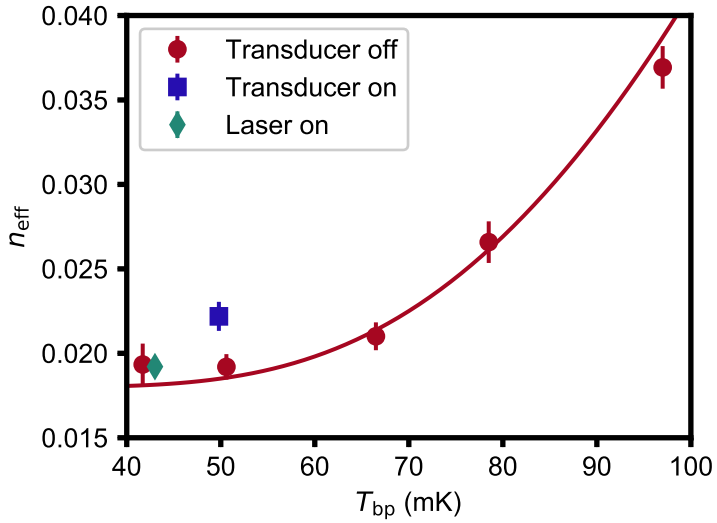

Figure 5.5: **Transducer backaction.** Effective thermal occupancy of the circuit QED system's microwave cavity as a function of the dilution refrigerator base plate temperature T_{bp}. Red circles are data obtained with the transducer off, while the red line is theory. The cyan diamond indicates the occupancy of the microwave cavity with $\Gamma_{\mathrm{o}}/2\pi = 5.0$ kHz, indicating no additional dephasing of the qubit from the optical field. The blue square is the effective occupancy while operating the transducer at $(\Gamma_{\mathrm{e}}, \Gamma_{\mathrm{o}})/2\pi = (1.1, 5.0)$ kHz. There is a small amount of excess backaction equivalent to $\Delta n = (3 \pm 1) \times 10^{-3}$ photons in the microwave cavity. All error bars represent one standard deviation.

5.5 Future improvements and considerations

5.5.1 Filtering and interferometric cancellation

Filters are placed between the circuit QED system and the transducer (see Figure A.3) to eliminate the propagation of high-frequency thermal radiation along the coaxial cable connecting

the two systems. These filters consist of a custom built eccosorb filter, which becomes lossy at frequencies above 10 GHz, and a low pass filter from K & L with a cutoff frequency at 10 GHz. See Figure A.3 for details on the location and type of filtering. It may be prudent to remove these filters from the signal path in future experiments as they are likely responsible for a large portion of the microwave loss ($\eta_{\mathrm{mic}} = 0.34$), which is discussed in 4.8.4. The filters could instead be placed on all of the input lines. Assuming that the dominant source of noise is coming from the pump and control lines, they would function equally well in such a configuration, and η_{mic} would likely improve. However, if the electro-optic transducer is a source of high frequency radiation itself, which is a possibility due to heating from microwave and optical pumps, then the coherence time of the superconducting qubit may be reduced in this configuration.

Interferometric cancellation (see Figure 5.1) turned out to be critical for the operation of the experiment, and yet it also could be improved further. Currently it is tuned by hand by adjusting the phase and amplitude of the cancellation signal until the pump signal measured via the microwave measurement chain is minimized. This enables upwards of a 40 dB reduction in P_{ref}, but tends to slowly drift over time as the helium level in the cryostat varies. Furthermore, each time the electromechanical damping is changed, this changes the settings required for cancellation, requiring the cancellation to be adjusted, which depending on the set of measurements being completed, can be quite tedious and inefficient. Thus a software controlled cancellation scheme might be quite important in future iterations of this experiment. Not only would it allow for higher levels of cancellation and isolation between the transducer and the circuit QED system through the use of active feedback, but it would also streamline certain experiments where Γ_{e} must be varied.

5.5.2 Excess backaction

The excess backaction of $\Delta n = (3 \pm 1) \times 10^{-3}$ from the transducer is already very low, but further improvements to the experimental apparatus can improve upon these results. Improvements in g_{e} should directly lower Δn since $\Gamma_{\mathrm{e}} \propto g_{\mathrm{e}}^2 P_{\mathrm{inc}}$, meaning that lower P_{inc} will be required to achieve the same value of Γ_{e}. This may be relatively important since the circuit QED system used in this

work had quite a narrow linewidth, with $\kappa_c = 2\pi \times 380$ kHz, which also provided significant isolation from the pump detuned by 1.45 MHz. If in the future, more modern circuit QED technology is used, where multiple cavities are coupled to the qubit, the resonator that is coupled to the transmission line may have a linewidth closer to 2 MHz. If such a system were used, then the backaction from coherent pump photons would be enhanced by roughly a factor of 60. Thus, the isolation provided by the resonant cavity of the circuit QED system must be considered when designing devices for integration with the electro-optic transducer.

5.5.3 Residual thermal occupancy

If one calculates the thermal occupancy of a 7.938 GHz microwave resonator (the cavity frequency used in this work) at 40 mK, then one finds that $\bar{n}_{\text{th}} \approx 8 \times 10^{-5}$ photons. However, under real experimental conditions it is difficult to thermalize microwave components to the base temperature of the dilution refrigerator, and thermal occupancies well above this level in the range of $10^{-3} < n_{\text{th}} < 10^{-1}$ are frequently seen [127, 92, 139]. Indeed in this experiment, the thermal occupancy of the microwave cavity plateaus at an effective occupancy of $n_{\text{eff}} = 0.019$ photons, more than two orders of magnitude higher than the expected value. This is particularly concerning, because with the same qubit and circuit QED system cooled down in a dilution refrigerator without optical access, the T_2 time of the qubit was significantly higher at $T_2 = 34$ µs, while $T_1 = 21$ µs, which yields a dephasing time of 179 µs—significantly larger than what is seen in the optical access dilution refrigerator (see Figure 5.4). This yields an effective occupancy of $n_{\text{eff}} = 5 \times 10^{-3}$, which is significantly lower.

The reason for this disparity in performance between the optical access dilution refrigerator and a more 'normal' dilution refrigerator likely has nothing to do with the optical access port. Instead, the rather large level of pump power required for the microwave pumps necessitates less attenuation than normal on the microwave pump and cancellation lines. In this work that attenuation was measured to be 51 dB. Whereas in a normal qubit experiment, one would ideally place $70 - 80$ dB of total attenuation [116, 120] (typically divided between the 4 K, still and < 50 mK

stages) between 300 K and the base temperature of the dilution refrigerator. Currently, the attenuation at the base temperature of the dilution refrigerator is supplied by a 20 dB directional coupler. Switching this out to a 30 dB or 40 dB directional coupler may have significant benefits for the coherence time of the qubit in the optical access dilution refrigerator, though this will have to be carefully balanced with the capabilities of the microwave generator at ambient temperature, where ~ 27 dBm of power is already being sourced to achieve the highest incident microwave power of $P_{\mathrm{inc}} = -45$ dBm.

Table 5.1: Circuit QED system parameters important for backaction estimation

Parameter	**Symbol**	**Value**
Qubit frequency	ω_{q}	$\omega_{\mathrm{q}}/2\pi = 5.632$ GHz
Qubit-cavity coupling	g_{qc}	$g_{\mathrm{qc}}/2\pi = 66.4$ MHz
Qubit anharmonicity	ν	$\nu/2\pi = 228$ MHz
Dispersive shift	χ	$\chi/2\pi = 172$ kHz
Cavity frequency	ω_{c}	$\omega_{\mathrm{c}}/2\pi = 7.938$ GHz
Cavity linewidth	κ_{c}	$\kappa_{\mathrm{c}}/2\pi = 380$ kHz
Weak port coupling	$\kappa_{\mathrm{c,w}}$	$\kappa_{\mathrm{c,w}}/2\pi < 5$ kHz
Cavity internal loss	$\kappa_{\mathrm{c,int}}$	$\kappa_{\mathrm{c,int}}/2\pi < 10$ kHz
Maximum microwave pump power	P_{inc}	$P_{\mathrm{inc}} = -45$ dBm

Chapter 6

Transient electromechanical amplification

6.1 Preface

This work was completed during the early stages of my doctoral work, predating my work on integrating superconducting qubits with electro-optic transducers. Although it is not directly related to quantum networking and electro-optic transduction, this work describes a technique for pulsed readout of an electromechanical element at the noise limits imposed by quantum mechanics. Pulsed protocols may be needed to mitigate noise in future iterations of the microwave to optical transduction project, or for experiments involving continuous variable entanglement between microwave and optical modes [140, 141, 142, 143]. Furthermore, an ideal transducer can be viewed as the limit of a measurement without gain [74], and thus many of the ideas in this work can be related closely to what one would like to achieve with an electro-optic transducer.

6.2 Introduction

The past ten years has seen a dramatic improvement in the ability to measure and control the quantum state of macroscopic mechanical oscillators. Much of this progress results from advances in the parametric coupling of these oscillators to optical cavities or resonant electrical circuits. These related fields of optomechanics and electromechanics have demonstrated the ability to cool mechanical oscillators to near their motional ground state [117, 144, 97, 69], entangle mechanical oscillators with each other [145, 146, 143] or with other degrees of freedom [141], and create squeezed states of motion [147, 148, 149]. To verify the successful creation of these non-classical

states, electromechanical and optomechanical methods have also enabled measurements of mechanical motion with near 50% quantum efficiency [150, 151], or equivalently an added noise equal to the zero-point motion of the oscillator, the quantum limit for simultaneous measurement of both mechanical quadratures [74].

These advances have encouraged notions of using non-classical states of motion to test quantum mechanics at larger scales, sensing forces with quantum enhanced precision, and enabling quantum transduction between disparate physical systems [56]. But as mechanical oscillators are prepared in more profoundly quantum states [152, 153], with finer features in oscillator phase-space, the measurement efficiency must further improve to resolve these fine features and to use them to realize a quantum advantage.

Reaching higher levels of efficiency with existing methods is hindered by fundamental and technical limitations, which seem difficult to overcome. In electromechanical and optomechanical devices, the state of motion can be converted without gain or added noise into a propagating electric field, and one quadrature component of the field can be measured nearly noiselessly [141, 150]. However, the loss experienced by the field traveling between the device and the amplifier has prevented quantum efficiency much greater than 50%. To improve measurement efficiency, the device can be used as its own parametric amplifier, emitting an electric field that encodes an amplified copy of the mechanical oscillator's state, thereby overcoming any subsequent loss and inefficiency of the following measurement chain. Using this strategy, both quadratures can be measured simultaneously with added noise very close to the quantum limit [151]. For steady state monitoring of a single quadrature, backaction evading schemes are in principle, noiseless [154, 155, 156, 148]. However, unwanted parametric effects, both parasitic [157, 158] and intrinsic to the electromechanical Hamiltonian [159, 160], have prevented measurements with noise far below the quantum-limited value.

In this Chapter, I demonstrate an efficient measurement of a single mechanical quadrature, monitoring mechanical motion with an added noise of -8.5 ± 2.0 dB relative to zero-point motion, and a quantum efficiency of $\eta_{\mathrm{q}} = 88 \pm 5$ %. By generating mechanical dynamics equivalent to the

time-reverse of dissipative squeezing [161], I intentionally induce mechanical instability through the electromechanical interaction, allowing for a pulsed measurement of the initial state of the mechanical oscillator. I term this protocol transient electromechanical amplification (TEA), and demonstrate the resolution of fine features in phase space by using TEA to perform quantum state tomography [162] on a dissipatively squeezed state of the mechanical oscillator, from which the density matrix of the mechanical oscillator can be reconstructed.

6.3 Electromechanical device

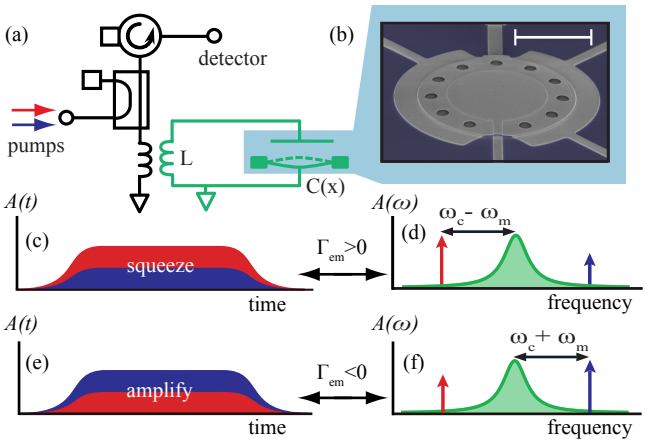

Figure 6.1: **Transient electromechanical amplification schematic.** (a) Schematic of experiment consisting of the electromechanical circuit (green) inductively coupled to a transmission line. Pump tones are applied through a directional coupler, while outgoing microwave signals are directed to a chain of conventional microwave amplifiers and mixer circuits, forming a microwave receiver, which adds noise much larger than zero-point fluctuations. (b) False-color micrograph of aluminum drum. The white bar corresponds to a distance of approximately 10 µm. (c) Time and (d) frequency domain representation of temporally overlapping dissipative squeezing pump tone amplitudes ($A(t)$ and $A(\omega)$). (e) Time and (f) frequency domain representation of transient electromechanical amplification (TEA) pump tone amplitudes.

The device (shown schematically in Figure 6.1a is an aluminum inductor-capacitor (LC) circuit composed of a spiral inductor and a compliant vacuum gap capacitor, which couples electrical energy to motion. The LC circuit has a resonant frequency of $\omega_c \approx 2\pi \times 7.4$ GHz, and is coupled to a transmission line at a rate $\kappa_{\text{ext}} \approx 2\pi \times 3.1$ MHz. The compliant top-plate of the capacitor (shown in Figure 6.1(b)) is free to vibrate with a fundamental mechanical resonant frequency of

$\omega_m \approx 2\pi \times 9.4$ MHz and mechanical linewidth of $\gamma_m \approx 2\pi \times 21$ Hz. The electromechanical system is attached to the base plate of a dilution refrigerator, resulting in a mechanical occupancy of $n_m \leq 40$ in thermal equilibrium.

6.4 Pulsed measurement and squeezing of motion

The electromechanical circuit is in the resolved sideband regime [79], enabling coherent control of motion with microwave tones. Applying a red detuned microwave pump to the LC circuit ($\Delta \equiv \omega_c - \omega_p = -\omega_m$) allows for sideband cooling [117], and state transfer between mechanical and microwave fields [163, 164], where ω_p is the frequency of the pump tone. A blue detuned microwave pump ($\Delta = +\omega_m$) creates entanglement between mechanical and microwave fields [141], and realizes a quantum limited phase-insensitive amplifier of mechanical motion [151]. Combining these two interactions, with simultaneous application of red and blue detuned pump tones, addresses two orthogonal mechanical quadratures $\hat{X}_+ = \frac{i}{\sqrt{2}}(\hat{c}^\dagger - \hat{c})$ and $\hat{X}_- = \frac{1}{\sqrt{2}}(\hat{c}^\dagger + \hat{c})$ independently, and enables backaction evading measurement, dissipative squeezing and TEA.

The type of interaction is determined by the sign of $\Gamma_{em}(t) = \Gamma_-(t) - \Gamma_+(t)$, where $\Gamma_\pm(t)$ are the electromechanical growth and decay rates caused by the blue (+) and red (-) detuned microwave tones respectively [141]. Dissipative squeezing occurs when $\Gamma_{em}(t) > 0$, which cools the mechanical oscillator towards a squeeezed vacuum state [161]. The microwave control tones that enable dissipative squeezing are shown schematically in the time and frequency domain in Figures 6.1(c) and 6.1(d). Ideal backaction evasion occurs when $\Gamma_{em} = 0$, where perfect constructive interference between sidebands decouples one mechanical quadrature from microwave vacuum fluctuations, producing an amplified noiseless representation of a single mechanical quadrature in a single microwave quadrature [155]. Finally, TEA occurs when $\Gamma_{em}(t) < 0$, amplifying motion with energy gain $G \approx e^{|\Gamma_{em}|t}$. Figures 6.1(e) and 6.1(f) show the microwave pump tones used in the time and frequency domain for TEA.

For both TEA and backaction evading measurement, the motion of a single mechanical quadrature $\hat{X}$ is encoded in a single microwave quadrature $\hat{U}$. The variance of $\hat{U}$ can then be

written as the sum of the noise contributions from the signal and added noise:

$$\langle \Delta \hat{U}^2 \rangle = G_{\mathrm{tot}} \left(\langle \Delta \hat{X}^2 \rangle + \langle \Delta \hat{X}^2_{\mathrm{add}} \rangle \right), \tag{6.1}$$

where G_{tot} is the total gain of the microwave receiver chain in units of V^2/quanta. If the total added measurement noise $\langle \Delta \hat{X}^2_{\mathrm{add}} \rangle$ is known, then the variance of the mechanical state $\langle \Delta X^2 \rangle$ can be inferred. Equivalently, by preparing a mechanical state with known variance the added measurement noise can be characterized. For an ideal single quadrature measurement $\langle \Delta \hat{X}^2_{\mathrm{add}} \rangle = 0$ and U faithfully records one quadrature of of the mechanical state. Approaching this ideal behavior is highly desirable for characterizing quantum states of motion, as the number of repeated measurements required to reconstruct a quantum state grows rapidly with added noise. Furthermore, assigning meaningful uncertainties to the extracted density matrix after any inference or deconvolution procedure is complicated and subtle, diminishing confidence in the inferred state.

For the two special quadratures $\hat{X}_{\pm}$, the noise properties of TEA are determined by the relative strength of Γ_+ and Γ_-. Assuming optimal detuning of the microwave tones by exactly $\pm\omega_{\mathrm{m}}$ and $\Gamma_{\pm} \ll \kappa/2$ (avoiding the strong coupling regime), the added noise $\langle \Delta \hat{X}^2_{\mathrm{add},\pm} \rangle$ referred to the input of TEA is given by

$$\langle \Delta \hat{X}^2_{\mathrm{add},\pm} \rangle \approx \frac{(\sqrt{\Gamma_+} \pm \sqrt{\Gamma_-})^2 + \gamma_{\mathrm{m}}(2n_{\mathrm{m}} + 1)}{2|\Gamma_{\mathrm{em}} + \gamma_{\mathrm{m}}|}. \tag{6.2}$$

In analogy with the high cooperativity limit, if $\gamma_{\mathrm{m}}(2n_{\mathrm{m}} + 1)/|\Gamma_{\mathrm{em}} + \gamma_{\mathrm{m}}| \ll 1$, then $\langle \Delta \hat{X}^2_{\mathrm{add},-} \rangle$ will be less than the zero-point motion. In the case where $\Gamma_- = 0$, equal noise will be added to both quadratures, enabling nearly quantum limited phase-insensitive amplification [151]. However, if the pump frequencies deviate from optimal detuning, either through an initial detuning, or through pump-power induced shifts in the circuit's resonance frequency, Equation 6.2 is not valid, and theory including pump induced mechanical and cavity frequency shifts is required (Appendix C.2). Similarly, the variance of the squeezed and anti-squeezed quadratures after dissipative squeezing $\langle \Delta \hat{X}^2_{\mathrm{sq},\pm} \rangle$ takes the same form as Equation 6.2, but with $\Gamma_- > \Gamma_+$. In Figure 6.2(a) I demonstrate, in a three step protocol, the control of the mechanical oscillator needed to study TEA. An initial pair

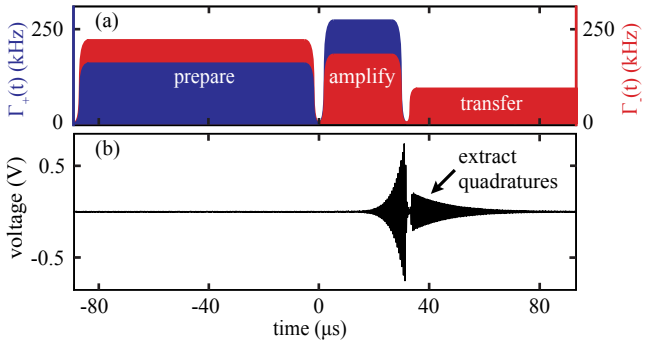

Figure 6.2: **Transient electromechanical amplification pulse sequence.** (a) General pulse protocol for characterization of TEA and squeezing. The first overlapping red/blue-detuned pulses determine whether the mechanical oscillator is squeezed, cooled or allowed to thermalize with its environment. The second set of pulses tune the gain and added noise of the measurement. The final red-detuned pulse transfers the amplified state of the mechanical oscillator to the microwave field for quadrature extraction. The pulse lengths are chosen so that $e^{|\Gamma_{\rm em}|t}$ is large, and provides sufficient amplification gain or dissipative squeezing and cooling to overwhelm the thermal noise of the mechanical environment. The pulse envelopes drawn are slower than in the experiment for visual clarity. (b) A single experimental voltage trace of the down-converted microwave field ($\omega_{\rm het} = 2\pi \times 1.8$ MHz) showing the resulting exponential growth and decay of the microwave field due to the amplification and transfer pulses respectively.

of pulses prepares the mechanical oscillator in a desired state, by either sideband cooling ($\Gamma_- > 0$ and $\Gamma_+ = 0$), dissipatively squeezing ($\Gamma_- > \Gamma_+ > 0$) or letting the mechanical oscillator reach equilibrium with its thermal environment ($\Gamma_+ = \Gamma_- = 0$). Following state preparation, the motion of the mechanical oscillator and the amplitude of the microwave field, are amplified by applying red and blue pumps such that $\Gamma_+ > \Gamma_-$. After a short delay, the red-detuned pump is pulsed on to transfer the previously amplified state of the mechanical oscillator to the microwave field [164]. After further amplification by a high-electron-mobility transistor (HEMT) amplifier, and a room temperature measurement chain, the signal is mixed down to $\omega_{\rm het} = 2\pi \times 1.8$ MHz, allowing the two mechanical quadratures to be extracted from the exponentially decaying microwave field shown in Figure 6.2(b).

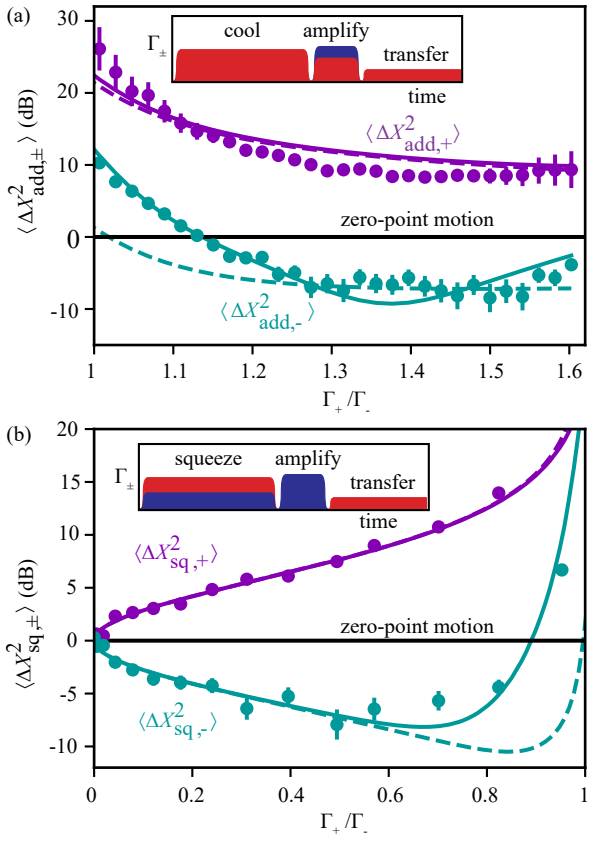

Figure 6.3: **Transient electromechanical amplification: added noise and squeezing.** (a) Total added noise referred to the input of TEA relative to zero-point motion. Γ_+ is varied, while $\Gamma_- = 2\pi \times 181$ kHz is held constant. The circles are data, while theory from Equation 6.2 (including HEMT noise contributions) is shown without any free parameters as the dashed lines, and deviates significantly because the pump power is large enough to induce additional parametric processes. The solid lines are theory including parametric effects (with free parameters). The inset illustrates the pulse sequence used for the inference of $\langle \Delta \hat{X}^2_{\mathrm{add},\pm} \rangle$. Here, I obtain a minimum added noise of $\langle \Delta \hat{X}^2_{\mathrm{add},-} \rangle = -8.5 \pm 2.0$ dB. (b) Inferred variance of the squeezed $\langle \Delta X^2_{\mathrm{sq},-} \rangle$ and anti-squeezed $\langle \Delta X^2_{\mathrm{sq},+} \rangle$ quadratures after dissipatively squeezing. Γ_+ is varied, while $\Gamma_- = 2\pi \times 154$ kHz is held constant. The minimum squeezed variance is $\langle \Delta X^2_{\mathrm{sq},-} \rangle = -7.9 \pm 1.4$ dB. The circles are the data, while theory is shown without any free parameters as the dashed lines, with the expected agreement at low pump powers. The solid lines are theory including parametric effects (with free parameters). The inset illustrates the pulse sequence for the inference of squeezing.

6.5 Added noise

I can determine experimentally the total noise $\langle \Delta \hat{X}^2_{\mathrm{add},\pm} \rangle$ added during TEA by separately preparing the mechanical oscillator in both a thermal state and through sideband cooling. By comparing the variance of these two states in a ratio, the added noise can be inferred (see Ap-

pendix C.4). Figure 6.3(a) shows the total added noise as a function of the ratio of red and blue pump power. With the optimal ratio of the red and blue-detuned pumps I find total added noise relative to zero-point motion of $\langle \Delta \hat{X}^2_{\mathrm{add},-} \rangle = -8.5 \pm 2.0$ dB. I compare these results to the prediction of Equation 6.2 with no adjustable parameters, illustrating poor quantitative agreement. I attribute this discrepancy to additional squeezing of the mechanical oscillator caused by non-linear mixing of the microwave pumps. I find good agreement in a fit to a more general theory that includes such processes (and see Appendix C.2). The two theories deviate significantly from each other, but TEA nevertheless achieves a minimum added noise equivalent to that predicted by the ideal case in Equation 6.2. I emphasize that $\langle \Delta X^2_{\mathrm{add},\pm} \rangle$ is the total noise added by the entire measurement chain, and for $\Gamma_+/\Gamma_- > 1.3$ TEA has large enough gain to overwhelm the noise added by the HEMT amplifier (see Appendix C.4.6).

Avoiding the noise associated with the simultaneous measurement of non-commuting observables is of particular importance when measuring mechanical states with a width in phase space less than the zero-point motion of the oscillator [165], and is desirable for many quantum state tomography protocols [166]. Thus, to test the effectiveness of TEA on states with variance below zero-point fluctuations, I prepare squeezed states of motion using the dissipative procedure illustrated in the inset of Figure 6.3(b). To infer the total amount of squeezing, the motion is first squeezed for 90 μs, then a 30 μs blue-detuned microwave pulse ($\Gamma_+ = 2\pi \times 73$ kHz and $\Gamma_- = 0$) is applied to amplify both motional quadratures. The variance associated with zero-point motion, which must be added by the phase-insensitive amplifier, is subtracted to infer the variance of the squeezed and anti-squeezed quadratures, which is shown in Figure 6.3(b). I obtain a maximum inferred vacuum squeezing of $\langle \Delta \hat{X}^2_{\mathrm{sq},-} \rangle = 7.9 \pm 1.4$ dB below the zero-point motion of the mechanical oscillator. I am able to far surpass the so-called steady state 3 dB squeezing limit both because of the use of pulsed operations, and more than a single mode is involved during dissipative squeezing [167]. Theory without any free parameters is plotted as the dashed lines in Figure 6.3(b), which agrees well at low pump powers. The solid lines show predicted squeezing when including additional parametric effects induced by nonlinear mixing of the two microwave pumps (with free

parameters).

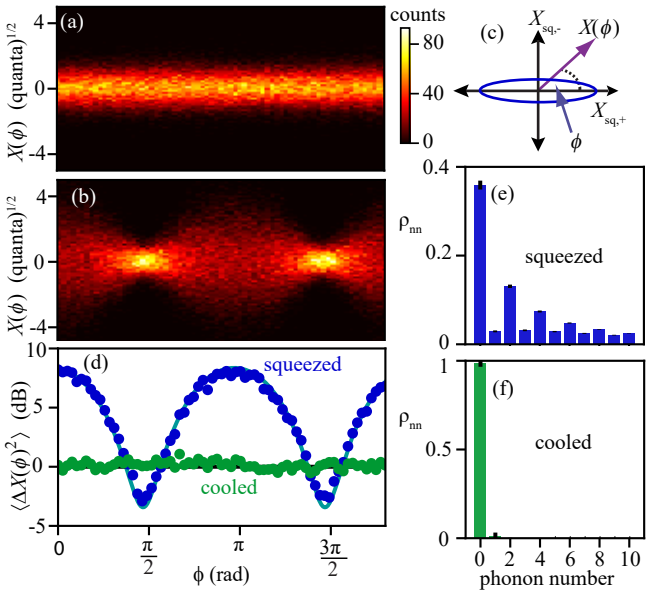

Figure 6.4: **Quantum state tomography of motion.** Measurement of mechanical squeezed and sideband cooled states with single quadrature TEA. (a) A density plot of the marginal distributions of a sideband cooled state as a function of tomography angle ϕ. (b) A density plot of the marginal distributions of a squeezed state using single quadrature TEA as a function of ϕ. (c) The schematic shows the rotation of the single quadrature measurement axis $X(\phi)$ relative to the prepared squeezed state. The squeezed variance is represented as the blue ellipse. (d) The total measured variance of a sideband cooled state with $n_{\mathrm{sb}} \approx 0.02$ (green) and squeezed vacuum (blue), which exhibits squeezing 2.8 ± 0.3 dB below zero-point motion. The data points are the circles, while theory (with no free parameters) is the solid line. (e) Squeezed and (f) sideband cooled diagonal density matrix elements are inferred from tomographic reconstruction of the covariance matrix. The error bars represent 90% confidence intervals estimated with an empirical bootstrap of the tomography data.

6.6 Quantum state tomography of motion

Having demonstrated that I can prepare a squeezed state with variance below zero-point motion, the ability of TEA to resolve fine phase space features can be tested by performing quantum state tomography on the squeezed mechanical state. By rotating a noiseless single quadrature measurement through all possible measurement axes, a set of phase space marginals can be recorded, and the density matrix can be reconstructed via quantum state tomography [168, 169, 170, 136, 171]. Figures 6.4(a) and 6.4(b) show histograms of a sideband cooled and a dissipatively squeezed state

of the mechanical oscillator as a function of the tomography angle ϕ. Figure 6.4(c) demonstrates the rotation of the single quadrature measurement axis relative to the prepared squeezed state by ϕ.

The minimum width that can be resolved in the tomography data $\langle \Delta \hat{X}_{\mathrm{min}}(\phi)^2 \rangle$ is an important figure of merit for single quadrature measurements in the quantum regime. In Figure 6.4(d) the total variance as a function of tomography angle is computed with theory (using independently measured parameters) shown as the solid blue line. The squeezed quadrature has a total variance of $\langle \Delta \hat{X}_{\mathrm{min}}(\phi)^2 \rangle = \langle \Delta \hat{X}^2_{\mathrm{sq},-} \rangle + \langle \Delta \hat{X}^2_{\mathrm{add},-} \rangle = 2.8 \pm 0.3$ dB below the zero-point motion of the mechanical oscillator. I emphasize that this represents the total reduction in noise that is present at the end of the conventional microwave receiver and no noise is subtracted to find this result.

The marginal distributions (1.4×10^5 points in total) can be used to reconstruct the density matrix of the quantum state in the number basis. For a general quantum state, iterative methods of tomographic reconstruction [162]–based upon maximum likelihood–are a reliable method of estimating quantum states [166], and are guaranteed to produce a physical density matrix. However, tomographic reconstruction of squeezed states in the Fock basis requires estimating density matrix elements up to very high phonon number [172, 136]. To avoid calculating large density matrices I assume Gaussian Wigner quasiprobability distributions [70], and estimate the density matrix through reconstruction of the covariance matrix [173]. The covariance matrix is then used to infer the Fock basis density matrix of the mechanical oscillator. In Figures 6.4(e) and 6.4(f) I plot the inferred diagonal density matrix elements for the squeezed vacuum and sideband cooled states, with the error bars on the measurements representing 90 % confidence intervals from an empirical bootstrap procedure (see Appendix C.7). From the density matrix I also infer the purity of the squeezed state to be $\mu = 0.53 \pm 0.03$ (see Appendix C.7), where n_{sq} is the equivalent thermal occupation of the squeezed state. This demonstrates the direct resolution of features in phase space with a width approximately half that of zero-point fluctuations and the ability to resolve the squeezed character in the number basis.

6.7 Outlook

Mechanical devices are increasingly being integrated into circuit QED systems as resource efficient elements, transducers and quantum memories, which offer access to new regimes of circuit QED [153, 152]. By directly using mechanical instability as a probe, TEA can efficiently measure motion in the presence of additional nonlinear effects. Combining TEA with already demonstrated [151] quantum state transfer techniques provides a path towards efficient tomography of non-Gaussian states in macroscopic mechanical oscillators.

Chapter 7

Conclusion

In this work I coupled technology from cavity quantum electrodynamics with a modular electro-optomechanical transducer and demonstrated readout of a superconducting qubit in the optical domain. Although the electro-optic transducer still adds slightly too much noise to enable the transduction of quantum states, this work firmly establishes that the integration of superconducting qubits with optical technologies is possible. This thesis provides a clear path forward to quantum enabled transduction of photons from a circuit QED system. In Chapter 2 I established the theoretical requirements for interfacing electro-optic transducers with superconducting qubits. In Chapter 3 I outlined the relevant performance metrics and experimental elements that are required when interfacing superconducting qubits with the electro-optic transducer. In Chapter 4 I demonstrated optical readout of a superconducting qubit, and found that the quantum efficiency is very close to what is expected when using the qubit as a non-Gaussian resource for the calibration of the optical readout apparatus. In Chapter 5 I verified that the backaction from the electro-optic transducer on the qubit is negligible.

In Chapter 6 I presented work from the beginning of my PhD on transient electromechanical amplification. This focused on efficient pulsed single quadrature measurement of the motion of a mechanical oscillator, and forms a useful technique for performing tomography on mechanical oscillators. Given the use of electromechanical elements in both Chapter 6 and by the electro-optic transducer, this work could have applications in the microwave-to-optical transduction project for both the distribution and measurement of continuous variable entanglement and squeezing.

This work also establishes experimental requirements for the transduction of quantum states from the microwave to the optical domain. As described in Chapter 4, a major limiting factor was the relatively narrow bandwidth of the electro-optic transducer relative to the bandwidth of the pulse emitted by the circuit QED system. Additionally, this inefficiency had a significant effect on the input-referred added noise (noise referred to the output of the circuit QED system) $N_{\mathrm{cQED}} = N_{\mathrm{t}}/\eta_{\mathrm{loss}}$, which when maximizing for the efficiency of the transduction process, yielded $N_{\mathrm{cQED}} =$ 740 photons. This is of course far from the value required for quantum-enabled transduction [82] and is limited by insufficient bandwidth, LC circuit loss, transducer efficiency, and pump power-dependent noise generated by the LC circuit [69]. However, there is significant room for optimism, as even moderate improvements in the vacuum electromechanical coupling g_{e} will greatly improve both the efficiency of the transducer and its added noise N_{cQED}, and may soon enable quantum transduction.

An increase in g_{e} would provide many simultaneous improvements to the operation of the transducer by reducing the number of microwave pump photons required to achieve a given transduction bandwidth. For example, $g_{\mathrm{e}}/2\pi = 8$ Hz would enable $\Gamma_{\mathrm{e}} = \Gamma_{\mathrm{o}} = 2\pi \times 5$ kHz and reduce pump power-dependent LC circuit loss, yielding $\eta_{\mathrm{t}} \approx 0.6$. If accompanied by an increase in the qubit decay times to $T_2 = T_1 = 100$ µs, I expect $\eta_{\mathrm{bw}} = 0.9$, and the transducer to be quite close to quantum-enabled with $N_{\mathrm{cQED}} < 10$. Further reductions in added noise, which will be needed to approach the regime such that $N_{\mathrm{cQED}} < 1$, are currently being explored and include the use of wafer bonding to achieve more reliable and even larger electromechanical coupling rates. Given that the microwave-to-optical transduction team has fabricated electromechanical devices with g_{e} at these levels already [76]—just not in a full working electro-optic transducer—these required improvements seem quite achievable, and quantum enabled transduction of photons from a microwave frequency superconducting qubit to the optical domain should be well within reach.

Perhaps the most exciting finding of this work is that with proper isolation (described in Chapter 5) superconducting qubits are completely compatible with this type of electro-optic transducer, as indicated by the minimal backaction of the transducer on the qubit. Due to the vastly

different energy scales between microwave and optical photons, coherent pump fields are required universally by all current techniques for electro-optic transduction. Given that superconducting qubits are extremely sensitive to microwave photons, and completely incompatible with optical photons, it is reasonable to be concerned about the proper operation of the circuit QED system when running the electro-optic transducer. However, I found that with sufficient non-reciprocal isolation between the two systems, there exists only a small amount of heating and backaction from the microwave pump, and there is no measurable influence of the optical pump on the superconducting qubit. Thus, with the aforementioned improvements to the transduction efficiency and added noise, continuous transduction of quantum signals from a circuit QED system to the optical domain should be possible.

Bibliography

[1] K. Beauchamp, History of telegraphy. No. 26, Iet, 2001.

[2] M. Guarnieri, "Messaging before the internet-early electrical telegraphs [historical]," IEEE Industrial Electronics Magazine, vol. 13, no. 1, pp. 38–53, 2019.

[3] R. W. Burns, "Communications: an international history of the formative years," IET, 2004.

[4] Y. Tamura, H. Sakuma, K. Morita, M. Suzuki, Y. Yamamoto, K. Shimada, Y. Honma, K. Sohma, T. Fujii, and T. Hasegawa, "The first 0.14-db/km loss optical fiber and its impact on submarine transmission," Journal of Lightwave Technology, vol. 36, no. 1, pp. 44–49, 2018.

[5] H.-J. Briegel, W. Dür, J. I. Cirac, and P. Zoller, "Quantum repeaters: the role of imperfect local operations in quantum communication," Physical Review Letters, vol. 81, no. 26, p. 5932, 1998.

[6] H. J. Kimble, "The quantum internet," Nature, vol. 453, no. 7198, pp. 1023–1030, 2008.

[7] S. Wehner, D. Elkouss, and R. Hanson, "Quantum internet: A vision for the road ahead," Science, vol. 362, no. 6412, 2018.

[8] A. S. Cacciapuoti, M. Caleffi, F. Tafuri, F. S. Cataliotti, S. Gherardini, and G. Bianchi, "Quantum internet: networking challenges in distributed quantum computing," IEEE Network, vol. 34, no. 1, pp. 137–143, 2019.

[9] J. Bardeen and W. H. Brattain, "The transistor, a semi-conductor triode," Physical Review, vol. 74, no. 2, p. 230, 1948.

[10] M. Gong, M.-C. Chen, Y. Zheng, S. Wang, C. Zha, H. Deng, Z. Yan, H. Rong, Y. Wu, S. Li, et al., "Genuine 12-qubit entanglement on a superconducting quantum processor," Physical Review Letters, vol. 122, no. 11, p. 110501, 2019.

[11] E. Chertkov, J. Bohnet, D. Francois, J. Gaebler, D. Gresh, A. Hankin, K. Lee, R. Tobey, D. Hayes, B. Neyenhuis, et al., "Holographic dynamics simulations with a trapped ion quantum computer," arXiv preprint arXiv:2105.09324, 2021.

[12] F. Arute, K. Arya, R. Babbush, D. Bacon, J. C. Bardin, R. Barends, R. Biswas, S. Boixo, F. G. Brandao, D. A. Buell, et al., "Quantum supremacy using a programmable superconducting processor," Nature, vol. 574, no. 7779, pp. 505–510, 2019.

[13] H.-S. Zhong, H. Wang, Y.-H. Deng, M.-C. Chen, L.-C. Peng, Y.-H. Luo, J. Qin, D. Wu, X. Ding, Y. Hu, et al., "Quantum computational advantage using photons," Science, vol. 370, no. 6523, pp. 1460–1463, 2020.

[14] T. D. Ladd, F. Jelezko, R. Laflamme, Y. Nakamura, C. Monroe, and J. L. O'Brien, "Quantum computers," Nature, vol. 464, no. 7285, pp. 45–53, 2010.

[15] P. W. Shor, "Polynomial-time algorithms for prime factorization and discrete logarithms on a quantum computer," SIAM review, vol. 41, no. 2, pp. 303–332, 1999.

[16] I. Georgescu, "Trapped ion quantum computing turns 25," Nature Reviews Physics, vol. 2, no. 6, pp. 278–278, 2020.

[17] M. Saffman, "Quantum computing with neutral atoms," National Science Review, vol. 6, no. 1, pp. 24–25, 2019.

[18] S. Takeda and A. Furusawa, "Toward large-scale fault-tolerant universal photonic quantum computing," APL Photonics, vol. 4, no. 6, p. 060902, 2019.

[19] Y. Nakamura, Y. A. Pashkin, and J. S. Tsai, "Coherent control of macroscopic quantum states in a single-cooper-pair box," Nature, vol. 398, no. 6730, pp. 786–788, 1999.

[20] P. Krantz, M. Kjaergaard, F. Yan, T. P. Orlando, S. Gustavsson, and W. D. Oliver, "A quantum engineer's guide to superconducting qubits," Applied Physics Reviews, vol. 6, no. 2, p. 021318, 2019.

[21] B. D. Josephson, "Possible new effects in superconductive tunnelling," Physics Letters, vol. 1, no. 7, pp. 251–253, 1962.

[22] J. Koch, Y. M. Terri, J. Gambetta, A. A. Houck, D. I. Schuster, J. Majer, A. Blais, M. H. Devoret, S. M. Girvin, and R. J. Schoelkopf, "Charge-insensitive qubit design derived from the cooper pair box," Physical Review A, vol. 76, no. 4, p. 042319, 2007.

[23] N. Foroozani, C. Hobbs, C. C. Hung, S. Olson, D. Ashworth, E. Holland, M. Malloy, P. Kearney, B. O'Brien, B. Bunday, et al., "Development of transmon qubits solely from optical lithography on 300 mm wafers," Quantum Science and Technology, vol. 4, no. 2, p. 025012, 2019.

[24] I. Tsioutsios, K. Serniak, S. Diamond, V. V. Sivak, Z. Wang, S. Shankar, L. Frunzio, R. J. Schoelkopf, and M. H. Devoret, "Free-standing silicon shadow masks for transmon qubit fabrication," AIP Advances, vol. 10, no. 6, p. 065120, 2020.

[25] A. Stehli, J. D. Brehm, T. Wolz, P. Baity, S. Danilin, V. Seferai, H. Rotzinger, A. V. Ustinov, and M. Weides, "Coherent superconducting qubits from a subtractive junction fabrication process," Applied Physics Letters, vol. 117, no. 12, p. 124005, 2020.

[26] C. Monroe, D. M. Meekhof, B. E. King, W. M. Itano, and D. J. Wineland, "Demonstration of a fundamental quantum logic gate," Physical Review Letters, vol. 75, no. 25, p. 4714, 1995.

[27] P. Polimeno, A. Magazzu, M. A. Iati, F. Patti, R. Saija, C. D. E. Boschi, M. G. Donato, P. G. Gucciardi, P. H. Jones, G. Volpe, et al., "Optical tweezers and their applications," Journal of Quantitative Spectroscopy and Radiative Transfer, vol. 218, pp. 131–150, 2018.

[28] D. Ristè, C. C. Bultink, M. J. Tiggelman, R. N. Schouten, K. W. Lehnert, and L. DiCarlo, "Millisecond charge-parity fluctuations and induced decoherence in a superconducting transmon qubit," Nature Communications, vol. 4, no. 1, pp. 1–6, 2013.

[29] I. M. Pop, K. Geerlings, G. Catelani, R. J. Schoelkopf, L. I. Glazman, and M. H. Devoret, "Coherent suppression of electromagnetic dissipation due to superconducting quasiparticles," Nature, vol. 508, no. 7496, pp. 369–372, 2014.

[30] G. Catelani, R. J. Schoelkopf, M. H. Devoret, and L. I. Glazman, "Relaxation and frequency shifts induced by quasiparticles in superconducting qubits," Physical Review B, vol. 84, no. 6, p. 064517, 2011.

[31] C. Wang, Y. Y. Gao, I. M. Pop, U. Vool, C. Axline, T. Brecht, R. W. Heeres, L. Frunzio, M. H. Devoret, G. Catelani, et al., "Measurement and control of quasiparticle dynamics in a superconducting qubit," Nature Communications, vol. 5, no. 1, pp. 1–7, 2014.

[32] Y. Ma, Y. Xu, X. Mu, W. Cai, L. Hu, W. Wang, X. Pan, H. Wang, Y. Song, C.-L. Zou, et al., "Error-transparent operations on a logical qubit protected by quantum error correction," Nature Physics, vol. 16, no. 8, pp. 827–831, 2020.

[33] N. Ofek, A. Petrenko, R. Heeres, P. Reinhold, Z. Leghtas, B. Vlastakis, Y. Liu, L. Frunzio, S. Girvin, L. Jiang, et al., "Extending the lifetime of a quantum bit with error correction in superconducting circuits," Nature, vol. 536, no. 7617, pp. 441–445, 2016.

[34] P. Campagne-Ibarcq, A. Eickbusch, S. Touzard, E. Zalys-Geller, N. E. Frattini, V. V. Sivak, P. Reinhold, S. Puri, S. Shankar, R. J. Schoelkopf, et al., "Quantum error correction of a qubit encoded in grid states of an oscillator," Nature, vol. 584, no. 7821, pp. 368–372, 2020.

[35] M. D. Reed, L. DiCarlo, S. E. Nigg, L. Sun, L. Frunzio, S. M. Girvin, and R. J. Schoelkopf, "Realization of three-qubit quantum error correction with superconducting circuits," Nature, vol. 482, no. 7385, pp. 382–385, 2012.

[36] D. J. Reilly, "Challenges in scaling-up the control interface of a quantum computer," in 2019 IEEE International Electron Devices Meeting (IEDM), pp. 31–7, IEEE, 2019.

[37] F. Lecocq, F. Quinlan, K. Cicak, J. Aumentado, S. Diddams, and J. Teufel, "Control and readout of a superconducting qubit using a photonic link," Nature, vol. 591, no. 7851, pp. 575–579, 2021.

[38] P. Magnard, S. Storz, P. Kurpiers, J. Schär, F. Marxer, J. Lütolf, T. Walter, J.-C. Besse, M. Gabureac, K. Reuer, et al., "Microwave quantum link between superconducting circuits housed in spatially separated cryogenic systems," Physical Review Letters, vol. 125, no. 26, p. 260502, 2020.

[39] A. Youssefi, I. Shomroni, Y. J. Joshi, N. R. Bernier, A. Lukashchuk, P. Uhrich, L. Qiu, and T. J. Kippenberg, "A cryogenic electro-optic interconnect for superconducting devices," Nature Electronics, vol. 4, no. 5, pp. 326–332, 2021.

[40] C. Cabrillo, J. I. Cirac, P. Garcia-Fernandez, and P. Zoller, "Creation of entangled states of distant atoms by interference," Physical Review A, vol. 59, no. 2, p. 1025, 1999.

[41] S. Bose, P. Knight, M. Plenio, and V. Vedral, "Proposal for teleportation of an atomic state via cavity decay," Physical Review Letters, vol. 83, no. 24, p. 5158, 1999.

[42] D. E. Browne, M. B. Plenio, and S. F. Huelga, "Robust creation of entanglement between ions in spatially separate cavities," Physical Review Letters, vol. 91, no. 6, p. 067901, 2003.

[43] E. T. Campbell and S. C. Benjamin, "Measurement-based entanglement under conditions of extreme photon loss," Physical Review Letters, vol. 101, no. 13, p. 130502, 2008.

[44] F. Grosshans and P. Grangier, "Continuous variable quantum cryptography using coherent states," Physical Review Letters, vol. 88, no. 5, p. 057902, 2002.

[45] R. Ursin, F. Tiefenbacher, T. Schmitt-Manderbach, H. Weier, T. Scheidl, M. Lindenthal, B. Blauensteiner, T. Jennewein, J. Perdigues, P. Trojek, et al., "Entanglement-based quantum communication over 144 km," Nature Physics, vol. 3, no. 7, pp. 481–486, 2007.

[46] T. Inagaki, N. Matsuda, O. Tadanaga, M. Asobe, and H. Takesue, "Entanglement distribution over 300 km of fiber," Optics Express, vol. 21, no. 20, pp. 23241–23249, 2013.

[47] J. Yin, Y. Cao, Y.-H. Li, S.-K. Liao, L. Zhang, J.-G. Ren, W.-Q. Cai, W.-Y. Liu, B. Li, H. Dai, et al., "Satellite-based entanglement distribution over 1200 kilometers," Science, vol. 356, no. 6343, pp. 1140–1144, 2017.

[48] H.-L. Yin, T.-Y. Chen, Z.-W. Yu, H. Liu, L.-X. You, Y.-H. Zhou, S.-J. Chen, Y. Mao, M.-Q. Huang, W.-J. Zhang, et al., "Measurement-device-independent quantum key distribution over a 404 km optical fiber," Physical Review Letters, vol. 117, no. 19, p. 190501, 2016.

[49] A. Boaron, G. Boso, D. Rusca, C. Vulliez, C. Autebert, M. Caloz, M. Perrenoud, G. Gras, F. Bussières, M.-J. Li, et al., "Secure quantum key distribution over 421 km of optical fiber," Physical Review Letters, vol. 121, no. 19, p. 190502, 2018.

[50] S. Wengerowsky, S. K. Joshi, F. Steinlechner, J. R. Zichi, S. M. Dobrovolskiy, R. van der Molen, J. W. Los, V. Zwiller, M. A. Versteegh, A. Mura, et al., "Entanglement distribution over a 96-km-long submarine optical fiber," Proceedings of the National Academy of Sciences, vol. 116, no. 14, pp. 6684–6688, 2019.

[51] Y. Cao, Y.-H. Li, K.-X. Yang, Y.-F. Jiang, S.-L. Li, X.-L. Hu, M. Abulizi, C.-L. Li, W. Zhang, Q.-C. Sun, et al., "Long-distance free-space measurement-device-independent quantum key distribution," Physical Review Letters, vol. 125, no. 26, p. 260503, 2020.

[52] C. J. Axline, L. D. Burkhart, W. Pfaff, M. Zhang, K. Chou, P. Campagne-Ibarcq, P. Reinhold, L. Frunzio, S. Girvin, L. Jiang, et al., "On-demand quantum state transfer and entanglement between remote microwave cavity memories," Nature Physics, vol. 14, no. 7, pp. 705–710, 2018.

[53] N. Lauk, N. Sinclair, S. Barzanjeh, J. P. Covey, M. Saffman, M. Spiropulu, and C. Simon, "Perspectives on quantum transduction," Quantum Science and Technology, vol. 5, no. 2, p. 020501, 2020.

[54] R. Hisatomi, A. Osada, Y. Tabuchi, T. Ishikawa, A. Noguchi, R. Yamazaki, K. Usami, and Y. Nakamura, "Bidirectional conversion between microwave and light via ferromagnetic magnons," Physical Review B, vol. 93, no. 17, p. 174427, 2016.

[55] J. Han, T. Vogt, C. Gross, D. Jaksch, M. Kiffner, and W. Li, "Coherent microwave-to-optical conversion via six-wave mixing in rydberg atoms," Physical Review Letters, vol. 120, no. 9, p. 093201, 2018.

[56] A. P. Higginbotham, P. S. Burns, M. D. Urmey, R. W. Peterson, N. S. Kampel, B. M. Brubaker, G. Smith, K. W. Lehnert, and C. A. Regal, "Harnessing electro-optic correlations in an efficient mechanical converter," Nature Physics, vol. 14, no. 10, pp. 1038–1042, 2018.

[57] L. Fan, C.-L. Zou, R. Cheng, X. Guo, X. Han, Z. Gong, S. Wang, and H. X. Tang, "Superconducting cavity electro-optics: a platform for coherent photon conversion between superconducting and photonic circuits," Science Advances, vol. 4, no. 8, p. eaar4994, 2018.

[58] J. Bochmann, A. Vainsencher, D. D. Awschalom, and A. N. Cleland, "Nanomechanical coupling between microwave and optical photons," Nature Physics, vol. 9, no. 11, pp. 712–716, 2013.

[59] W. Jiang, C. J. Sarabalis, Y. D. Dahmani, R. N. Patel, F. M. Mayor, T. P. McKenna, R. Van Laer, and A. H. Safavi-Naeini, "Efficient bidirectional piezo-optomechanical transduction between microwave and optical frequency," Nature Communications, vol. 11, no. 1, pp. 1–7, 2020.

[60] M. Forsch, R. Stockill, A. Wallucks, I. Marinković, C. Gärtner, R. A. Norte, F. van Otten, A. Fiore, K. Srinivasan, and S. Gröblacher, "Microwave-to-optics conversion using a mechanical oscillator in its quantum ground state," Nature Physics, vol. 16, no. 1, pp. 69–74, 2020.

[61] R. Stockill, M. Forsch, F. Hijazi, G. Beaudoin, K. Pantzas, I. Sagnes, R. Braive, and S. Gröblacher, "Ultra-low-noise microwave to optics conversion in gallium phosphide," arXiv preprint arXiv:2107.04433, 2021.

[62] M. Mirhosseini, A. Sipahigil, M. Kalaee, and O. Painter, "Superconducting qubit to optical photon transduction," Nature, vol. 588, no. 7839, pp. 599–603, 2020.

[63] J. D. Witmer, T. P. McKenna, P. Arrangoiz-Arriola, R. Van Laer, E. A. Wollack, F. Lin, A. K. Y. Jen, J. Luo, and A. H. Safavi-Naeini, "A silicon-organic hybrid platform for quantum microwave-to-optical transduction," Quantum Science and Technology, vol. 5, no. 3, p. 034004, 2020.

[64] J. G. Bartholomew, J. Rochman, T. Xie, J. M. Kindem, A. Ruskuc, I. Craiciu, M. Lei, and A. Faraon, "On-chip coherent microwave-to-optical transduction mediated by ytterbium in yvo 4," Nature Communications, vol. 11, no. 1, pp. 1–6, 2020.

[65] R. Sahu, W. Hease, A. Rueda, G. Arnold, L. Qiu, and J. Fink, "Quantum-enabled interface between microwave and telecom light," arXiv preprint arXiv:2107.08303, 2021.

[66] W. Hease, A. Rueda, R. Sahu, M. Wulf, G. Arnold, H. G. L. Schwefel, and J. M. Fink, "Bidirectional electro-optic wavelength conversion in the quantum ground state," PRX Quantum, vol. 1, no. 2, p. 020315, 2020.

[67] R. W. Andrews, R. W. Peterson, T. P. Purdy, K. Cicak, R. W. Simmonds, C. A. Regal, and K. W. Lehnert, "Bidirectional and efficient conversion between microwave and optical light," Nature Physics, vol. 10, no. 4, pp. 321–326, 2014.

[68] D. Stucki, N. Walenta, F. Vannel, R. T. Thew, N. Gisin, H. Zbinden, S. Gray, C. Towery, and S. Ten, "High rate, long-distance quantum key distribution over 250 km of ultra low loss fibres," New Journal of Physics, vol. 11, no. 7, p. 075003, 2009.

[69] B. M. Brubaker, J. M. Kindem, M. D. Urmey, S. Mittal, R. D. Delaney, P. S. Burns, M. R. Vissers, K. W. Lehnert, and C. A. Regal, "Optomechanical ground-state cooling in a continuous and efficient electro-optic transducer," arXiv preprint arXiv:2112.13429, 2021.

[70] D. F. Walls and G. J. Milburn, Quantum optics. Springer Science & Business Media, 2007.

[71] W. Fu, M. Xu, X. Liu, C.-L. Zou, C. Zhong, X. Han, M. Shen, Y. Xu, R. Cheng, S. Wang, et al., "Cavity electro-optic circuit for microwave-to-optical conversion in the quantum ground state," Physical Review A, vol. 103, no. 5, p. 053504, 2021.

[72] M. Li and H. X. Tang, "Strong pockels materials," Nature Materials, vol. 18, no. 1, pp. 9–11, 2019.

[73] C. Gardiner, P. Zoller, and P. Zoller, Quantum noise: a handbook of Markovian and non-Markovian quantum stochastic methods with applications to quantum optics. Springer Science & Business Media, 2004.

[74] C. M. Caves, "Quantum limits on noise in linear amplifiers," Physical Review D, vol. 26, no. 8, p. 1817, 1982.

[75] A. Jayich, J. Sankey, B. Zwickl, C. Yang, J. Thompson, S. Girvin, A. Clerk, F. Marquardt, and J. Harris, "Dispersive optomechanics: a membrane inside a cavity," New Journal of Physics, vol. 10, no. 9, p. 095008, 2008.

[76] P. S. Burns, Reducing Added Noise in a Microwave-mechanical-optical Converter. PhD thesis, University of Colorado at Boulder, 2020.

[77] R. D. Delaney, M. D. Urmey, S. Mittal, B. M. Brubaker, J. M. Kindem, P. S. Burns, C. A. Regal, and K. W. Lehnert, "Non-destructive optical readout of a superconducting qubit," arXiv preprint arXiv:2110.09539, 2021.

[78] C.-T. Chen, "Linear system theory and design," 1999.

[79] M. Aspelmeyer, T. J. Kippenberg, and F. Marquardt, "Cavity optomechanics," Rev. Mod. Phys., vol. 86, no. 4, p. 1391, 2014.

[80] J. Gambetta, W. A. Braff, A. Wallraff, S. M. Girvin, and R. J. Schoelkopf, "Protocols for optimal readout of qubits using a continuous quantum nondemolition measurement," Physical Review A, vol. 76, no. 1, p. 012325, 2007.

[81] I. Galinskiy, Y. Tsaturyan, M. Parniak, and E. S. Polzik, "Phonon counting thermometry of an ultracoherent membrane resonator near its motional ground state," Optica, vol. 7, no. 6, pp. 718–725, 2020.

[82] E. Zeuthen, A. Schliesser, A. S. Sørensen, and J. M. Taylor, "Figures of merit for quantum transducers," Quantum Sci. Technol., vol. 5, no. 3, p. 034009, 2020.

[83] R. W. Andrews, Quantum signal processing with mechanical oscillators. PhD thesis, University of Colorado at Boulder, 2015.

[84] A. A. Houck, J. A. Schreier, B. R. Johnson, J. M. Chow, J. Koch, J. M. Gambetta, D. I. Schuster, L. Frunzio, M. H. Devoret, S. M. Girvin, et al., "Controlling the spontaneous emission of a superconducting transmon qubit," Physical Review Letters, vol. 101, no. 8, p. 080502, 2008.

[85] N. Lütkenhaus and S. M. Barnett, "Nonclassical effects in phase space," Physical Review A, vol. 51, no. 4, p. 3340, 1995.

[86] G. Nogues, A. Rauschenbeutel, S. Osnaghi, P. Bertet, M. Brune, J. Raimond, S. Haroche, L. Lutterbach, and L. Davidovich, "Measurement of a negative value for the wigner function of radiation," Physical Review A, vol. 62, no. 5, p. 054101, 2000.

[87] R. D. Delaney, A. P. Reed, R. W. Andrews, and K. W. Lehnert, "Measurement of motion beyond the quantum limit by transient amplification," Physical Review Letters, vol. 123, no. 18, p. 183603, 2019.

[88] P. Campagne-Ibarcq, E. Zalys-Geller, A. Narla, S. Shankar, P. Reinhold, L. Burkhart, C. Axline, W. Pfaff, L. Frunzio, R. Schoelkopf, et al., "Deterministic remote entanglement of superconducting circuits through microwave two-photon transitions," Physical Review Letters, vol. 120, no. 20, p. 200501, 2018.

[89] M. M. Weston, S. Slussarenko, H. M. Chrzanowski, S. Wollmann, L. K. Shalm, V. B. Verma, M. S. Allman, S. W. Nam, and G. J. Pryde, "Heralded quantum steering over a high-loss channel," Science Advances, vol. 4, no. 1, p. e1701230, 2018.

[90] J.-W. Pan, D. Bouwmeester, H. Weinfurter, and A. Zeilinger, "Experimental entanglement swapping: entangling photons that never interacted," Physical Review Letters, vol. 80, no. 18, p. 3891, 1998.

[91] R. Kaltenbaek, R. Prevedel, M. Aspelmeyer, and A. Zeilinger, "High-fidelity entanglement swapping with fully independent sources," Physical Review A, vol. 79, no. 4, p. 040302, 2009.

[92] R.-B. Jin, M. Takeoka, U. Takagi, R. Shimizu, and M. Sasaki, "Highly efficient entanglement swapping and teleportation at telecom wavelength," Scientific Reports, vol. 5, no. 1, pp. 1–7, 2015.

[93] H. Shibata, T. Honjo, and K. Shimizu, "Quantum key distribution over a 72 db channel loss using ultralow dark count superconducting single-photon detectors," Optics Letters, vol. 39, no. 17, pp. 5078–5081, 2014.

[94] H. Shibata, K. Fukao, N. Kirigane, S. Karimoto, and H. Yamamoto, "Snspd with ultimate low system dark count rate using various cold filters," IEEE Transactions on Applied Superconductivity, vol. 27, no. 4, pp. 1–4, 2016.

[95] J. Chiles, S. M. Buckley, A. Lita, V. B. Verma, J. Allmaras, B. Korzh, M. D. Shaw, J. M. Shainline, R. P. Mirin, and S. W. Nam, "Superconducting microwire detectors based on wsi with single-photon sensitivity in the near-infrared," Applied Physics Letters, vol. 116, no. 24, p. 242602, 2020.

[96] D. M. Pozar, Microwave engineering. John Wiley & Sons, 2011.

[97] R. Peterson, T. Purdy, N. Kampel, R. Andrews, P.-L. Yu, K. Lehnert, and C. Regal, "Laser cooling of a micromechanical membrane to the quantum backaction limit," Physical Review Letters, vol. 116, no. 6, p. 063601, 2016.

[98] M. Reagor, W. Pfaff, C. Axline, R. W. Heeres, N. Ofek, K. Sliwa, E. Holland, C. Wang, J. Blumoff, K. Chou, et al., "Quantum memory with millisecond coherence in circuit qed," Physical Review B, vol. 94, no. 1, p. 014506, 2016.

[99] A. P. Place, L. V. Rodgers, P. Mundada, B. M. Smitham, M. Fitzpatrick, Z. Leng, A. Premkumar, J. Bryon, A. Vrajitoarea, S. Sussman, et al., "New material platform for superconducting transmon qubits with coherence times exceeding 0.3 milliseconds," Nature Communications, vol. 12, no. 1, pp. 1–6, 2021.

[100] C. Wang, X. Li, H. Xu, Z. Li, J. Wang, Z. Yang, Z. Mi, X. Liang, T. Su, C. Yang, et al., "Transmon qubit with relaxation time exceeding 0.5 milliseconds," arXiv preprint arXiv:2105.09890, 2021.

[101] K. Geerlings, Z. Leghtas, I. M. Pop, S. Shankar, L. Frunzio, R. J. Schoelkopf, M. Mirrahimi, and M. H. Devoret, "Demonstrating a driven reset protocol for a superconducting qubit," Physical Review Letters, vol. 110, no. 12, p. 120501, 2013.

[102] D. Ristè, J. G. van Leeuwen, H.-S. Ku, K. W. Lehnert, and L. DiCarlo, "Initialization by measurement of a superconducting quantum bit circuit," Physical Review Letters, vol. 109, no. 5, p. 050507, 2012.

[103] D. Ristè, C. Bultink, K. W. Lehnert, and L. DiCarlo, "Feedback control of a solid-state qubit using high-fidelity projective measurement," Physical Review Letters, vol. 109, no. 24, p. 240502, 2012.

[104] P. Magnard, P. Kurpiers, B. Royer, T. Walter, J.-C. Besse, S. Gasparinetti, M. Pechal, J. Heinsoo, S. Storz, A. Blais, et al., "Fast and unconditional all-microwave reset of a superconducting qubit," Physical Review Letters, vol. 121, no. 6, p. 060502, 2018.

[105] C. Macklin, K. O'Brien, D. Hover, M. E. Schwartz, V. Bolkhovsky, X. Zhang, W. D. Oliver, and I. Siddiqi, "A near–quantum-limited josephson traveling-wave parametric amplifier," Science, vol. 350, no. 6258, pp. 307–310, 2015.

[106] C. C. Bultink, B. Tarasinski, N. Haandbæk, S. Poletto, N. Haider, D. J. Michalak, A. Bruno, and L. DiCarlo, "General method for extracting the quantum efficiency of dispersive qubit readout in circuit qed," Applied Physics Letters, vol. 112, no. 9, p. 092601, 2018.

[107] A. Eddins, J. M. Kreikebaum, D. M. Toyli, E. M. Levenson-Falk, A. Dove, W. P. Livingston, B. A. Levitan, L. C. G. Govia, A. A. Clerk, and I. Siddiqi, "High-efficiency measurement of an artificial atom embedded in a parametric amplifier," Physical Review X, vol. 9, no. 1, p. 011004, 2019.

[108] S. Touzard, A. Kou, N. E. Frattini, V. V. Sivak, S. Puri, A. Grimm, L. Frunzio, S. Shankar, and M. H. Devoret, "Gated conditional displacement readout of superconducting qubits," Physical Review Letters, vol. 122, no. 8, p. 080502, 2019.

[109] E. I. Rosenthal, C. M. Schneider, M. Malnou, Z. Zhao, F. Leditzky, B. J. Chapman, W. Wustmann, X. Ma, D. A. Palken, M. F. Zanner, et al., "Efficient and low-backaction quantum measurement using a chip-scale detector," Physical Review Letters, vol. 126, no. 9, p. 090503, 2021.

[110] B. W. Shore and P. L. Knight, "The jaynes-cummings model," Journal of Modern Optics, vol. 40, no. 7, pp. 1195–1238, 1993.

[111] I. Chiorescu, Y. Nakamura, C. M. Harmans, and J. Mooij, "Coherent quantum dynamics of a superconducting flux qubit," Science, vol. 299, no. 5614, pp. 1869–1871, 2003.

[112] A. Wallraff, D. I. Schuster, A. Blais, L. Frunzio, R.-S. Huang, J. Majer, S. Kumar, S. M. Girvin, and R. J. Schoelkopf, "Strong coupling of a single photon to a superconducting qubit using circuit quantum electrodynamics," Nature, vol. 431, no. 7005, pp. 162–167, 2004.

[113] A. Wallraff, D. Schuster, A. Blais, L. Frunzio, J. Majer, M. Devoret, S. Girvin, and R. Schoelkopf, "Approaching unit visibility for control of a superconducting qubit with dispersive readout," Physical Review Letters, vol. 95, no. 6, p. 060501, 2005.

[114] M. Boissonneault, J. M. Gambetta, and A. Blais, "Dispersive regime of circuit qed: Photon-dependent qubit dephasing and relaxation rates," Physical Review A, vol. 79, no. 1, p. 013819, 2009.

[115] A. Clerk, K. Lehnert, P. Bertet, J. Petta, and Y. Nakamura, "Hybrid quantum systems with circuit quantum electrodynamics," Nature Physics, vol. 16, no. 3, pp. 257–267, 2020.

[116] F. Yan, D. Campbell, P. Krantz, M. Kjaergaard, D. Kim, J. L. Yoder, D. Hover, A. Sears, A. J. Kerman, T. P. Orlando, et al., "Distinguishing coherent and thermal photon noise in a circuit quantum electrodynamical system," Physical Review Letters, vol. 120, no. 26, p. 260504, 2018.

[117] J. D. Teufel, T. Donner, D. Li, J. W. Harlow, M. S. Allman, K. Cicak, A. J. Sirois, J. D. Whittaker, K. W. Lehnert, and R. W. Simmonds, "Sideband cooling of micromechanical motion to the quantum ground state," Nature, vol. 475, no. 7356, pp. 359–363, 2011.

[118] J. Gambetta, A. Blais, D. I. Schuster, A. Wallraff, L. Frunzio, J. Majer, M. H. Devoret, S. M. Girvin, and R. J. Schoelkopf, "Qubit-photon interactions in a cavity: Measurement-induced dephasing and number splitting," Physical Review A, vol. 74, no. 4, p. 042318, 2006.

[119] A. F. Kockum, L. Tornberg, and G. Johansson, "Undoing measurement-induced dephasing in circuit qed," Physical Review A, vol. 85, no. 5, p. 052318, 2012.

[120] Z. Wang, S. Shankar, Z. K. Minev, P. Campagne-Ibarcq, A. Narla, and M. H. Devoret, "Cavity attenuators for superconducting qubits," Physical Review Applied, vol. 11, no. 1, p. 014031, 2019.

[121] J.-H. Yeh, J. LeFebvre, S. Premaratne, F. Wellstood, and B. Palmer, "Microwave attenuators for use with quantum devices below 100 mk," Journal of Applied Physics, vol. 121, no. 22, p. 224501, 2017.

[122] C. Gerry, P. Knight, and P. L. Knight, Introductory quantum optics. Cambridge university press, 2005.

[123] D. Sank, Z. Chen, M. Khezri, J. Kelly, R. Barends, B. Campbell, Y. Chen, B. Chiaro, A. Dunsworth, A. Fowler, et al., "Measurement-induced state transitions in a superconducting qubit: Beyond the rotating wave approximation," Physical Review Letters, vol. 117, no. 19, p. 190503, 2016.

[124] M. Brune, E. Hagley, J. Dreyer, X. Maitre, A. Maali, C. Wunderlich, J. Raimond, and S. Haroche, "Observing the progressive decoherence of the "meter" in a quantum measurement," Physical Review Letters, vol. 77, no. 24, p. 4887, 1996.

[125] M. Brune, F. Schmidt-Kaler, A. Maali, J. Dreyer, E. Hagley, J. Raimond, and S. Haroche, "Quantum rabi oscillation: A direct test of field quantization in a cavity," Physical Review Letters, vol. 76, no. 11, p. 1800, 1996.

[126] J. Raimond, M. Brune, and S. Haroche, "Reversible decoherence of a mesoscopic superposition of field states," Physical Review Letters, vol. 79, no. 11, p. 1964, 1997.

[127] A. P. Sears, A. Petrenko, G. Catelani, L. Sun, H. Paik, G. Kirchmair, L. Frunzio, L. I. Glazman, S. M. Girvin, and R. J. Schoelkopf, "Photon shot noise dephasing in the strong-dispersive limit of circuit qed," Physical Review B, vol. 86, no. 18, p. 180504, 2012.

[128] C. Zhong, Z. Wang, C. Zou, M. Zhang, X. Han, W. Fu, M. Xu, S. Shankar, M. H. Devoret, H. X. Tang, et al., "Proposal for heralded generation and detection of entangled microwave–optical-photon pairs," Physical Review Letters, vol. 124, no. 1, p. 010511, 2020.

[129] P. Kurpiers, P. Magnard, T. Walter, B. Royer, M. Pechal, J. Heinsoo, Y. Salathé, A. Akin, S. Storz, J.-C. Besse, et al., "Deterministic quantum state transfer and remote entanglement using microwave photons," Nature, vol. 558, no. 7709, pp. 264–267, 2018.

[130] N. Kalb, A. A. Reiserer, P. C. Humphreys, J. J. W. Bakermans, S. J. Kamerling, N. H. Nickerson, S. C. Benjamin, D. J. Twitchen, M. Markham, and R. Hanson, "Entanglement distillation between solid-state quantum network nodes," Science, vol. 356, no. 6341, pp. 928–932, 2017.

[131] M. Pompili, S. L. N. Hermans, S. Baier, H. K. C. Beukers, P. C. Humphreys, R. N. Schouten, R. F. L. Vermeulen, M. J. Tiggelman, L. dos Santos Martins, B. Dirkse, et al., "Realization of a multinode quantum network of remote solid-state qubits," Science, vol. 372, no. 6539, pp. 259–264, 2021.

[132] W. F. Kindel, M. Schroer, and K. Lehnert, "Generation and efficient measurement of single photons from fixed-frequency superconducting qubits," Physical Review A, vol. 93, no. 3, p. 033817, 2016.

[133] W. F. Kindel, Generation and efficient measurement of single photons using superconducting circuits. PhD thesis, University of Colorado at Boulder, 2015.

[134] P. Leek, S. Filipp, P. Maurer, M. Baur, R. Bianchetti, J. Fink, M. Göppl, L. Steffen, and A. Wallraff, "Using sideband transitions for two-qubit operations in superconducting circuits," Physical Review B, vol. 79, no. 18, p. 180511, 2009.

[135] A. Wallraff, D. I. Schuster, A. Blais, J. M. Gambetta, J. Schreier, L. Frunzio, M. H. Devoret, S. M. Girvin, and R. J. Schoelkopf, "Sideband transitions and two-tone spectroscopy of

a superconducting qubit strongly coupled to an on-chip cavity," Physical Review Letters, vol. 99, no. 5, p. 050501, 2007.

[136] F. Mallet, M. A. Castellanos-Beltran, H. S. Ku, S. Glancy, E. Knill, K. D. Irwin, G. C. Hilton, L. R. Vale, and K. W. Lehnert, "Quantum state tomography of an itinerant squeezed microwave field," Physical Review Letters, vol. 106, no. 22, p. 220502, 2011.

[137] A. A. Clerk and D. W. Utami, "Using a qubit to measure photon-number statistics of a driven thermal oscillator," Physical Review A, vol. 75, no. 4, p. 042302, 2007.

[138] C. Rigetti, J. M. Gambetta, S. Poletto, B. L. T. Plourde, J. M. Chow, A. D. Córcoles, J. A. Smolin, S. T. Merkel, J. R. Rozen, G. A. Keefe, et al., "Superconducting qubit in a waveguide cavity with a coherence time approaching 0.1 ms," Physical Review B, vol. 86, no. 10, p. 100506, 2012.

[139] B. Suri, Z. Keane, L. S. Bishop, S. Novikov, F. C. Wellstood, and B. S. Palmer, "Nonlinear microwave photon occupancy of a driven resonator strongly coupled to a transmon qubit," Physical Review A, vol. 92, no. 6, p. 063801, 2015.

[140] S. G. Hofer, W. Wieczorek, M. Aspelmeyer, and K. Hammerer, "Quantum entanglement and teleportation in pulsed cavity optomechanics," Physical Review A, vol. 84, no. 5, p. 052327, 2011.

[141] T. Palomaki, J. Teufel, R. Simmonds, and K. W. Lehnert, "Entangling mechanical motion with microwave fields," Science, vol. 342, no. 6159, pp. 710–713, 2013.

[142] J. Clarke, P. Sahium, K. Khosla, I. Pikovski, M. Kim, and M. Vanner, "Generating mechanical and optomechanical entanglement via pulsed interaction and measurement," New Journal of Physics, vol. 22, no. 6, p. 063001, 2020.

[143] S. Kotler, G. A. Peterson, E. Shojaee, F. Lecocq, K. Cicak, A. Kwiatkowski, S. Geller, S. Glancy, E. Knill, R. W. Simmonds, et al., "Direct observation of deterministic macroscopic entanglement," Science, vol. 372, no. 6542, pp. 622–625, 2021.

[144] L. Qiu, I. Shomroni, P. Seidler, and T. J. Kippenberg, "Laser cooling of a nanomechanical oscillator to its zero-point energy," Physical Review Letters, vol. 124, no. 17, p. 173601, 2020.

[145] C. Ockeloen-Korppi, E. Damskägg, J.-M. Pirkkalainen, M. Asjad, A. Clerk, F. Massel, M. Woolley, and M. Sillanpää, "Stabilized entanglement of massive mechanical oscillators," Nature, vol. 556, no. 7702, pp. 478–482, 2018.

[146] R. Riedinger, A. Wallucks, I. Marinković, C. Löschnauer, M. Aspelmeyer, S. Hong, and S. Gröblacher, "Remote quantum entanglement between two micromechanical oscillators," Nature, vol. 556, no. 7702, p. 473, 2018.

[147] E. E. Wollman, C. U. Lei, A. J. Weinstein, J. Suh, A. Kronwald, F. Marquardt, A. A. Clerk, and K. C. Schwab, "Quantum squeezing of motion in a mechanical resonator," Science, vol. 349, no. 6251, pp. 952–955, 2015.

[148] F. Lecocq, J. B. Clark, R. W. Simmonds, J. Aumentado, and J. D. Teufel, "Quantum nondemolition measurement of a nonclassical state of a massive object," Physical Review X, vol. 5, no. 4, p. 041037, 2015.

[149] J. M. Pirkkalainen, E. Damskägg, M. Brandt, F. Massel, and M. A. Sillanpää, "Squeezing of quantum noise of motion in a micromechanical resonator," Physical Review Letters, vol. 115, p. 243601, Dec 2015.

[150] M. Rossi, D. Mason, J. Chen, Y. Tsaturyan, and A. Schliesser, "Measurement-based quantum control of mechanical motion," Nature, vol. 563, no. 7729, p. 53, 2018.

[151] A. P. Reed, K. H. Mayer, J. D. Teufel, L. D. Burkhart, W. Pfaff, M. Reagor, L. Sletten, X. Ma, R. J. Schoelkopf, E. Knill, et al., "Faithful conversion of propagating quantum information to mechanical motion," Nature Physics, vol. 13, no. 12, pp. 1163–1167, 2017.

[152] Y. Chu, P. Kharel, T. Yoon, L. Frunzio, P. T. Rakich, and R. J. Schoelkopf, "Creation and control of multi-phonon fock states in a bulk acoustic-wave resonator," Nature, vol. 563, no. 7733, p. 666, 2018.

[153] B. A. Moores, L. R. Sletten, J. J. Viennot, and K. W. Lehnert, "Cavity quantum acoustic device in the multimode strong coupling regime," Physical Review Letters, vol. 120, no. 22, p. 227701, 2018.

[154] V. B. Braginsky, Y. I. Vorontsov, and K. S. Thorne, "Quantum nondemolition measurements," Science, vol. 209, no. 4456, pp. 547–557, 1980.

[155] A. A. Clerk, F. Marquardt, and K. Jacobs, "Back-action evasion and squeezing of a mechanical resonator using a cavity detector," New Journal of Physics, vol. 10, no. 9, p. 095010, 2008.

[156] C. U. Lei, A. J. Weinstein, J. Suh, E. E. Wollman, A. Kronwald, F. Marquardt, A. A. Clerk, and K. C. Schwab, "Quantum nondemolition measurement of a quantum squeezed state beyond the 3 db limit," Physical Review Letters, vol. 117, no. 10, p. 100801, 2016.

[157] J. Suh, M. D. Shaw, H. G. LeDuc, A. J. Weinstein, and K. C. Schwab, "Thermally induced parametric instability in a back-action evading measurement of a micromechanical quadrature near the zero-point level," Nano letters, vol. 12, no. 12, pp. 6260–6265, 2012.

[158] J. Suh, A. J. Weinstein, and K. C. Schwab, "Optomechanical effects of two-level systems in a back-action evading measurement of micro-mechanical motion," Applied Physics Letters, vol. 103, no. 5, p. 052604, 2013.

[159] J. Q. Liao, C. K. Law, et al., "Parametric generation of quadrature squeezing of mirrors in cavity optomechanics," Physical Review A, vol. 83, no. 3, p. 033820, 2011.

[160] I. Shomroni, A. Youssefi, N. Sauerwein, L. Qiu, P. Seidler, D. Malz, A. Nunnenkamp, and T. J. Kippenberg, "Two-tone optomechanical instability and its fundamental implications for backaction-evading measurements," Physical Review X, vol. 9, no. 4, p. 041022, 2019.

[161] A. Kronwald, F. Marquardt, and A. A. Clerk, "Arbitrarily large steady-state bosonic squeezing via dissipation," Physical Review A, vol. 88, no. 6, p. 063833, 2013.

[162] A. I. Lvovsky and M. G. Raymer, "Continuous-variable optical quantum-state tomography," Reviews of Modern Physics, vol. 81, no. 1, p. 299, 2009.

[163] R. W. Andrews, A. P. Reed, K. Cicak, J. D. Teufel, and K. W. Lehnert, "Quantum-enabled temporal and spectral mode conversion of microwave signals," Nature Communications, vol. 6, p. 10021, 2015.

[164] T. A. Palomaki, J. W. Harlow, J. D. Teufel, R. W. Simmonds, and K. W. Lehnert, "Coherent state transfer between itinerant microwave fields and a mechanical oscillator," Nature, vol. 495, no. 7440, p. 210, 2013.

[165] B. Yurke and D. Stoler, "Generating quantum mechanical superpositions of macroscopically distinguishable states via amplitude dispersion," Physical Review Letters, vol. 57, no. 1, p. 13, 1986.

[166] A. I. Lvovsky, H. Hansen, T. Aichele, O. Benson, J. Mlynek, and S. Schiller, "Quantum state reconstruction of the single-photon fock state," Physical Review Letters, vol. 87, no. 5, p. 050402, 2001.

[167] A. A. Clerk, M. H. Devoret, S. M. Girvin, F. Marquardt, and R. J. Schoelkopf, "Introduction to quantum noise, measurement, and amplification," Rev. Mod. Phys., vol. 82, no. 2, p. 1155, 2010.

[168] D. T. Smithey, M. Beck, M. G. Raymer, and A. Faridani, "Measurement of the wigner distribution and the density matrix of a light mode using optical homodyne tomography: Application to squeezed states and the vacuum," Physical Review Letters, vol. 70, no. 9, p. 1244, 1993.

[169] K. Vogel and H. Risken, "Determination of quasiprobability distributions in terms of probability distributions for the rotated quadrature phase," Physical Review A, vol. 40, no. 5, p. 2847, 1989.

[170] Z. Hradil, "Quantum-state estimation," Physical Review A, vol. 55, no. 3, p. R1561, 1997.

[171] M. Christandl and R. Renner, "Reliable quantum state tomography," Physical Review Letters, vol. 109, no. 12, p. 120403, 2012.

[172] M. S. Kim, F. A. M. De Oliveira, and P. L. Knight, "Photon number distributions for squeezed number states and squeezed thermal states," Optics Communications, vol. 72, no. 1-2, pp. 99–103, 1989.

[173] J. Řeháček, S. Olivares, D. Mogilevtsev, Z. Hradil, M. G. A. Paris, S. Fornaro, V. D'Auria, A. Porzio, and S. Solimeno, "Effective method to estimate multidimensional gaussian states," Physical Review A, vol. 79, no. 3, p. 032111, 2009.

[174] G. J. Dolan, "Offset masks for lift-off photoprocessing," Appl. Phys. Lett., vol. 31, no. 5, pp. 337–339, 1977.

[175] M. J. Reagor, Superconducting cavities for circuit quantum electrodynamics. Yale University, 2016.

[176] E. D. Black, "An introduction to pound–drever–hall laser frequency stabilization," American journal of physics, vol. 69, no. 1, pp. 79–87, 2001.

[177] T. M. Hazard, Improving Quantum Hardware: Building New Superconducting Qubits and Couplers. PhD thesis, Princeton University, 2019.

[178] D. I. Schuster, Circuit quantum electrodynamics. Yale University, 2007.

[179] A. P. Sears, Extending Coherence in Superconducting Qubits: from microseconds to milliseconds. Yale University, 2013.

[180] J. W. Harlow, Microwave electromechanics: Measuring and manipulating the quantum state of a macroscopic mechanical oscillator. PhD thesis, University of Colorado at Boulder, 2013.

[181] J. Zhang, K. Peng, and S. L. Braunstein, "Quantum-state transfer from light to macroscopic oscillators," Physical Review A, vol. 68, no. 1, p. 013808, 2003.

[182] A. C. Davison and D. V. Hinkley, Bootstrap methods and their application, vol. 1. Cambridge university press, 1997.

Appendix A

Technical specifications of the circuit QED system and electro-optic transducer

A.1 Circuit QED system

The circuit QED system consists of a planar superconducting transmon qubit coupled to the fundamental mode of a seamless 3D aluminum cavity. The qubit was fabricated on a 14×2 mm^2 c-plane sapphire chip. Using a single e-beam lithography step, the Dolan bridge process ([174] and see Appendix B) was used to fabricate an Al$-$AlO$_x-$Al Josephson junction with area of $150 \times 250\,\mathrm{nm}^2$. The qubit capacitance comes from two rectangular 500×700 µm pads separated by 200 µm.

The cavity, a 40 mm long circular waveguide with radius 4.7 mm, was machined out of a single piece of 99.999% purity aluminum. The waveguide is open at one end, with a 7.25 mm long post with 1.5 mm radius at the other end; this geometry defines the fundamental mode as a quarter-wave resonance with evanescent coupling to the waveguide above [98]. A cross section of the CAD model for the circuit QED system is shown in Figure A.2 alongside of a photo of one of the cavities, while Figure A.2 shows a picture of the optical access dilution refrigerator containing both the circuit QED module and the electro-optic transducer. To reduce surface loss, the cavity was etched in Transene aluminum etchant Type A for 24 hours at ambient temperature. A sapphire rod with radius 2 mm is epoxied to a copper plate and fastened to a piezoelectric stepping module above the waveguide with a maximum travel of 5 mm. This assembly allows the sapphire rod to be translated along the center of the waveguide to tune the fundamental mode's resonant frequency ω_c *in situ* by up to 1.7 GHz. The cavity mode has a total linewidth of $\kappa_c = \kappa_{c,w} + \kappa_{c,int} + \kappa_{c,ext}$ and is strongly overcoupled to the transmission line connected to the electro-optic transducer. To achieve

coupling to the weak and strong ports at rate $\kappa_{\mathrm{c,w}}$ and $\kappa_{\mathrm{c,ext}}$ respectively, the outer conductor and dielectric are removed from the end of a superconducting coaxial cable such that the center conductor can be inserted into the cavity through a hole in the bottom of the quarter wave resonator (see Figure A.2). Since the coupling pin is being injected at a node of the resonance it is critical that the pin be superconducting, as the pin extends several millimeters into the cavity to achieve the appropriate amount of coupling. This technique for coupling to the resonant mode was chosen over more standard evanescent coupling techniques at the anti-node of the microwave resonance [175] due to spatial constraints in the optical access dilution refrigerator.

The circuit QED system can be described by the Jaynes-Cummings model with interaction Hamiltonian $\hat{H}_{\mathrm{int}}^{\mathrm{JC}} = \hbar g_{\mathrm{qc}}(\hat{d}^{\dagger}\hat{\sigma}^{-} + \hat{d}\hat{\sigma}^{+})$. When the qubit is far detuned from the resonator ($g_{\mathrm{qc}} \ll |\Delta_{\mathrm{qc}}|$, where $\Delta_{\mathrm{qc}} = \omega_{\mathrm{q}} - \omega_{\mathrm{c}}$), the Jaynes-Cummings model can be described under the dispersive approximation $\hat{H}_{\mathrm{int}}^{\mathrm{JC}} = -\hbar\chi\hat{\sigma}_{\mathrm{z}}\hat{d}^{\dagger}\hat{d}$. The dispersive shift χ is given by $\chi = g_{\mathrm{qc}}^{2}\nu/\left(\Delta_{\mathrm{qc}}(\Delta_{\mathrm{qc}} - \nu)\right)$ [22], where the qubit anharmonicity ν encodes the contribution from higher energy levels of the transmon qubit. See Extended Data Table A.1 for a list of parameters describing the circuit QED system.

The qubit lifetime ($T_1 = 17$ µs) is far from Purcell-limited [84], likely due to participation of lossy dielectrics that remain after e-beam lithography and aluminum deposition. The coherence time of the qubit is $T_2^{\mathrm{R}} \approx T_2^{\mathrm{echo}} \approx 20$ µs, and no difference is seen when measured using a Hahn echo versus a standard Ramsey sequence.

The circuit QED system is contained in a magnetic shield comprising an outer shield of high-permeability Amumetal 4K and an inner shield made of pure aluminum in order to minimize stray magnetic fields near the circuit QED system during cooling of the device through its critical temperature.

A.2 Electro-optic transducer

The electro-optic transducer consists of a microwave resonator and an optical resonator simultaneously coupled to a single mode of a micromechanical oscillator. It is described by the

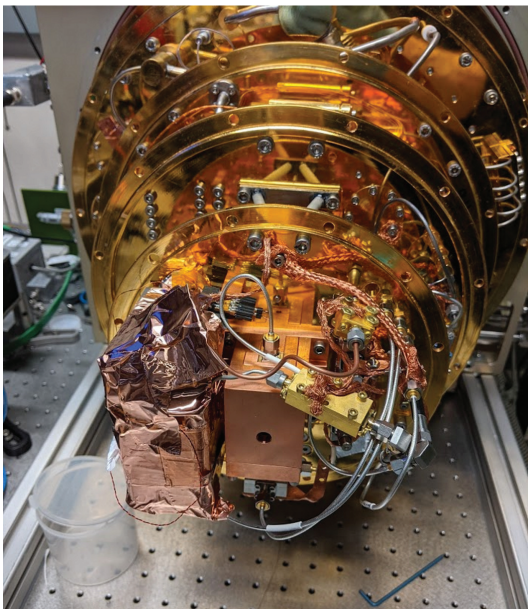

Figure A.1: **Image of the optical access dilution refrigerator.** The circuit QED module is covered in copper tape and on the left. The copper box in the center of the base plate contains the electro-optic transducer.

Hamiltonian

$$\frac{\hat{H}}{\hbar} = \omega_{\mathrm{o}}\hat{a}^{\dagger}\hat{a} + \omega_{\mathrm{e}}\hat{b}^{\dagger}\hat{b} + \omega_{\mathrm{m}}\hat{c}^{\dagger}\hat{c} + (g_{\mathrm{o}}\hat{a}^{\dagger}\hat{a} + g_{\mathrm{e}}\hat{b}^{\dagger}\hat{b})(\hat{c} + \hat{c}^{\dagger}), \tag{A.1}$$

where $\hat{a}$, $\hat{b}$ and $\hat{c}$ are the annihilation operators for the optical, microwave and mechanical modes, respectively, and g_{o} (g_{e}) is the vacuum optomechanical (electromechanical) coupling rate.

The mechanical oscillator is a 100 nm thick, 500 μm wide square silicon nitride membrane suspended from a silicon chip. Phononic shielding is patterned into the silicon chip, isolating the membrane mode used for transduction, with resonant frequency $\omega_{\mathrm{m}} = 2\pi \times 1.45$ MHz, from vibrational modes of the chip. This shielding results in a quality factor $Q_{\mathrm{m}} = 1.3 \times 10^7$ for the mode of interest, or equivalently an energy dissipation rate $\gamma_{\mathrm{m}} = 2\pi \times 0.11$ Hz.

The microwave resonator is a superconducting flip-chip LC circuit whose capacitance is modulated by the motion of a superconducting pad deposited on the membrane. The strength of the electromechanical coupling is determined by the capacitor gap spacing between this pad and a second nearby chip hosting the rest of the circuit, which is $\sim$ 300 nm for most devices. In the

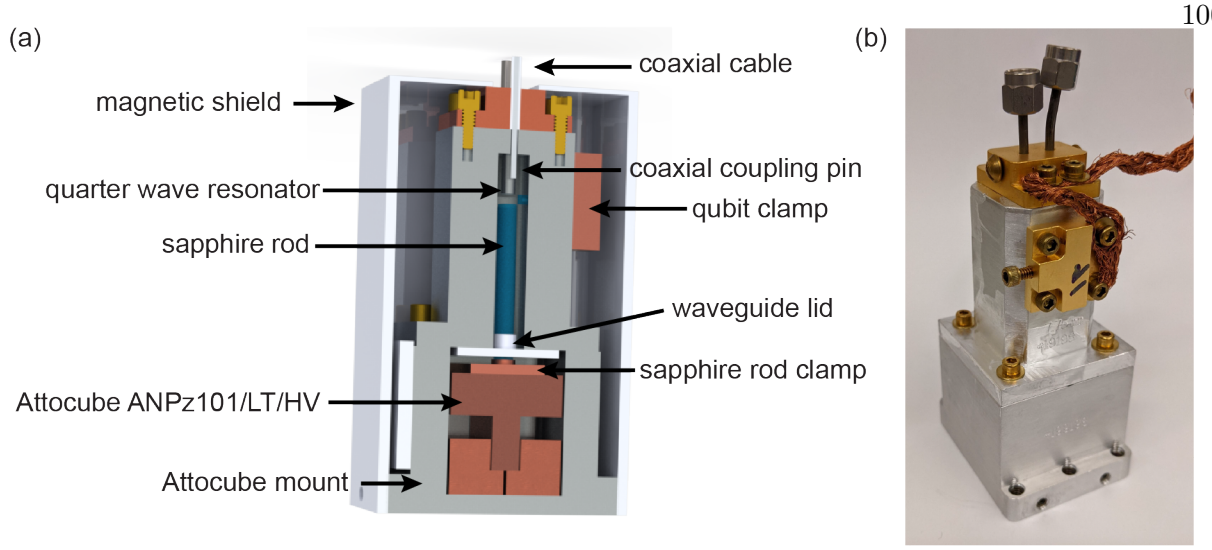

Figure A.2: **CAD model of the circuit QED system.** (a) The circuit QED system is formed by a superconducting qubit coupled to a 3d quarter wave post resonator evanescently coupled to the wave guide above. A sapphire rod can be translated towards the end of the post resonator in order to tune its frequency. The sapphire rod is epoxied to a clamp with Stycast 2850 and then the clamp is attached to the Attocube translation stage. A lid with a narrow hole for the sapphire rod to pass through is attached to the top of the waveguide to prevent coupling of modes in the Attocube mount to modes within the waveguide and the quarter wave resonator. (b) Photo of the circuit QED system and Attocube mount. A copper braid is attached to the gold plated copper qubit clamp in order to better thermalize the superconducting qubit to the base temperature of the dilution refrigerator.

transducer used in this work the capacitor gap was unusually large, resulting in a low vacuum electromechanical coupling rate $g_\mathrm{e} = 2\pi \times 1.6$ Hz. The LC circuit is coupled to a microwave transmission line at rate $\kappa_{\mathrm{e,ext}} = 2\pi \times 1.42$ MHz, and its total linewidth κ_e varies between 1.6 MHz and 2.7 MHz due to dependence of the internal loss $\kappa_{\mathrm{e,int}}$ on the power of the strong microwave pump used to mediate transduction.

The optical resonator is a Fabry-Pérot cavity defined by high-reflectivity ion beam sputtered mirror coatings, which are chosen to be very asymmetric such that the cavity mode couples preferentially out the front mirror with external coupling $\kappa_{\mathrm{o,ext}} = 2\pi \times 2.1$ MHz. The total cavity linewidth is $\kappa_\mathrm{o} = \kappa_{\mathrm{o,ext}} + \kappa_{\mathrm{o,int}} = 2\pi \times 2.7$ MHz, where $\kappa_{\mathrm{o,int}}$ includes scattering and absorption losses as well as transmission through the back mirror. The membrane is positioned at a maximum in the intensity gradient of the intracavity light, yielding a vacuum coupling rate $g_\mathrm{o} = 2\pi \times 60$ Hz.

The heterodyne mode matching factor quantifying the overlap of the propagating optical cavity mode and the local oscillator beam (LO) is $\epsilon = 0.8$.

During operation, strong microwave and optical pumps are applied near the corresponding electromagnetic resonances to enhance the vacuum coupling rates g_o and g_e [67]. Transforming to a rotating frame to remove the free evolution of the fields, $\hat{a} \to \hat{a}e^{-i\omega_\mathrm{o}t}$, $\hat{b} \to \hat{b}e^{-i\omega_\mathrm{e}t}$ and $\hat{c} \to \hat{c}e^{-i\omega_\mathrm{m}t}$, the Hamiltonian can then be linearized around the strong pumps to yield

$$\frac{\hat{H}_\mathrm{int}^\mathrm{lin}}{\hbar} = g_\mathrm{o}\bar{a}(\hat{a}^\dagger + \hat{a})(\hat{c} + \hat{c}^\dagger) + g_\mathrm{e}\bar{b}(\hat{b}^\dagger + \hat{b})(\hat{c} + \hat{c}^\dagger), \tag{A.2}$$

where $\bar{a}$ ($\bar{b}$) is the optical (microwave) mode coherent state amplitude due to the incident pump. Both pumps are red-detuned from the respective resonances by ω_m, resonantly enhancing the optomechanical and electromechanical beamsplitter terms in the Hamiltonian [79]. In the resolved sideband limit at this optimal detuning, the electromechanical (optomechanical) damping rate is then given by $\Gamma_\mathrm{o} = 4g_\mathrm{o}^2\bar{a}^2/\kappa_\mathrm{o}$ $\left(\Gamma_\mathrm{e} = 4g_\mathrm{e}^2\bar{b}^2/\kappa_\mathrm{e}\right)$. The transducer bandwidth is given by $\Gamma_\mathrm{T} = \Gamma_\mathrm{e} + \Gamma_\mathrm{o} + \gamma_\mathrm{m}$.

The electro-optic transducer parameters are summarized in Tab. A.1. See Ref. [69] for a more detailed description of the fabrication, assembly, and characterization of the electro-optic transducer, as well as the theory of transducer operation.

A.3 Experimental layout

A schematic of the experimental setup is shown in Supplementary Figure A.3. Here I briefly summarize the details of the optical setup, discussed further in Ref. [69].

A beam sourced by a low-noise external cavity diode laser (Toptica Photonics CTL) operated at a wavelength $\lambda = 1084$ nm is passed through an optical filter cavity (not shown) to further reduce laser phase noise, and then split three ways to obtain pump (red), lock (yellow), and local oscillator (LO, maroon) beams. The pump and lock beams are frequency shifted relative to the LO beam by acousto-optic modulators, such that the lock beam is resonant with the optical cavity mode, the pump beam is red-detuned by ω_m, and the LO beam is detuned from the pump beam by 12.8 MHz

Table A.1: Circuit QED system and electro-optic transducer parameters.

Parameter	**Symbol**	**Value**
Qubit frequency	ω_{q}	$\omega_{\mathrm{q}}/2\pi = 5.632$ GHz
Qubit-cavity coupling	g_{qc}	$g_{\mathrm{qc}}/2\pi = 66.4$ MHz
Qubit anharmonicity	ν	$\nu/2\pi = 228$ MHz
Dispersive shift	χ	$\chi/2\pi = 172$ kHz
Cavity frequency	ω_{c}	$\omega_{\mathrm{c}}/2\pi = 7.938$ GHz
Cavity linewidth	κ_{c}	$\kappa_{\mathrm{c}}/2\pi = 380$ kHz
Weak port coupling	$\kappa_{\mathrm{c,w}}$	$\kappa_{\mathrm{c,w}}/2\pi < 5$ kHz
Cavity internal loss	$\kappa_{\mathrm{c,int}}$	$\kappa_{\mathrm{c,int}}/2\pi < 10$ kHz
Qubit lifetime	T_1	$T_1 = 17$ µs
Ramsey time	T_2	$T_2 = 20$ µs
Optical cavity frequency	ω_{o}	$\omega_{\mathrm{o}}/2\pi = 277$ THz
Optical cavity external coupling	$\kappa_{\mathrm{o,ext}}$	$\kappa_{\mathrm{o,ext}}/2\pi = 2.12$ MHz
Optical cavity linewidth	κ_{o}	$\kappa_{\mathrm{o}}/2\pi = 2.68$ MHz
LC circuit frequency	ω_{e}	$\omega_{\mathrm{e}}/2\pi = 7.938$ GHz
LC circuit external coupling	$\kappa_{\mathrm{e,ext}}$	$\kappa_{\mathrm{e,ext}}/2\pi = 1.42$ MHz
LC circuit linewidth (low pump power)	κ_{e}	$\kappa_{\mathrm{e}}/2\pi \approx 1.6$ MHz
LC circuit linewidth (high pump power)	κ_{e}	$\kappa_{\mathrm{e}}/2\pi \approx 2.7$ MHz
Mechanical mode frequency	ω_{m}	$\omega_{\mathrm{m}}/2\pi = 1.45$ MHz
Intrinsic mechanical dissipation rate	γ_{m}	$\gamma_{\mathrm{m}}/2\pi = 0.11$ Hz
Vacuum optomechanical coupling	g_{o}	$g_{\mathrm{o}}/2\pi = 60$ Hz
Vacuum electromechanical coupling	g_{e}	$g_{\mathrm{e}}/2\pi = 1.6$ Hz
Optical cavity mode matching	ϵ	$\epsilon = 0.80$

to enable heterodyne measurement. The lock and pump beams are orthogonally polarized and thus can be combined and routed to separate detectors using a polarizing beamsplitter.

The Pound-Drever-Hall technique [176] is employed to simultaneously lock the laser to both the optical filter cavity and the transducer's optical cavity. The error signal is used to feed back to the laser wavelength, the filter cavity length, and the rf drive to an acousto-optic modulator. The absence of tuning elements on the transducer's optical cavity leads to improved stability relative to cavities in previous devices [56].

As shown in Supplementary Figure A.3, the qubit control and readout pulses are generated via individual sources and controlled and gated by mixers and switches [20].

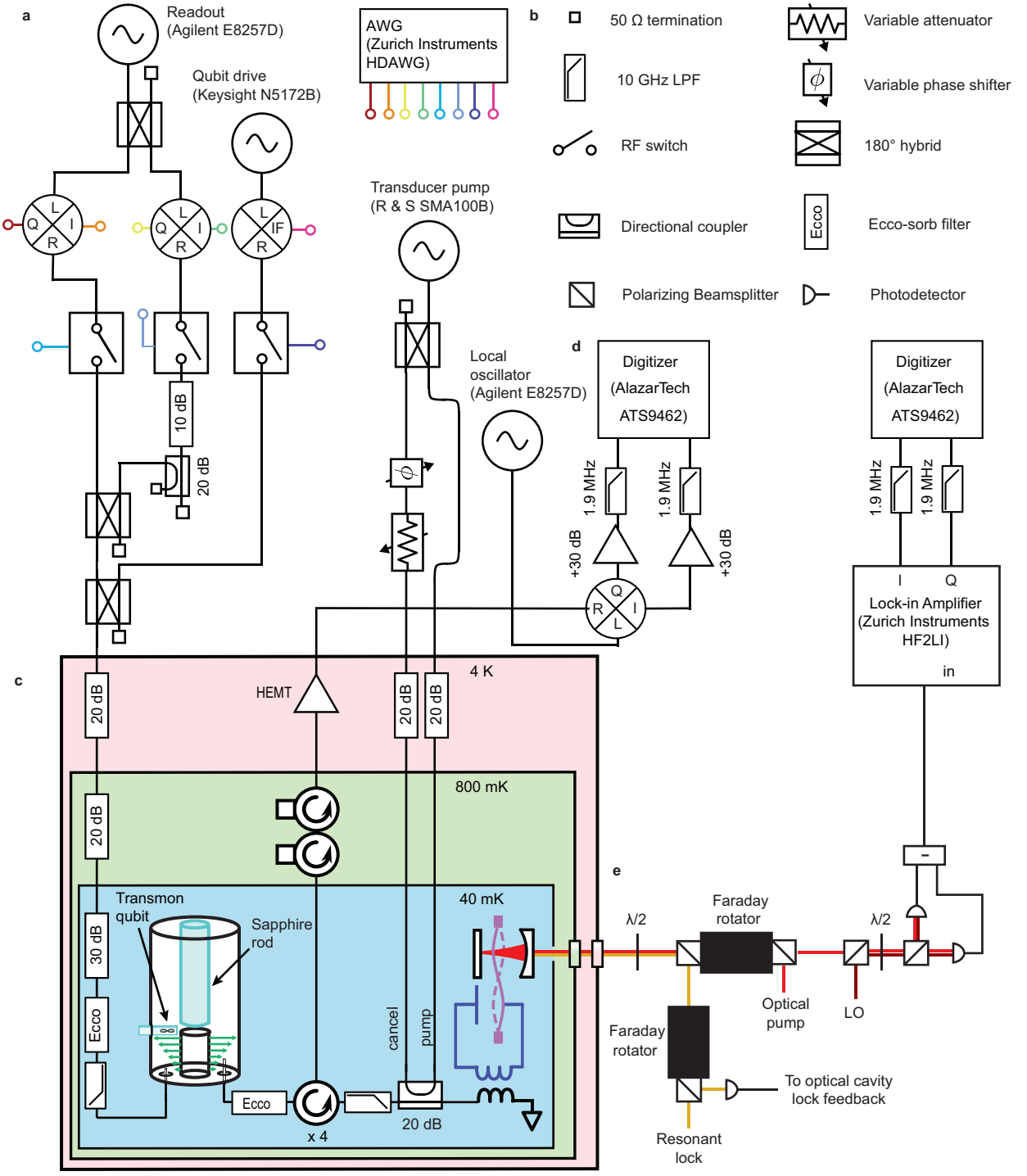

Figure A.3: **Experimental schematic.** (a) Microwave layout demonstrating the exact configuration of the qubit readout/control pulses and the pumps for the electro-optic transducer. (b) Legend for various different microwave and optical components. (c) Cryogenic portion of the experiment. (d) Demodulation and detection scheme. The two digitizers allow for simultaneous measurement of the microwave and optical signals emitted from the transducer. (e) Simplified schematic of optical beam layout and balanced heterodyne detector.

Appendix B

Qubit Fabrication procedure

Here I describe the procedure used to fabricate qubits in the JILA cleanroom using wafer scale techniques and the standard Dolan bridge process [174, 177]. Similar procedures for fabricating basic transmon qubits through electron-beam lithography can be found here [178]. The process described here can easily be generalized to fabricating individual qubit chips.

(1) Sonicate the sapphire wafer at high power in acetone and then IPA for two minutes in each solvent. Depending on the wafer supplier additional cleaning may be needed.

(2) Blow the wafer dry after the IPA clean to ensure all solvent is removed.

(3) Place wafer on 3 glass slides (for a 3" wafer) on top of a hot plate at 180 °C to pre-bake the wafer for 3 minutes. The exact baking time is not particularly important as this is just to ensure that the wafer is entirely dry before spinning resist.

(4) Remove the wafer from the hot plate, let it cool for at least one minute.

(5) Program the spin coater to run at 4000 RPM and accelerate at 1000 RPM/s, with a 45 s spin time. Place the wafer onto the vacuum chuck, turn on the vacuum to hold the wafer.

(6) Pour the co-polymer (MMA(8.5) EL 10) directly onto the wafer, making sure that the vast majority of the wafer is coated in resist to ensure uniformity of the resist across the entire wafer after spinning.

(7) Close the spin coater lid, and run the spin cycle. Once completed, turn off the vacuum chuck, and place the wafer on the hot plate.

(8) Bake for 6 minutes at 180 °C.

(9) Remove the wafer, and let it cool for one minute.

(10) Repeat the previous four steps but with PMMA A6 instead of the co-polymer.

(11) The wafer can now be loaded into the vacuum chamber for deposition of a 15 nm aluminum dissipation layer. This layer prevents charging of the wafer during electron beam lithography.

(12) After aluminum deposition, the wafer can be stored in a black wafer carrier (PMMA is nominally not sensitive to UV light, but there is no need to expose it unnecessarily) for as long as is needed.

(13) Using a diamond scribe or metal tweezers, put 6 scratches onto the outer radius of the wafer for future focusing purposes.

(14) Load the wafer into the SEM, focus and adjust stigmators on the auxiliary gold sample.

(15) Move over to the wafer and align to the flat of the wafer so that the junctions will be parallel with the wafer flat.

(16) Move to the Faraday cup. Use NPGS to measure the beam current at a spot size of 1.1 and 5.0, though these may vary based upon the SEM emission current. Essentially, it is best to write junctions and the fingers connecting them to the pads with less than 100 pA of current, and it is best to write the transmon pads with approximately 2.5 nA of current. Using more current than this to write the pads typically ruins the junctions (likely from stray charge incident on the junction region), while less current than this makes writing take a prohibitively long time.

(17) Return to the gold sample, check if the stigmators need to be adjusted further, or if the focus has changed. This can occasionally occur when switching the spot size of the beam.

(18) Once focused, move to the wafer's edge and find one of the scratches. Avoid traversing the center of the wafer so as not to expose the resist.

(19) By adjusting the Z-position of the SEM stage (not the focus knob!) bring the SEM into focus on a loose piece of aluminum near the scratch. Do not try to focus on the inside of the scratch as this is not conducting and will charge up and obscure the image.

(20) In the SEM software, record this position as focused using the direct stage control functionality.

(21) Move to the next scratch by traveling around the outer edge of the wafer. The sample should in all likelihood not be in focus due to tilt of the wafer. Find another flake of aluminum at the new scratch, but this time use the fine focus knob to focus on the sample, again record on the direct stage control feature that the sample is in focus.

(22) Repeat this procedure above (without changing the Z-position of the SEM stage) on all 6 scratches so that the SEM can fit a plane to find the tilt and automatically adjust the focus for a given X-Y coordinate.

(23) Switch the control of the software to NPGS mode, and ensure that the beam blanker is set to external (NPGS) control mode.

(24) Go to the center of the wafer, and run the desired NPGS write program.

(25) Once the electron beam writing is completed prepare four crystallizing dishes with MF-26A (dilute TMAH based photoresist developer), water, MIBK (1-3 parts MIBK to IPA) and IPA. Turn a hot plate on to 100 °C.

(26) Etch the aluminum in MF-26A. Once the aluminum is no longer visible, etch for 10 additional seconds. Remove the wafer and place in a dish of water for 30 s.

(27) Remove the wafer from the water and blow dry with nitrogen. Be certain that all TMAH has been diluted/rinsed off with water before doing so as you do not want to spray this toxic chemical into the air or onto anything else.

(28) Once the wafer is dry, submerge the wafer in MIBK for 45 s. The precise amount of development time will determine the size of the junctions, so it is important to keep this time consistent.

(29) After development, immediately submerge the wafer in IPA for 30s.

(30) Remove the wafer and blow dry with nitrogen gas.

(31) Bake the wafer on the hot plate at 100 °C for one minute.

(32) Inspect the resist under a microscope, looking to see that the features appear as expected. You will not be able to resolve the junctions directly, but you should be able to see that there is a wire connecting both pads to each other through the junction.

(33) Once visual inspection is passed, bring the wafer to the reactive ion etcher for O_2 plasma cleaning.

(34) Using 50 w and 50 SCCM of O_2 for 10 seconds, run the O_2 plasma cleaning cycle.

(35) Immediately the place wafer in the deposition chamber, being careful to align the wafer flat with the vertical grooves on the wafer holder, and then place the wafer in the chamber and pump out to ideally better than 2×10^{-7} Torr.

(36) Evaporate 30 nm of aluminum with sample at 20°.

(37) Quickly stop the evaporation by going down to 30 mA of electron-beam current on the aluminum crucible—note, this current value is for the JILA evaporator. This will keep the crucible hot, but stop the evaporation process. Close the gate valve between the evaporator and the sample chamber. Let in approximately 7 Torr of oxygen to the sample chamber to

oxidize the aluminum for three minutes. The time and pressure can be varied to control the junction resistance. Alternatively the junction size can also be varied to adjust the junction resistance.

(38) Right before the oxidation time is up turn the evaporator off completely.

(39) Pump the oxygen out of the chamber, and when the chamber is below 8×10^{-2} Torr, the valve to the roughing pump can be closed, and the gate valve can be opened. The evaporator should be turned on and ramped to its maximum current immediately after the vacuum interlock allows one to do so, and evaporation should resume relatively quickly because the aluminum crucible was kept hot.

(40) Once a sufficiently large evaporation rate is achieved (typically in the range of 0.3 nm/s with the shutter closed), the sample can be rotated to 340° to evaporate 60 nm of aluminum.

(41) With the second layer of aluminum complete, the evaporator can be ramped down to 30 mA. Once the deposition rate has returned to zero, close the gate valve between the sample chamber and the evaporation chamber and oxidize the sample for 10 minutes in 7 Torr of oxygen.

(42) Pump out the oxygen with the rough pump and then vent the sample chamber to remove the sample.

(43) Place wafer upright in a teflon stand in large beaker of PG remover at 80° C for lift-off. It's best to leave this overnight, though several hours typically works.

(44) Perform liftoff using a transfer pipette to gently 'blow' off the remaining aluminum on the wafer inside of the solvent.

(45) Clean the wafer in IPA and methanol at low power in the sonicator, and then blow dry.

(46) Spin a protective layer of thick positive photoresist onto the wafer. It is important to use positive photo resist as the wafer is going to be exposed to UV light when dicing, which

could make a negative photoresist difficult to remove due to cross-linking of the resist.

(47) Using heat sensitive double sided tape, fix the sapphire wafer to a thick silicon wafer. Affix this to the dicing saw with the vacuum chuck.

(48) Dice the chips.

(49) Blow off all of the water using dry nitrogen, and place the silicon wafer onto a hot plate at 100 °C.

(50) Once the heat tape releases, remove the silicon wafer from the hot plate, and transfer the chips over to the machined aluminum cleaning jig. The wire shorting the pads together can be used to determine which side of the chip the aluminum was deposited on if needed.

(51) Soak and sonicate the chips in acetone. Replacing the acetone 2-3 times to ensure that the dissolved photoresist is largely removed.

(52) Transfer the chip cleaning jig to PG remover at 80°C for at least several hours, preferably overnight.

(53) Transfer the chip cleaning jig to IPA (acetone does not dissolve PG remover). Sonicate at low power for several minutes.

(54) Sonicate the chips in acetone. It can also be worthwhile to let the chips soak in acetone for several more hours or overnight.

(55) Sonicate the chips in IPA and/or Methanol.

(56) Blow each chip dry individually, and carefully place face up on a microscope slide.

(57) Place the slides with the chips in the reactive ion etcher. Using an oxygen atmosphere at 100 W and 100 SCCM of O_2 for 3 minutes, run the reactive-ion etcher. Repeat this cycle 2-3 times. This step is critical for the lifetime of the qubit as during our dicing process

some sort of surface contamination that remains after the above cleaning steps seems to be removed by this plasma cleaning process.

(58) Place chips in gelpack for storage in dry box or for transport to the probing station.

(59) Probe chips to select for appropriate junction resistance. [179].

Appendix C

Transient electromechanical amplification experimental details

C.1 Theory

C.1.1 Two-tone electromechanical equations of motion

Starting with the linearized Heisenberg-Langevin equations of motion [79] in a frame rotating at a center frequency ω_{r} I find that

$$\dot{\hat{d}} = \left(-\frac{\kappa}{2} + i\Delta\right)\hat{d} + ig_0\alpha(t)(\hat{c} + \hat{c}^\dagger) + \sqrt{\kappa_{\mathrm{ex}}}\hat{d}_{\mathrm{in}} + \sqrt{\kappa_0}\hat{f}_{\mathrm{in}} \tag{C.1}$$

$$\dot{\hat{c}} = \left(-i\omega_{\mathrm{m}} - \frac{\Gamma_{\mathrm{m}}}{2}\right)\hat{c} + ig_0(\alpha^*(t)\hat{d} + \alpha(t)\hat{d}^\dagger) + \sqrt{\Gamma_{\mathrm{m}}}\hat{c}_{\mathrm{in}}, \tag{C.2}$$

while in a two tone driving scheme:

$$\alpha(t) = \alpha_+ e^{-i\omega_+ t} + \alpha_- e^{-i\omega_- t}, \tag{C.3}$$

where $\Delta = \omega_{\mathrm{r}} - \omega_{\mathrm{c}}$ and $\omega_\pm = \omega_{\mathrm{r}} \pm (\omega_{\mathrm{m}} + \delta_{\mathrm{m}})$. Going to a rotating frame for the mechanical mode such that $\hat{c} \to \hat{c}e^{-i(\omega_{\mathrm{m}}+\delta_{\mathrm{m}})t}$ and ignoring all fast counter rotating terms:

$$\dot{\hat{d}} = \left(-\frac{\kappa}{2} + i\Delta\right)\hat{d} + ig_0(\alpha_-\hat{c} + \alpha_+\hat{c}^\dagger) + \sqrt{\kappa_{\mathrm{ex}}}\hat{d}_{\mathrm{in}} + \sqrt{\kappa_0}\hat{f}_{\mathrm{in}} \tag{C.4}$$

$$\dot{\hat{c}} = \left(i\delta_{\mathrm{m}} - \frac{\Gamma_{\mathrm{m}}}{2}\right)\hat{c} + ig_0(\alpha_-^*\hat{d} + \alpha_+\hat{d}^\dagger) + \sqrt{\Gamma_{\mathrm{m}}}\hat{c}_{\mathrm{in}}. \tag{C.5}$$

I define the mechanical and cavity quadratures:

$$\hat{X}_- = \hat{X}_1 = \frac{1}{\sqrt{2}}(\hat{c}^\dagger + \hat{c}) \tag{C.6}$$

$$\hat{X}_+ = \hat{X}_2 = \frac{i}{\sqrt{2}}(\hat{c}^\dagger - \hat{c}) \tag{C.7}$$

$$\hat{U}_1 = \frac{1}{\sqrt{2}}(\hat{d}^\dagger + \hat{d}) \tag{C.8}$$

$$\hat{U}_2 = \frac{i}{\sqrt{2}}(\hat{d}^\dagger - d). \tag{C.9}$$

Specializing to the case $\delta_\mathrm{m} = 0$ and $\omega_\pm = \omega_\mathrm{c} \pm \omega_\mathrm{m}$ (as in [161]) the linearized Heisenberg-Langevin equations can be calculated in the rotating wave approximation:

$$\dot{\hat{X}}_1 = \frac{\sqrt{\kappa}}{2}\left(\sqrt{\Gamma_+} - \sqrt{\Gamma_-}\right)\hat{U}_2 - \frac{\Gamma_\mathrm{m}}{2}\hat{X}_1 + \sqrt{\Gamma_\mathrm{m}}\hat{X}_{1,\mathrm{in}} \tag{C.10}$$

$$\dot{\hat{X}}_2 = \frac{\sqrt{\kappa}}{2}\left(\sqrt{\Gamma_+} + \sqrt{\Gamma_-}\right)\hat{U}_1 - \frac{\Gamma_\mathrm{m}}{2}\hat{X}_2 + \sqrt{\Gamma_\mathrm{m}}\hat{X}_{2,\mathrm{in}} \tag{C.11}$$

$$\dot{\hat{U}}_1 = \frac{\sqrt{\kappa}}{2}\left(\sqrt{\Gamma_+} - \sqrt{\Gamma_-}\right)\hat{X}_2 - \frac{\kappa}{2}\hat{U}_1 + \sqrt{\kappa_\mathrm{ext}}\hat{U}_{1,\mathrm{in}} + \sqrt{\kappa_0}\hat{f}_{1,\mathrm{in}} \tag{C.12}$$

$$\dot{\hat{U}}_2 = \frac{\sqrt{\kappa}}{2}\left(\sqrt{\Gamma_+} + \sqrt{\Gamma_-}\right)\hat{X}_1 - \frac{\kappa}{2}\hat{U}_2 + \sqrt{\kappa_\mathrm{ext}}\hat{U}_{2,\mathrm{in}} + \sqrt{\kappa_0}\hat{f}_{2,\mathrm{in}}. \tag{C.13}$$

Where $\Gamma_\pm = 4g_0^2 n_\pm/\kappa$ depends upon the average number of photons $n_\pm$ circulating in the LC circuit from the red (-) and blue (+) detuned pumps respectively. This experiment stays out of the strong coupling regime such that $\kappa/2 >> \Gamma_\pm$. The cavity decay rate is much larger than all other decays rates in the system, thus the cavity follows the state of the mechanical oscillator, allowing for adiabatic elimination of the cavity amplitude such that $\dot{\hat{U}}_1 = 0$ and $\dot{U}_2 = 0$. This allows for simplification of the system of equations above into two independent equations for the mechanical quadratures:

$$\dot{\hat{X}}_1 = \frac{\Gamma_+ - \Gamma_- - \Gamma_\mathrm{m}}{2}\hat{X}_1 + \sqrt{\Gamma_\mathrm{m}}\hat{X}_{1,\mathrm{in}} + \frac{1}{\sqrt{\kappa}}\left(\sqrt{\Gamma_+} - \sqrt{\Gamma_-}\right)\left(\sqrt{\kappa_\mathrm{ext}}\hat{U}_{2,\mathrm{in}} + \sqrt{\kappa_0}\hat{f}_{2,\mathrm{in}}\right) \tag{C.14}$$

$$\dot{\hat{X}}_2 = \frac{\Gamma_+ - \Gamma_- - \Gamma_\mathrm{m}}{2}\hat{X}_2 + \sqrt{\Gamma_\mathrm{m}}\hat{X}_{2,\mathrm{in}} + \frac{1}{\sqrt{\kappa}}\left(\sqrt{\Gamma_+} + \sqrt{\Gamma_-}\right)\left(\sqrt{\kappa_\mathrm{ext}}\hat{U}_{1,\mathrm{in}} + \sqrt{\kappa_0}\hat{f}_{1,\mathrm{in}}\right). \tag{C.15}$$

To calculate the expected variance of the mechanical quadratures the differential equations can be solved and the noise correlation functions of the cavity and mechanical quadratures can be used:

$$\langle \hat{f}^\dagger_{1,\mathrm{in}}(t)\hat{f}_{1,\mathrm{in}}(t')\rangle = \langle \hat{U}^\dagger_{1,\mathrm{in}}(t)\hat{U}_{1,\mathrm{in}}(t')\rangle = \left(n_\mathrm{c} + \frac{1}{2}\right)\delta(t-t') \tag{C.16}$$

$$\langle \hat{f}^\dagger_{2,\mathrm{in}}(t)\hat{f}_{2,\mathrm{in}}(t')\rangle = \langle \hat{U}^\dagger_{2,\mathrm{in}}(t)\hat{U}_{2,\mathrm{in}}(t')\rangle = \left(n_\mathrm{c} + \frac{1}{2}\right)\delta(t-t') \tag{C.17}$$

$$\langle \hat{X}^\dagger_{1,\mathrm{in}}(t)\hat{X}_{1,\mathrm{in}}(t')\rangle = \left(n_\mathrm{m} + \frac{1}{2}\right)\delta(t-t') \tag{C.18}$$

$$\langle \hat{X}^{\dagger}_{2,\mathrm{in}}(t)\hat{X}_{2,\mathrm{in}}(t')\rangle = \left(n_{\mathrm{m}} + \frac{1}{2}\right)\delta(t-t'). \tag{C.19}$$

Computing the variance gives:

$$\begin{aligned}\langle \Delta\hat{X}_1^2\rangle =& \langle \Delta\hat{X}_1(0)^2\rangle e^{(\Gamma_+ - \Gamma_- - \Gamma_{\mathrm{m}})t} + \\ & \frac{1}{2(\Gamma_+ - \Gamma_- - \Gamma_{\mathrm{m}})}\left((\sqrt{\Gamma_+} - \sqrt{\Gamma_-})^2(2n_{\mathrm{c}}+1) + \Gamma_{\mathrm{m}}(2n_{\mathrm{m}}+1)\right)(e^{(\Gamma_+ - \Gamma_- - \Gamma_{\mathrm{m}})t} - 1)\end{aligned} \tag{C.20}$$

$$\begin{aligned}\langle \Delta\hat{X}_2^2\rangle =& \langle \Delta\hat{X}_2(0)^2\rangle e^{(\Gamma_+ - \Gamma_- - \Gamma_{\mathrm{m}})t} + \\ & \frac{1}{2(\Gamma_+ - \Gamma_- - \Gamma_{\mathrm{m}})}\left((\sqrt{\Gamma_+} + \sqrt{\Gamma_-})^2(2n_{\mathrm{c}}+1) + \Gamma_{\mathrm{m}}(2n_{\mathrm{m}}+1)\right)(e^{(\Gamma_+ - \Gamma_- - \Gamma_{\mathrm{m}})t} - 1).\end{aligned} \tag{C.21}$$

In the large gain limit, such that the energy gain $G = e^{(\Gamma_+ - \Gamma_- - \Gamma_{\mathrm{m}})t} \gg 1$ the noise added at the input of transient electromechanical amplification (TEA) for the two preferred quadratures becomes:

$$\langle \Delta\hat{X}^2_{\mathrm{add},\pm}\rangle = \frac{1}{2|\Gamma_+ - \Gamma_- - \Gamma_{\mathrm{m}}|}\left((\sqrt{\Gamma_+} \pm \sqrt{\Gamma_-})^2(2n_{\mathrm{c}}+1) + \Gamma_{\mathrm{m}}(2n_{\mathrm{m}}+1)\right). \tag{C.22}$$

If instead, I squeeze the motion of the mechanical oscillator with $e^{(\Gamma_+ - \Gamma_- - \Gamma_{\mathrm{m}})t} \approx 0$, then the variance of each preferred quadrature is given by:

$$\langle \Delta\hat{X}^2_{\mathrm{sq},\pm}\rangle = \frac{1}{2|\Gamma_+ - \Gamma_- - \Gamma_{\mathrm{m}}|}\left((\sqrt{\Gamma_+} \pm \sqrt{\Gamma_-})^2(2n_{\mathrm{c}}+1) + \Gamma_{\mathrm{m}}(2n_{\mathrm{m}}+1)\right). \tag{C.23}$$

C.1.2 Additional single mode squeezing due to detuning of microwave pumps

The equations of motion in Section C.1 are valid for $\kappa >> \Gamma_{\pm}$, but even if adiabatic elimination of the cavity mode remains valid, as the pump power is increased, both the cavity resonant frequency and the mechanical resonant frequency depend on the number of photons circulating in the LC circuit. The data can be described by adding in the effects of these pump induced frequency shifts. The following analysis is similar to that in [159] where single mode squeezing of the mechanical oscillator was demonstrated in the large detuning limit $\Delta >> \kappa$ where adiabatic elimination of the cavity field is also valid. I operate in the limit such that $\kappa >> \Delta$ to demonstrate an equivalent

result. Assuming that $\frac{\kappa}{2} >> \Delta$, $\Gamma_\pm$, Γ_m, I can still adiabatically eliminate the cavity fluctuations [180, 181]:

$$\hat{d} \approx \frac{ig_0(\alpha_- \hat{c} + \alpha_+ \hat{c}^\dagger) + \sqrt{\kappa}\hat{d}_\mathrm{in}}{\kappa/2 - i\Delta}, \tag{C.24}$$

where I have ignored the small internal loss of the cavity. This gives an independent equation of motion for the mechanical field as:

$$\dot{\hat{c}} = \frac{\Gamma_+ - \Gamma_- - \Gamma_\mathrm{m}}{2}\hat{c} + i\left(\delta_\mathrm{m} - \frac{\Delta}{\kappa}(\Gamma_+ + \Gamma_-)\right)\hat{c} - \frac{2i\Delta}{\kappa}\sqrt{\Gamma_+\Gamma_-}\hat{c}^\dagger + \tag{C.25}$$

$$i\sqrt{\frac{\Gamma_-}{1+\frac{4\Delta^2}{\kappa^2}}}\left(1 + \frac{2i\Delta}{\kappa}\right)\hat{d}_\mathrm{in} + i\sqrt{\frac{\Gamma_+}{1+\frac{4\Delta^2}{\kappa^2}}}\left(1 - \frac{2i\Delta}{\kappa}\right)\hat{d}_\mathrm{in}^\dagger, \tag{C.26}$$

where I choose a global measurement phase and assume that $\alpha_\pm$ are both real. In this form I can identify two additional terms in the equation for the cavity field that are caused by detuning both microwave tones from cavity resonance. These two terms correspond to a mechanical frequency shift $\delta_\mathrm{m,tot}$ and a single-mode squeezing term χ given by:

$$\delta_\mathrm{m,tot} = \delta_\mathrm{m} - \frac{\Delta}{\kappa}(\Gamma_+ + \Gamma_-) \tag{C.27}$$

$$\chi = \frac{2\Delta}{\kappa}\sqrt{\Gamma_+\Gamma_-}. \tag{C.28}$$

I combine these effects into a coupled set of equations of motion to describe the two cavity quadratures.

$$\begin{bmatrix}\dot{\hat{X}}_1 \\ \dot{\hat{X}}_2\end{bmatrix} = \begin{bmatrix}\frac{\Gamma_+ - \Gamma_- - \Gamma_\mathrm{m}}{2} & \delta_\mathrm{m} + \frac{\Delta}{\kappa}(\sqrt{\Gamma_+} - \sqrt{\Gamma_-})^2 \\ -\delta_\mathrm{m} - \frac{\Delta}{\kappa}(\sqrt{\Gamma_+} + \sqrt{\Gamma_-})^2 & \frac{\Gamma_+ - \Gamma_- - \Gamma\mathrm{m}}{2}\end{bmatrix}\begin{bmatrix}\hat{X}_1 \\ \hat{X}_2\end{bmatrix} + \tag{C.29}$$

$$\begin{bmatrix}\sqrt{\Gamma_\mathrm{m}}\hat{X}_{1,\mathrm{in}} + \frac{\left(\sqrt{\Gamma_+} - \sqrt{\Gamma_-}\right)}{\sqrt{1+\frac{4\Delta^2}{\kappa^2}}}\left(\hat{U}_{2,\mathrm{in}} + \frac{2\Delta}{\kappa}\hat{U}_{1,\mathrm{in}}\right) \\ \sqrt{\Gamma_\mathrm{m}}\hat{X}_{2,\mathrm{in}} + \frac{\left(\sqrt{\Gamma_+} + \sqrt{\Gamma_-}\right)}{\sqrt{1+\frac{4\Delta^2}{\kappa^2}}}\left(\hat{U}_{1,\mathrm{in}} - \frac{2\Delta}{\kappa}\hat{U}_{2,\mathrm{in}}\right)\end{bmatrix}. \tag{C.30}$$

The additional single mode squeezing term and frequency shifts cause significant deviation from the equations of motion in section C.1.1 as the power of the two tones is increased.

C.2 Pump dependent cavity frequency shifts

I estimate the cavity frequency shifts induced by the two microwave tones from optomechanical theory [79] by noting that there is a nonlinear dependence of the detuning from the cavity on

microwave pump power, where α and β are the coherent displacements of the cavity and mechanical oscillators respectively:

$$\alpha = \frac{\sqrt{\kappa_{\mathrm{ex}}}\alpha_{\mathrm{in}}}{\kappa/2 - i\Delta_{\mathrm{eff}}} \tag{C.31}$$

$$\beta = \frac{-ig_0\left|\alpha\right|^2}{\Gamma_{\mathrm{m}}/2 - i\omega_{\mathrm{m}}} \tag{C.32}$$

$$\Delta_{\mathrm{eff}} = \Delta_0 + g_0(\beta + \beta^*). \tag{C.33}$$

Solving these equations (neglecting Γ_{m}) the effective detuning is given by

$$\Delta_{\mathrm{eff}} \approx \Delta_0 + \frac{2g_0^2}{\omega_{\mathrm{m}}}|\alpha|^2 = \Delta_0 + \frac{\kappa}{2\omega_{\mathrm{m}}}(\Gamma_+ + \Gamma_-), \tag{C.34}$$

demonstrating the implicit dependence of the cavity resonant frequency on the pump power sent to the circuit. This also demonstrates that a detuned back-action evading measurement [156] will cause degenerate parametric amplification of the mechanical mode. I use the result from Equation C.34 to solve the full set of equations in Equation C.30. With free parameters $\delta_{\mathrm{m}} = 300$ Hz and $\Delta_0 = -74$ kHz I get good agreement between theory and experiment. Given that there are two adjustable parameters to make the theory agree, other parametric effects such as the ones described in [158] may also contribute. Thermal effects (such as [157]) are less likely because only a small shift in mechanical resonant frequency with temperature is seen, with $\frac{1}{2\pi}\frac{d\omega_{\mathrm{m}}}{dT} \approx 4$ Hz/mK.

C.3 Variance normalization

When preparing or measuring states at or near the limits imposed by quantum mechanics the relevant scale for the variance is the zero-point motion of the oscillator. This is the appropriate scale for squeezing because vacuum squeezing reduces the variance in a single quadrature below the zero-point motion. It is also the relevant scale for measurement noise, because a high gain phase preserving amplifier (simultaneous measurement of both quadratures) must add at least the equivalent of zero-point fluctuations at the input of the measurement [74]. Thus I normalize all variance measurements to zero-point motion $\langle \Delta \hat{X}^2_{\mathrm{zp}} \rangle = 1/2$. Explicitly, this gives the measured

values in decibels as:

$$\langle \Delta \hat{X}^2_{\mathrm{add,db}} \rangle = 10 \log_{10} \left(\frac{\langle \Delta \hat{X}^2_{\mathrm{add}} \rangle}{\langle \Delta \hat{X}^2_{\mathrm{zp}} \rangle} \right) \tag{C.35}$$

$$\langle \Delta \hat{X}^2_{\mathrm{sq,db}} \rangle = 10 \log_{10} \left(\frac{\langle \Delta \hat{X}^2_{\mathrm{sq}} \rangle}{\langle \Delta \hat{X}^2_{\mathrm{zp}} \rangle} \right). \tag{C.36}$$

In Figure 6.4(d) I characterize the variance of the squeezed state $\langle X(\phi)^2 \rangle$ (measured by single quadrature TEA) as a function of phase angle ϕ. To see that I can directly measure a squeezed state without any inference I include measurement noise, but still normalize to zero-point motion:

$$\langle X(\phi)^2_{\mathrm{db}} \rangle = 10 \log_{10} \left(\frac{\langle \Delta X(\phi)^2 \rangle + \langle \Delta \hat{X}^2_{\mathrm{add},-} \rangle}{\langle \Delta X^2_{\mathrm{zp}} \rangle} \right). \tag{C.37}$$

The quantity $\langle \Delta X(\phi)^2 \rangle + \langle \Delta \hat{X}^2_{\mathrm{add}} \rangle$ provides a direct measure of the squeezed state without any inference or noise subtraction.

C.4 Mechanical occupancy, added noise and gain calibrations

To characterize the noise added by TEA and the total amount of mechanical squeezing, states with known variance are required to calibrate these unknown values. To accurately infer the variance of a prepared mechanical state $\langle \Delta X(\phi)^2 \rangle$ the added measurement noise $\langle \Delta X(\phi)^2_{\mathrm{add}} \rangle$ must be known. Conversely to characterize the noise added by measurement, the variance of the prepared mechanical state must be known. I achieve this by comparing the variance of a calibrated mechanical thermal state, to the state I wish to characterize. In microwave engineering this is known as a Y-factor measurement [96]:

$$r(\phi) = \frac{\langle \Delta \hat{X}^2_{\mathrm{therm}} \rangle + \langle \Delta X(\phi)^2_{\mathrm{add}} \rangle}{\langle \Delta X(\phi)^2 \rangle + \langle \Delta X(\phi)^2_{\mathrm{add}} \rangle}. \tag{C.38}$$

The variance of the mechanical thermal state is:

$$\langle \Delta \hat{X}^2_{\mathrm{therm}} \rangle = n_{\mathrm{m}} + 1/2, \tag{C.39}$$

where n_{m} is the independently calibrated thermal occupancy (described in Section C.4.5) of the mechanical oscillator.

C.4.1 Calibration of sideband cooling and two-quadrature measurement noise

In order to fully characterize the added noise of TEA I prepare the mechanical oscillator in states with two different temperatures: a thermal state and a sideband cooled state. A thermal state can be prepared and calibrated by allowing the mechanical oscillator to reach thermal equilibrium (see Section C.4.5). To calibrate the variance of a sideband cooled state $\langle \Delta X_{\rm sb}^2 \rangle$, I measure both quadratures of motion simultaneously with the blue detuned pump ($\Gamma_+ > 0, \Gamma_- = 0$). This nearly quantum limited amplifier adds a total noise to one quadrature of

$$\langle \Delta \hat{X}_{\rm add}^2 \rangle = n_{\rm add} + 1/2, \tag{C.40}$$

where $n_{\rm add}$ is any noise the amplifier adds above zero-point fluctuations. While the variance of the sideband cooled state is

$$\langle \Delta \hat{X}_{\rm sb}^2 \rangle = n_{\rm sb} + 1/2, \tag{C.41}$$

where $n_{\rm sb}$ is the remaining thermal occupancy after sideband cooling. The ratio of the measured thermal state variance to the sideband cooled variance is:

$$r = \frac{\langle \Delta \hat{X}_{\rm therm}^2 \rangle + \langle \Delta \hat{X}_{\rm add}^2 \rangle}{\langle \Delta \hat{X}_{\rm sb}^2 \rangle + \langle \Delta \hat{X}_{\rm add}^2 \rangle} = \frac{n_{\rm m} + n_{\rm add} + 1}{n_{\rm sb} + n_{\rm add} + 1}. \tag{C.42}$$

From the measurements it is clear that $r \gg 1$, indicating that $n_{\rm m} \gg n_{\rm add}$, which allows $n_{\rm add}$ to be neglected in the numerator, and I find that $n_{\rm sb} + n_{\rm add}$ is given by:

$$n_{\rm sb} + n_{\rm add} \approx \frac{1}{r}(n_{\rm m} + 1) - 1. \tag{C.43}$$

Measurements of this number yield a value:

$$n_{\rm sb} + n_{\rm add} = 0.05 \pm .03 \text{ quanta} \tag{C.44}$$

It isn't possible to differentiate between $n_{\rm add}$ and $n_{\rm sb}$, but by comparing it to the minimum theoretically possible number it is possible to demonstrate that the mechanical oscillator is being nearly perfectly sideband cooled. To find this lower bound I use the theory of electromechanical

sideband cooling [79], and find (assuming negligible cavity occupancy) that in the resolved sideband regime the minimum mechanical occupancy after sideband cooling is:

$$n_{\mathrm{sb,min}} \approx \frac{\Gamma_{\mathrm{m}}}{\Gamma_{-}+\Gamma_{\mathrm{m}}} n_{\mathrm{m}} + \frac{\kappa^2}{16\omega_m^2} = .012 \pm .002, \tag{C.45}$$

while equivalently the effective added occupancy at the input of the phase-preserving amplification pulse is given by:

$$n_{\mathrm{add,min}} \approx \frac{\Gamma_{\mathrm{m}}}{\Gamma_{+}-\Gamma_{\mathrm{m}}} n_{\mathrm{m}} + \frac{\kappa^2}{16\omega_m^2} = .018 \pm .002. \tag{C.46}$$

This gives a total minimum remaining occupancy of:

$$n_{\mathrm{sb,min}} + n_{\mathrm{eff,min}} = .030 \pm .004. \tag{C.47}$$

Thus the total remaining occupancy after sideband cooling and measurement in Equation C.44 is nearly equivalent to the minimum possible value $n_{\mathrm{sb}} + n_{\mathrm{eff}} \approx n_{\mathrm{sb,min}} + n_{\mathrm{eff,min}}$, suggesting that the mechanical oscillator is being cooled to very close to the limit of resolved sideband cooling.

C.4.2 Inference of mechanical squeezing

To infer mechanical squeezing and anti-squeezing I use TEA to measure both quadratures simultaneously ($\Gamma_{+} > 0$, $\Gamma_{-} = 0$) and obtain histograms for three separately prepared mechanical states. These histograms can then be used to calibrate the variance and added noise. First, I prepare a mechanical thermal state with variance $\langle X^2_{\mathrm{therm}} \rangle = n_{\mathrm{m}} + 1/2 = 36.5$ by allowing the mechanical oscillator to thermalize with its environment for 250 ms. This is repeated 2048 times to obtain a histogram and estimate the variance of the thermal state in units of V^2/quanta. With a 2 ms repetition time the same procedure is performed with a dissipatively squeezed state. The increased speed of this measurement is enabled by the increased mechanical damping rate from squeezing. The variances of these two histograms are compared as a ratio:

$$r_{\pm} = \frac{\langle \Delta \hat{X}^2_{\mathrm{therm}} \rangle + \langle \Delta \hat{X}^2_{\mathrm{add}} \rangle}{\langle \Delta \hat{X}^2_{\mathrm{sq},\pm} \rangle + \langle \Delta \hat{X}^2_{\mathrm{add}} \rangle} = \frac{n_{\mathrm{m}} + n_{\mathrm{add}} + 1}{\langle \Delta \hat{X}^2_{\mathrm{sq},\pm} \rangle + n_{\mathrm{add}} + 1/2}. \tag{C.48}$$

I assume that n_{add} is equal to its lowest possible value in Equation C.46. This means that any deviation from the ideal perfect two-quadrature measurement will decrease the inferred squeezing.

For each measurement of $\langle \Delta X^2_{\mathrm{sq},\pm} \rangle$ I obtain a histogram of a sideband cooled state, so I can monitor that the added measurement noise remains consistent with the ideal case as in Section C.4.1.

C.4.3 Inference of the measurement noise

I use a similar procedure to Section C.4.2 to infer the noise added by TEA. I obtain histograms of 2048 points for a mechanical thermal state and a sideband cooled state. This results in a ratio of variances of:

$$r_\pm = \frac{n_\mathrm{m} + 1/2 + \langle \Delta \hat{X}_{\mathrm{add},\pm} \rangle}{n_\mathrm{sb} + 1/2 + \langle \Delta \hat{X}_{\mathrm{add},\pm} \rangle}, \tag{C.49}$$

where $\hat{X}_\pm$ are the two preferred quadratures of TEA. At low gains the added noise of the HEMT is significant, and is included in the theory for single quadrature measurement noise. For the inference of $\langle \Delta \hat{X}^2_{\mathrm{add},\pm} \rangle$ I assume perfect sideband cooling as in Equation C.47 to provide a conservative estimate of the added noise. For each variance data point I also make a separate 2048 point two-quadrature measurement of a thermal state and sideband cooled state to infer that n_sb, n_add and n_m remain constant over the course of the entire measurement.

C.4.4 Direct measurement of mechanical variance

For a direct measurement of a mechanical state without any inference I use single quadrature amplification ($\Gamma_+ > 0 > \Gamma_- > 0$) to acquire histograms of a thermal, sideband cooled and squeezed states of motion as in Section C.4.2 and Section C.4.3. I also separately use a two-quadrature measurement to obtain histograms of a mechanical thermal state and sideband cooled state to monitor that n_m, n_sb and n_add remain constant over the course of the entire measurement. Again, I can then compute the ratio of the variance of a mechanical thermal and the squeezed state:

$$r(\phi) = \frac{\langle \Delta \hat{X}^2_\mathrm{therm} \rangle + \langle \Delta \hat{X}_{\mathrm{add},-} \rangle}{\langle \Delta X(\phi)^2_\mathrm{sq} \rangle + \langle \Delta \hat{X}_{\mathrm{add},-} \rangle} \approx \frac{\langle \Delta \hat{X}^2_\mathrm{therm} \rangle}{\langle \Delta X(\phi)^2_\mathrm{sq} \rangle + \langle \Delta \hat{X}^2_{\mathrm{add},-} \rangle}. \tag{C.50}$$

The approximation is valid because $\langle \Delta \hat{X}^2_{\mathrm{add},-} \rangle$ is negligible compared to the $\langle \Delta \hat{X}^2_\mathrm{therm} \rangle$. I can then solve for the total variance of the squeezed state (as measured by TEA):

$$\langle \Delta X(\phi)^2 \rangle = \langle \Delta X(\phi)^2_\mathrm{sq} \rangle + \langle \Delta \hat{X}^2_{\mathrm{add},-} \rangle, \tag{C.51}$$

which is the plotted result in Figure 6.4(d). The blue points in Figure C.2 show $r(\phi)$ as a function of tomography angle, while the red points are an equivalent measurement of a sideband cooled state (nearly mechanical vacuum) using single quadrature amplification. The black points are the ratio of variance of a thermal state and a sideband cooled state obtained from a simultaneous measurement of both quadratures ($\Gamma_+ > 0$ and $\Gamma_- = 0$).

C.4.5 Estimating thermal occupancy of the mechanical oscillator

I independently measure the thermal occupancy of the mechanical oscillator in two separate ways. First, I use the same procedure as in [151, 163], where a very weak continuous red detuned pump is applied such that $\Gamma_\mathrm{m} >> \Gamma_-$. The ratio of the mechanical sideband power P_m and the resulting power circulating in the cavity P_c is measured. The temperature sweeps in Figure C.3a demonstrate that the mechanical oscillator is thermalized to 18 mK (the temperature of the dilution refrigerator) and allows extraction of the electromechanical coupling rate of $g_0 = 2\pi \times (287 \pm 11)$ Hz.

Alternatively, I verify the temperature of the mechanical oscillator by using the blue detuned pump as a quantum limited amplifier

$$\langle \Delta \hat{X}^2_{1,\mathrm{meas}} \rangle = e^{\Gamma_+ t} \left(n_\mathrm{m} + n_\mathrm{add} + 1 \right). \tag{C.52}$$

The measurement of a mechanical thermal state n_m is repeated 2048 times at each different dilution refrigerator base plate temperature to compute the variance. Drift in the gain is corrected at each temperature by measuring the exponential envelope of the amplification pulse to retrieve Γ_+. Figure C.3b shows the result of a temperature sweeps performed in this way. The linear dependence of the variance on temperature demonstrates that the mechanical device is thermalized to the base temperature of the dilution refrigerator (16 mK).

C.4.6 Gain calibration

From the calibration of the total noise, the gain of TEA can be estimated, and can then be compared with the expected results from theory. In Figure C.5 I compare this independently measured gain to the gain expected from $G_- = e^{(\Gamma_+ - \Gamma_-)t}$ and find reasonable agreement. The deviation for large Γ_+/Γ_- may be due to additional parametric effects becoming relevant at high pump powers [157, 158].

C.5 Quadrature extraction

I perform heterodyne detection ($\omega_{\text{het}} = 2\pi \cdot 1.8$ MHz) on the microwave frequency signal emerging from the electromechanical circuit. There are two temporally separated components of the down converted microwave field. First, is a pulse with an exponentially growing envelope that results from the amplification pulse. The second exponentially decreasing microwave pulse encodes the amplified state of the mechanical oscillator that was transferred to the microwave field [164]. Both of these pulses encode the motion of the mechanical oscillator, but due to the additional parametric effects described in C.1.2 the added noise is not exactly equivalent. Figure C.4 shows a comparison of the added noise of TEA when measuring the amplified microwave field and the transferred mechanical field. For all measurements in the main text the transferred mechanical field was used as it exhibited slightly better performance.

C.6 Tracking measurement and squeezing axes

The measurement and squeezing axes are controlled by the average phase $\phi_{\text{avg}} = (\phi_+ + \phi_-)/2$ of the red and blue detuned pumps. This phase is monitored by mixing both pumps down with the local oscillator ($\omega_{\text{LO}} = \omega_{\text{r}} + \omega_{\text{het}}$) and then measuring the phase of the resulting down converted tones with frequencies $\Omega_\pm = \omega_{\text{m}} \pm \omega_{\text{het}}$ on a separate channel of the data acquisition card (see Figure C.6 for experimental schematic). I use this independent measurement of the phase of the microwave tones to track the squeezing and measurement axes as a function of time. Due to a

small frequency difference between the local oscillator (Holzworth HS9000) and the red and blue detuned pump microwave generators (Agilent E8257D) the measurement and squeezing axes drift linearly with time. I measure this phase drift and correct all data points by rotating them back to the initial measurement axis.

C.7 Quantum state tomography

Squeezed and thermal states are inherently Gaussian states, thus to infer the density matrix of these states I assume a Gaussian quasiprobability distribution and perform tomography as in [173]. Using the set of tomography data points $x_k(\phi_j)$, I define the two matrix quantities:

$$D = \sum_{k,j} \frac{S^T(\phi_j)|w_k\rangle\langle w_k|S(\phi_j)}{\langle w_k|S(\phi_j)GR^T(\phi_j)|w_k\rangle + \delta_\eta^2} \tag{C.53}$$

$$R = \sum_{k,j} \frac{R^T(\phi_j)|w_k\rangle\langle w_k|S(\phi_j)}{\langle w_k|S(\phi_j)GR^T(\phi_j)|w_k\rangle + \delta_\eta^2} x_k(\phi_j)^2 \tag{C.54}$$

where $S(\phi)$ is the 2d rotation matrix, $\delta_{\eta_\mathrm{q}}^2 = (1-\eta_\mathrm{m})/(2\eta_\mathrm{m})$ is a function of the measurement efficiency η_m and G is the covariance matrix to be iterated over. To find the covariance matrix describing the data I start with a vacuum covariance matrix and then iterate such that:

$$G^{(i+1)} = (D^i)^{-1} R^i G^i R^i (D^i)^{-1}, \tag{C.55}$$

from which the values of D, R and G are iteratively calculated. As was shown in [173] this procedure will compute the covariance matrix that underlies the data. The covariance matrix for a squeezed thermal state is given by:

$$G = \left(n_\mathrm{sq} + \frac{1}{2}\right) \begin{bmatrix} \cosh(2r) + \sinh(2r)\cos(\phi) & -\sinh(2r)\sin(\phi) \\ -\sinh(2r)\sin(\phi) & \cosh(2r) - \sinh(2r)\cos(\phi) \end{bmatrix}, \tag{C.56}$$

with n_sq, r and ϕ inferred from the tomographic reconstruction. The matrix elements of a squeezed thermal state can be calculated as in [172]. The squeezing parameters inferred from tomography are displayed in Table C.2. The 90% confidence intervals are found from a case re-sampling bootstrap algorithm [182].

C.8 Experimental apparatus

C.8.1 Electromechanical device

The electromechanical device is mounted to the base plate of a dilution refrigerator and held at a temperature of $T \leq 18$ mK. The design and operation of the electromechanical device is described in [163, 151]. Table C.1 shows the relevant parameters of the electromechanical device.

C.8.2 Arbitrary microwave signal generation

I generate the red and blue detuned microwave tones $\omega_{\pm} = \omega_{\mathrm{c}} \pm \omega_{\mathrm{m}}$ with two separate microwave generators (Agilent E8267D). The microwave generators are pulsed on and off with an arbitrary waveform generator (Tektonix AWG 5014C). To control the temporal envelope of the signals the microwave generators act as local oscillators on two separate double-balanced mixers (Marki-0626H), and the IF port of each mixer is controlled with a baseband signal from the AWG. I use square pulses with Gaussian edges ($\sigma = 200$ ns) to avoid driving the mechanical oscillator into a coherent state. The pulses are then sent through two cavity filters to reduce pump fluctuations at ω_{c}. After filtering, the pulses are split into three separate lines. The first two lines are sent into the fridge to pump the electromechanical circuit and to cancel the reflected microwave pumps. The third line is mixed back down against the local oscillator for independent measurement of the phase of the red and blue detuned microwave tones. See Figure C.6 for a full diagram of the experimental schematic. The AWG controls the timing of all pulses, and runs at a 4 Hz repetition rate when measuring thermal states (to allow the mechanical oscillator to reach equilibrium with its environment) and a 500 Hz repetition rate when measuring squeezed and sideband cooled states. To maintain phase coherence between all signals, the frequencies of all generators are set to integer multiples of 500 Hz.

Table C.1: Parameters of the electromechanical device.

Symbol	**Description**	**Value and units**
$\omega_c/2\pi$	Circuit resonant frequency	7.376 841 GHz
$\kappa/2\pi$	Circuit decay rate	3.4 MHz
$\kappa_{ext}/2\pi$	Circuit decay rate into the transmission line	3.1 MHz
$\omega_m/2\pi$	Mechanical resonant frequency	9.3608 MHz
$\Gamma_m/2\pi$	Mechanical decay rate	21 Hz
$g_0/2\pi$	Electromechanical coupling	287 Hz

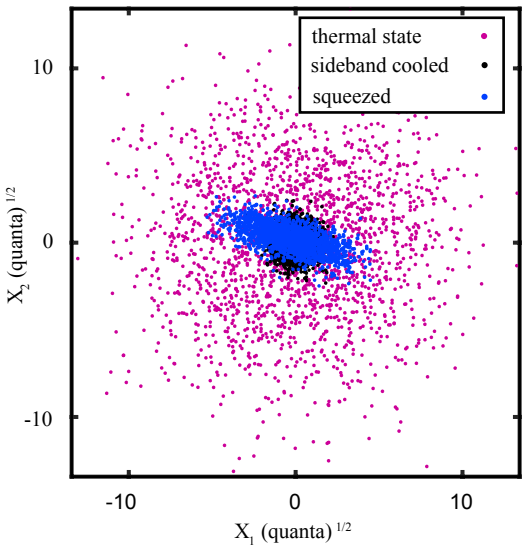

Figure C.1: **Typical measured histograms when inferring squeezed state variance.** To estimate squeezing a thermal state (magenta points, $n_m = 36$) is compared with a sideband cooled state (black points, $n_{sb} > .02$) and a dissipatively squeezed state (blue). I estimate and diagonalize the covariance matrix to retrieve the variances of the three data sets for comparison in the y-factor measurement. This measurement was performed using only the blue detuned pump to simultaneously amplify both quadratures, thus noise equivalent to the mechanical zero-point motion is added to all of these measurements.

Table C.2: Tomographically reconstructed squeezed state parameters

Symbol	**Description**	**Value and units**
r	Squeezing parameter	0.661 ± 0.008
n_{sq}	Thermal occupancy	0.44 ± 0.05 quanta
ϕ	Squeezing angle	1.481 ± 0.005

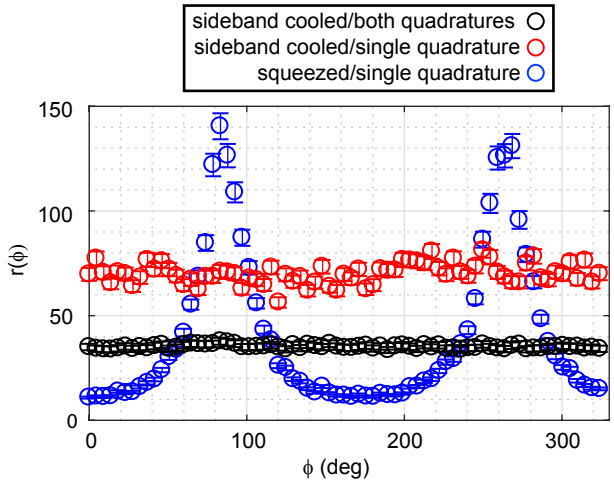

Figure C.2: **Transient electromechanical amplification Y-factor measurement.** The blue points show $r(\phi)$ (see Equation C.48) for a squeezed state measured with single quadrature TEA. The red points are $r(\phi)$ for a sideband cooled state. The black points are $r(\phi)$ (see Equation C.42) for a sideband cooled state measured using two-quadrature TEA.

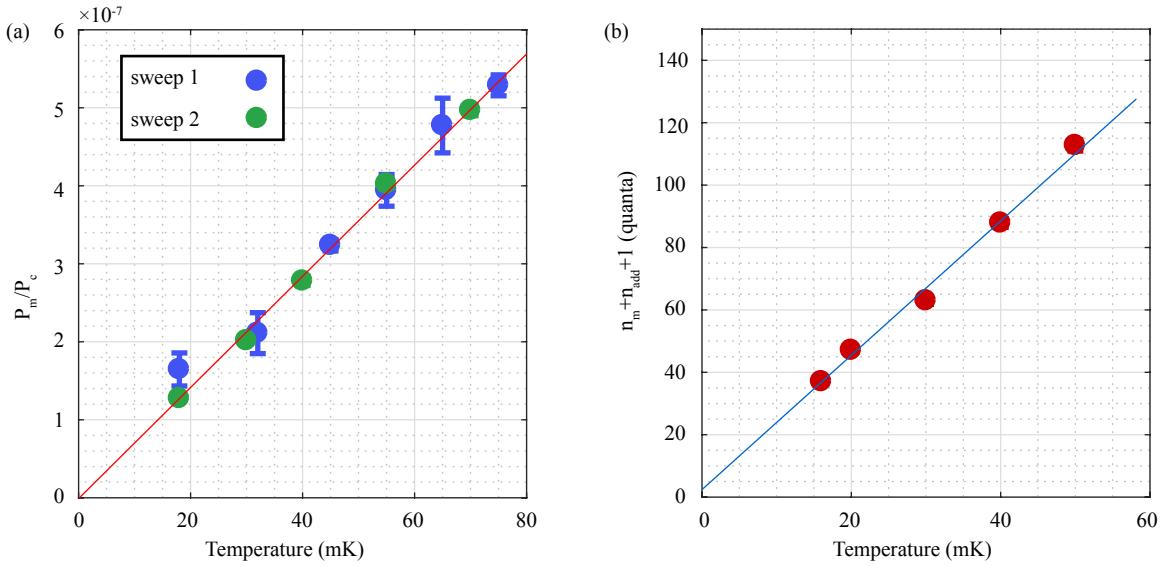

Figure C.3: **Electromechanical temperature sweep.** (a) Ratio of power in the red sideband P_m to power circulating in cavity P_c due to red-detuned pump. This measurement is used to extract the electromechanical coupling rate $g_0 = 2\pi \times (287 \pm 11)$ Hz and verify the steady state thermal occupancy of the mechanical oscillator. The blue and green points represent two separate temperature sweeps. The error bars on the green points are smaller than the data points. These measurements also demonstrate that the mechanical oscillator is thermalized to the base temperature of the fridge. (b) Temperature sweep using blue-detuned pump as a quantum limited amplifier, demonstrating that the mechanical oscillator remains thermalized to the base temperature of the fridge. The linear fit extrapolated to $n_{\mathrm{m}} = 0$ yields the amplifier added noise of $n_{\mathrm{add}} = 1.4 \pm 2.5$, which is consistent with the quantum limited amplification that was inferred in Section C.4.

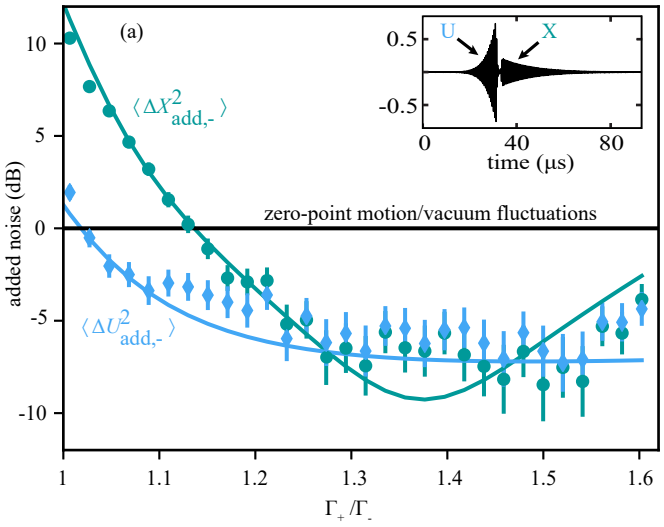

Figure C.4: **Microwave and mechanical noise comparison. Electromechanical temperature sweep.** Comparison of the added noise of TEA when directly measuring the microwave field U or the transferred mechanical field X. The blue diamonds are the added noise of TEA when using the microwave field to measure motion. The teal circles correspond to the case where the quadratures are extracted from the transferred mechanical field. The inset demonstrates the two separate microwave pulses containing X and U. Comparable levels of added noise are achieved, but are not equivalent due to the additional parametric effects (described in Section C.1.2) acting on the mechanical oscillator.

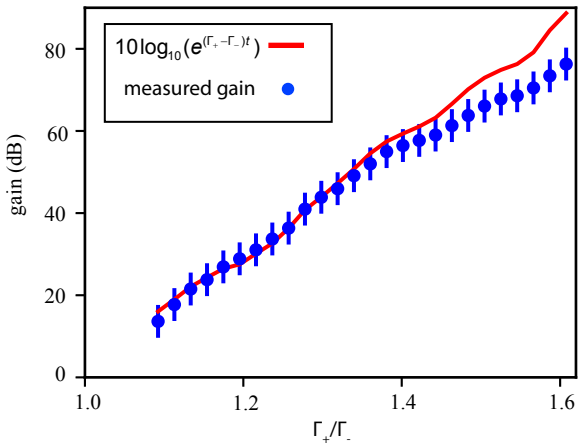

Figure C.5: **Transient electromechanical amplification gain.** Characterization of TEA gain. The blue points are inferred from the the added noise measurements. The red line is theory for the energy gain using only independently measured parameters.

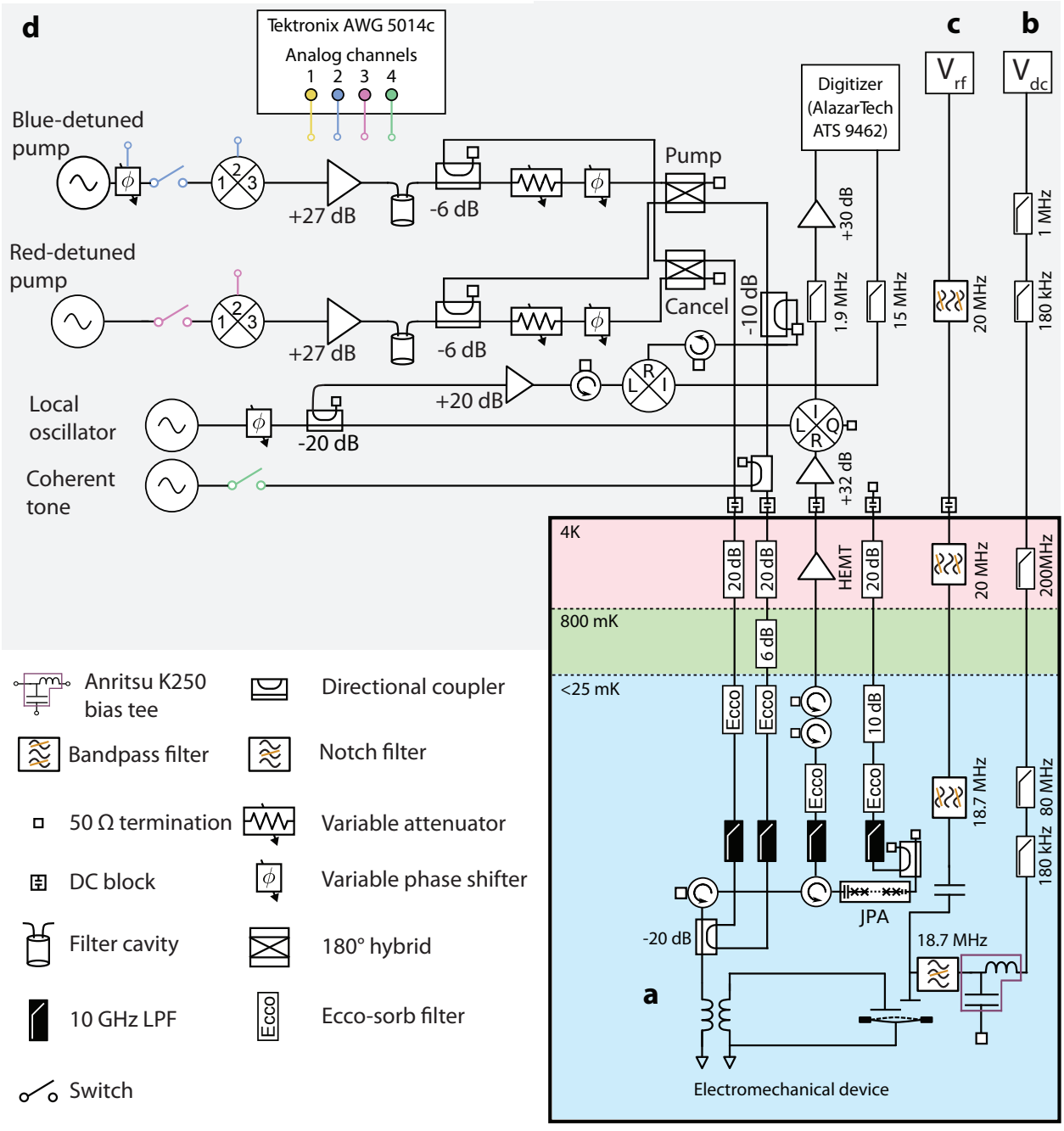

Figure C.6: **Transient electromechanical amplification experimental schematic.** (a) Electromechanical device (b) dc actuation line that allows for the tuning of the mechanical and microwave resonant frequencies, which is not used in this work. (c) rf actuation line allowing for rf modulation of the mechanical resonant frequency, which is not used in this work. (d) Room temperature microwave control and measurement electronics.